

DEPARTMENT OF OCEAN ENGINEERING

MASSACHUSETTS INSTITUTE OF TECHNOLOGY

CAMBRIDGE, MASSACHUSETTS 02139

SELECTING THE PROPER CERAMIC MATERIAL FOR
A REGENERATOR EXPERIENCING LARGE TEMPERATURE
GRADIENTS

BY

MILES Y. KIKUTA

XIII-A

JUNE, 1984

Thesis
K3985

~~FUNCTION OF THE PEPTIDE ANTIBIOTIC,
GRAMICIDIN S, IN ITS PRODUCER,
BACILLUS BREVIS NAGANO~~

~~BY~~

~~Jacqueline Marie Piret
Course XX
March 26, 1981~~

OK16

SELECTING THE PROPER CERAMIC MATERIAL FOR
A REGENERATOR EXPERIENCING LARGE TEMPERATURE GRADIENTS

by

MILES YASUO KIKUTA
B.S. Electrical Engineering
Illinois Institute of Technology
(1974)

SUBMITTED TO THE DEPARTMENT OF
OCEAN ENGINEERING
IN PARTIAL FULFILLMENT OF THE REQUIREMENTS
FOR THE DEGREES OF

OCEAN ENGINEER
and
MASTER OF SCIENCE IN MECHANICAL ENGINEERING

at the

MASSACHUSETTS INSTITUTE OF TECHNOLOGY

JUNE 1984

© Miles Yasuo Kikuta, 1984

The author hereby grants to M.I.T. and to the United States Government and its agencies permission to reproduce and to distribute copies of this thesis document in whole or in part.

SELECTING THE PROPER CERAMIC MATERIAL FOR A
REGENERATOR EXPERIENCING LARGE TEMPERATURE GRADIENTS

by

MILES YASUO KIKUTA

Submitted to the Department of Ocean Engineering on May 11, 1984 in partial fulfillment of the requirements for the Degrees of Ocean Engineer and Master of Science in Mechanical Engineering.

ABSTRACT

The objective of this study is to select the optimum ceramic material for a new engine regenerator. The regenerator will be designed for operation at two working temperatures, a compressed air temperature of about 250°C and an exhaust gas temperature of about 1100°C. Candidate ceramic materials considered were of two types: (1) ceramic materials analyzed for operating temperatures up to 1200°C, and (2) ceramic materials analyzed for operating temperatures between 1200°C and 1400°C. A figure of merit (FOM) rating scheme was utilized to determine the most suitable ceramic material for the regenerator in terms of mechanical, thermal, fabricability and cost parameters. Also, an analysis was performed to determine the most appropriate regenerator passage geometry on an aero-thermodynamic basis.

Thesis Supervisor: A. Douglas Carmichael

Title: Professor of Ocean Engineering

ACKNOWLEDGEMENTS

The author wishes to extend his most sincere thanks to Professor A. Douglas Carmichael, for his support and guidance during the preparation of this thesis. A special thanks is extended to Sandi, for her timely and accurate typing of this thesis.

The author is deeply grateful to his wife, Michele, and son, Michael, for their patience and understanding during the years spent at M.I.T. Finally, much gratitude is extended to my parents, for their continued support, love, and belief in me, which will always be cherished.

TABLE OF CONTENTS

	<u>PAGE</u>
ABSTRACT	2
ACKNOWLEDGEMENTS	3
TABLE OF CONTENTS	4
LIST OF FIGURES	6
LIST OF TABLES	9
CHAPTER 1: BACKGROUND	10
CHAPTER 2: INTRODUCTION	23
CHAPTER 3: CERAMIC MATERIALS ANALYZED FOR OPERATING TEMPERATURES UP TO 1200°C	26
3.1 Introduction	26
3.2 LAS, AS and MAS	26
3.3 Thermal Stability Comparison of LAS, AS and MAS	27
3.4 Thermal Shock Resistance Comparison of LAS, AS and MAS	37
3.5 Thermal Conductivity Comparison of LAS, AS and MAS	42
3.6 Fabricability of LAS, AS and MAS	47
3.7 Cost Comparison of LAS, AS and MAS	50
CHAPTER 4: CERAMIC MATERIALS ANALYZED FOR OPERATION BETWEEN 1200°C-1400°C	
4.1 Introduction	53
4.2 Sintering Process	54
4.3 Sintered SiC	70
4.4 Strength Comparison of Sintered Si ₃ N ₄ and SiC	71
4.5 Corrosion and Oxidation of Sintered Si ₃ N ₄ and SiC	74
4.6 Thermal Shock Comparison of Sintered Si ₃ N ₄ and SiC	93

	<u>PAGE</u>
4.7 Thermal Conductivity Comparison of Sintered Si_3N_4 and SiC	95
4.8 Fabricability of Sintered Si_3N_4 and SiC	95
4.9 Cost Comparison of Sintered Si_3N_4 and SiC	98
CHAPTER 5: MANUFACTURING AND FABRICATING PROCESS	
5.1 Introduction	100
5.2 α - SiC	102
5.3 MAS	117
CHAPTER 6: PASSAGE GEOMETRY ANALYSIS	
6.1 Introduction	121
6.2 Aero-Thermodynamic Analysis	121
6.3 Passage Geometries Analyzed	124
6.4 Passage Geometry Selection	136
CHAPTER 7: COST ANALYSIS	
7.1 Introduction	137
7.2 Comparison of Raw Material Costs	137
7.3 Comparison of Raw Material Availability	138
7.4 Comparison of Manufacturing Costs	139
7.5 Comparison of Total Costs	140
CHAPTER 8: SUMMARY	
8.1 Introduction	143
8.2 MAS	144
8.3 α - SiC	144
REFERENCES	147

LIST OF FIGURES

	<u>PAGE</u>
1.1 REGENERATIVE GAS TURBINE-SPECIFIC AIR AND FUEL CONSUMPTIONS	13
1.2 PRESSURE-VOLUME DIAGRAM OF NEW ENGINE	15
1.3 TEMPERATURE-VOLUME DIAGRAM OF NEW ENGINE	16
1.4 ARRANGEMENT OF THE COMPONENTS FOR THE DOUBLE-SPEED COMPRESSION CYLINDER DESIGN, IN-LINE ENGINE	17
1.5 REGENERATOR ARRANGEMENT	18
1.6 RAW MATERIAL COSTS OF HIGH-TEMPERATURE MATERIALS	21
3.1 PHYSICAL STABILITY OF VARIOUS MATERIALS AT 315°C	29
3.2 PHYSICAL STABILITY OF VARIOUS MATERIALS AT 800°C	30
3.3 AS THERMAL EXPANSION BEFORE AND AFTER 150 HOURS OF ACCELERATED CORROSION TESTING	31
3.4 LAS THERMAL EXPANSION BEFORE AND AFTER 150 HOURS OF ACCELERATED CORROSION TESTING	32
3.5 MAS #1 THERMAL EXPANSION BEFORE AND AFTER 150 HOURS OF ACCELERATED CORROSION TESTING	33
3.6 MAS #2 THERMAL EXPANSION BEFORE AND AFTER 150 HOURS OF ACCELERATED CORROSION TESTING	34
3.7 MAS #3 THERMAL EXPANSION BEFORE AND AFTER 150 HOURS OF ACCELERATED CORROSION TESTING	35
3.8 THERMAL CONDUCTIVITY OF VARIOUS MATERIALS	49
3.9 ABUNDANCE OF ELEMENTS IN THE EARTH'S CRUST	51
4.1 SCHEMATIC OF SOLID-STATE MATERIAL TRANSPORT	57
4.2 SINTERING RATE AS A FUNCTION OF TEMPERATURE AND TIME	59
4.3 SINTERING RATE AS A FUNCTION OF LOGARITHMIC TEMPERATURE AND TIME	60

	<u>PAGE</u>
4.4 MODEL FOR SINTERING PROCESS	62
4.5 SCHEMATIC DRAWING OF POLYCRYSTALLINE SPECIMEN	67
4.6 ELEVATED TEMPERATURE STRENGTH OF SiC AND Si ₃ N ₄	73
4.7 WEIGHT GAIN IN AIR AT 1380°C OF SINTERED Si ₃ N ₄ AND SiC	76
4.8 CORROSION-EROSION BEHAVIOR OF SILICON CARBIDE AND SILICON NITRIDE	77
4.9 POSSIBLE MODES OF BEHAVIOR OF SiC IN GAS-MOLTEN-GAS ENVIRONMENTS	80
4.10 OXIDE THICKNESS VERSUS OXIDATION TIME	83
4.11 OXIDATION WEIGHT GAIN VERSUS TIME 1/2 FOR SINTERED ALPHA SiC	85
4.12 OXIDATION ISOTHERMS FOR POLYCRYSTALLINE SiC IN OXYGEN AT TEMPERATURES FROM 1297°C TO 1697°C	86
4.13 TRANSITION PRESSURES FOR SiC ACTIVE-PASSIVE OXIDATION VERSUS TEMPERATURE	91
4.14 THERMAL CONDUCTIVITY OF SiC	96
4.15 THERMAL CONDUCTIVITY OF Si ₃ N ₄	97
5.1 BASIC STEPS FOR THE CERAMIC FABRICATION PROCESS	101
5.2 BALL MILL	104
5.3 TYPICAL COATED PAPER WRAPPING OPERATION	107
5.4 TYPICAL CALENDERING OPERATION	108
5.5 TYPICAL EXTRUSION OPERATION FOR FABRICATING A CERAMIC REGENERATOR	110
5.6 CHANGES IN TEMPERATURE, WEIGHT LOSS, AND RELATIVE HUMIDITY DURING DRYING CYCLE	112

	<u>PAGE</u>
5.7 MAS MANUFACTURING PROCESS STEPS	119
6.1 PASSAGE GEOMETRIES	125
6.2 STANDARD THERMODYNAMIC PERFORMANCE CHARACTERISTICS	127
6.3 ALTERNATE THERMODYNAMIC PERFORMANCE CHARACTERISTICS	129
6.4 THERMODYNAMIC PERFORMANCE CHARACTERISTICS FOR HEXAGONAL PASSAGE	132
6.5 THERMODYNAMIC PERFORMANCE CHARACTERISTICS FOR CIRCULAR PASSAGE	133
7.1 COST BREAKDOWN FOR SUPERALLOY AND CERAMIC BASED PRODUCTS	141

LIST OF TABLES

	<u>PAGE</u>
1.1 CORROSION RESISTANCE OF SUPERALLOYS AND CERAMICS	20
2.1 FIGURE OF MERIT FOR CERAMIC MATERIALS ANALYZED FOR THE LOWER TEMPERATURE RANGE	25
3.1 MATRIX DIMENSIONAL CHANGE AFTER 1008 HOUR EXPOSURE AT TEST TEMPERATURE WITH AND WITHOUT SODIUM PRESENT	38
3.2 MATRIX THERMAL EXPANSION AT TEST TEMPERATURE AFTER 1008 HOUR EXPOSURE WITH AND WITHOUT SODIUM PRESENT	39
3.3 THERMAL SHOCK RESISTANCE PARAMETERS	40
3.4 THERMAL SHOCK PARAMETERS FOR MAS, LAS AND AS	42
4.1 SINTERING MECHANISMS	56
4.2 FIGURE OF MERIT FOR CERAMIC MATERIALS ANALYZED FOR THE HIGHER TEMPERATURE RANGE	72
4.3 OXIDATION RATE CONSTANTS	87
4.4 OXIDATION OF POLYCRYSTALLINE SILICON CARBIDE	89
4.5 THEORETICAL VALUES OF EQUILIBRIUM PARTIAL PRESSURE, $P_{\text{SiO}}(\text{eq})$ AND MAXIMUM OXYGEN PARTIAL PRESSURE, $P_{\text{O}_2}(\text{max})$ FOR REMOVAL OF ALL THE OXIDE ON Si_3N_4 AND SiC SURFACES	92
4.6 THERMAL SHOCK PARAMETERS FOR SINTERED Si_3N_4 AND SiC	94
5.1 MAJOR TECHNIQUES FOR POWDER CONSOLIDATION AND SHAPE FORMING	106
6.1 MATRIX CONFIGURATION DATA FOR FIGURE 4.2	128
6.2 MATRIX CONFIGURATION DATA FOR FIGURE 4.3	130
6.3 PASSAGE GEOMETRY COMPARISON	135
8.1 THERMAL AND MECHANICAL PROPERTIES OF MAS	145
8.2 THERMAL AND MECHANICAL PROPERTIES OF $\alpha\text{-SiC}$	146

CHAPTER 1

BACKGROUND

With the current and projected energy conservation requirements, the use of heat exchangers or regenerators to recover waste heat is growing in importance. A good possible material for the regenerator is a ceramic based material. This is the situation currently faced by the gas turbine industry. The progress of the gas turbine engine has been consistently delayed by the lack of good high temperature stable materials. Even in the early days of the jet engine, the lack of appropriate metal alloys was an important obstacle. Today, the availability of a number of metal superalloys enables the gas inlet temperatures to reach temperatures of 980° to 1040°C . Even at this temperature level, however, the overall fuel air ratio is lean and therefore, from a combustion aspect, there is considerable potential for a further increase in the turbine inlet temperature. In the aircraft industry, as a means of increasing turbine inlet temperature, air cooling techniques for both stationary and rotating high temperature components are under current development and experimental engines have been operated with turbine inlet temperatures in excess of 1650°C . These techniques however, do not rely on a material solution, but rather on

directing cooling air on critical high temperature parts. The application of air cooling techniques to small gas turbines is greatly complicated by the small size of the components, and, the possibility of employing uncooled ceramics in place of air cooled metals becomes a very attractive prospect, from the point of view of engine efficiency (fuel savings), size and cost.

In view of their potential, the gas turbine industry is currently investigating the application of ceramics to the gas turbine engine at a number of laboratories. The relatively higher melting points, lower densities, superior oxidation and thermal shock resistance, and mechanical strength enhance the overall attractiveness of ceramic materials as components (such as the regenerator) in the gas turbine engine.

In a similar manner, it is the ability of ceramic components to operate at higher temperatures which allows for the design and operation of an adiabatic (zero heat transfer) diesel engine. Adiabatic diesel engines currently use ceramic materials for the following engine parts:

1. Insulated piston cap.
2. Insulated "hot plate" for the cylinder head.
3. Insulated cylinder liner.
4. Insulated exhaust parts.
5. Insulated exhaust manifolds, valves and injectors.

With no heat transfer requirement, adiabatic diesel engines have eliminated the requirement for the radiator fan, water pump, water and associated metal in the block needed only for the cooling water, thus yielding a major weight and cost savings. All of the power previously wasted by parasitic losses is now available as horsepower, thereby decreasing the specific fuel consumption (SFC) of the diesel engine. The elimination of the entire water cooling system will significantly reduce maintenance and repair costs over the life cycle of the engine. A completely insulated engine with components made of glass ceramics will reduce heat rejection by approximately 80 percent and much of this energy can be recovered by the use of turbo-compounding.

Therefore, for both gas turbine and adiabatic diesel engines, ceramic components are being utilized to improve SFC, which in turn improves engine efficiency by causing an increase in engine peak temperatures. Figure 1.1 illustrates this tendency for gas turbine engines. However, though Figure 1.1 details this conclusion for gas turbine engines, the analogy can be extended to adiabatic diesel engines and a new cycle design being developed in the Ocean Engineering Department at the Massachusetts Institute of Technology.

The new cycle has two working cylinders, one for compression and the other for expansion. One arrangement

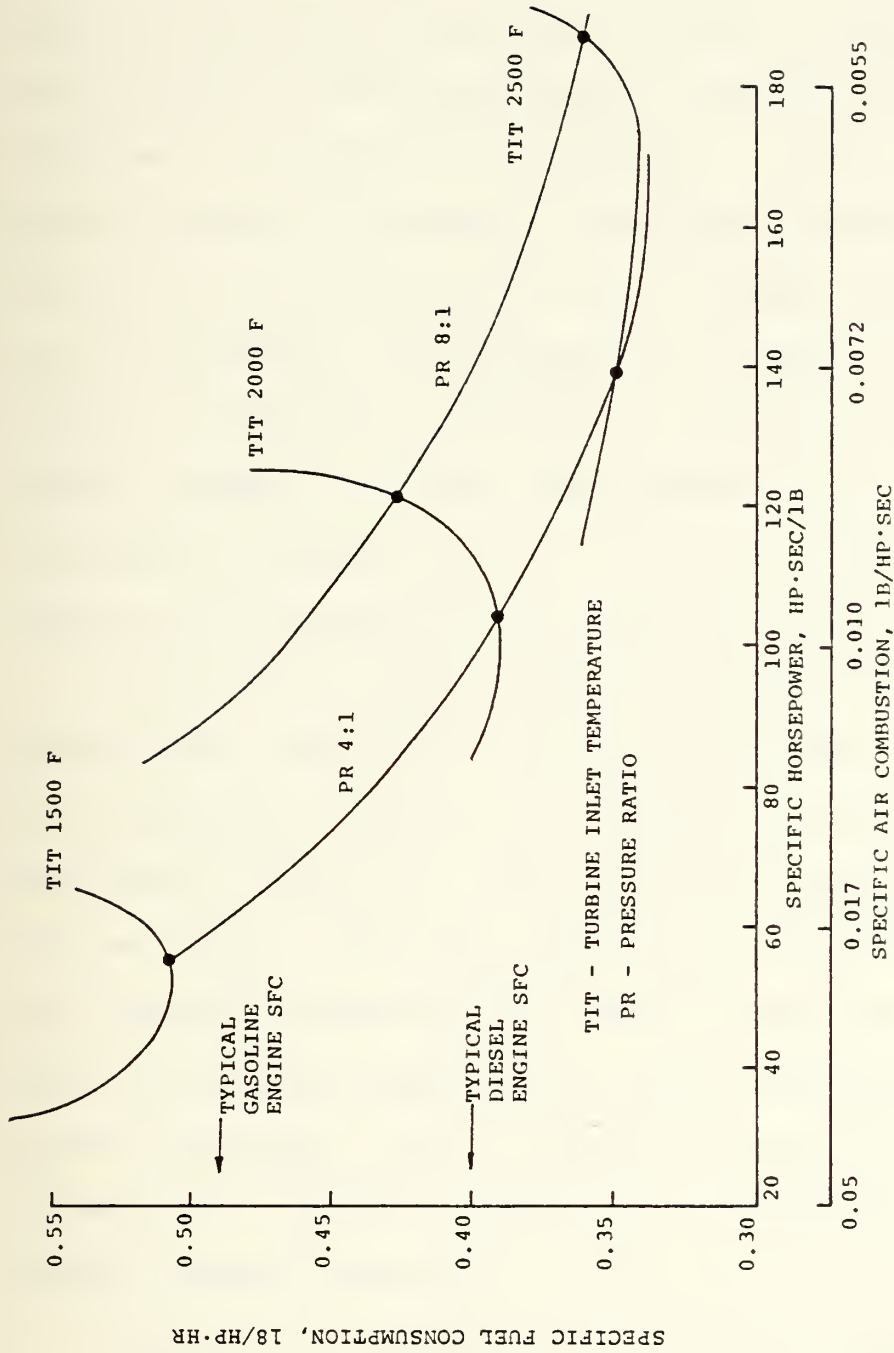


FIGURE 1.1: REGENERATIVE GAS TURBINE - SPECIFIC AIR AND FUEL CONSUMPTIONS

has a double-speed compression cylinder design with two expansion cylinders. Preliminary calculations of the expansion/combustion stroke and exhaust stroke of the new cycle produce pressure-volume and temperature-volume diagrams as illustrated in Figures 1.2 and 1.3. To improve engine efficiency, a stationary regenerator, designed to recover heat from the exhaust gases of the new cycle and preheat the compressed air entering the expansion/combustion cylinder, is conceptualized to be located between and above the expansion and compression cylinders. Figures 1.4 and 1.5 provide a schematic of the regenerator placement in the new cycle engine design.

The service limit of metallic regenerators is approximately $850-900^{\circ}\text{C}$ in clean environments with little or no corrosive gases in the exhaust gas stream. As detailed in Figure 1.3, the exhaust gas temperatures of the new engine are of the order of $1050-1100^{\circ}\text{C}$ and due to the inherent contaminants in diesel fuel, the exhaust gases will be too corrosive for metal regenerators. It appears therefore, that a suitable material for the regenerator of this new engine is a high temperature capable ceramic material.

However, do high temperature ceramic materials have the potential to replace superalloys? By comparing basic properties of some selected superalloy metals used for high temperature engine components with selected ceramic

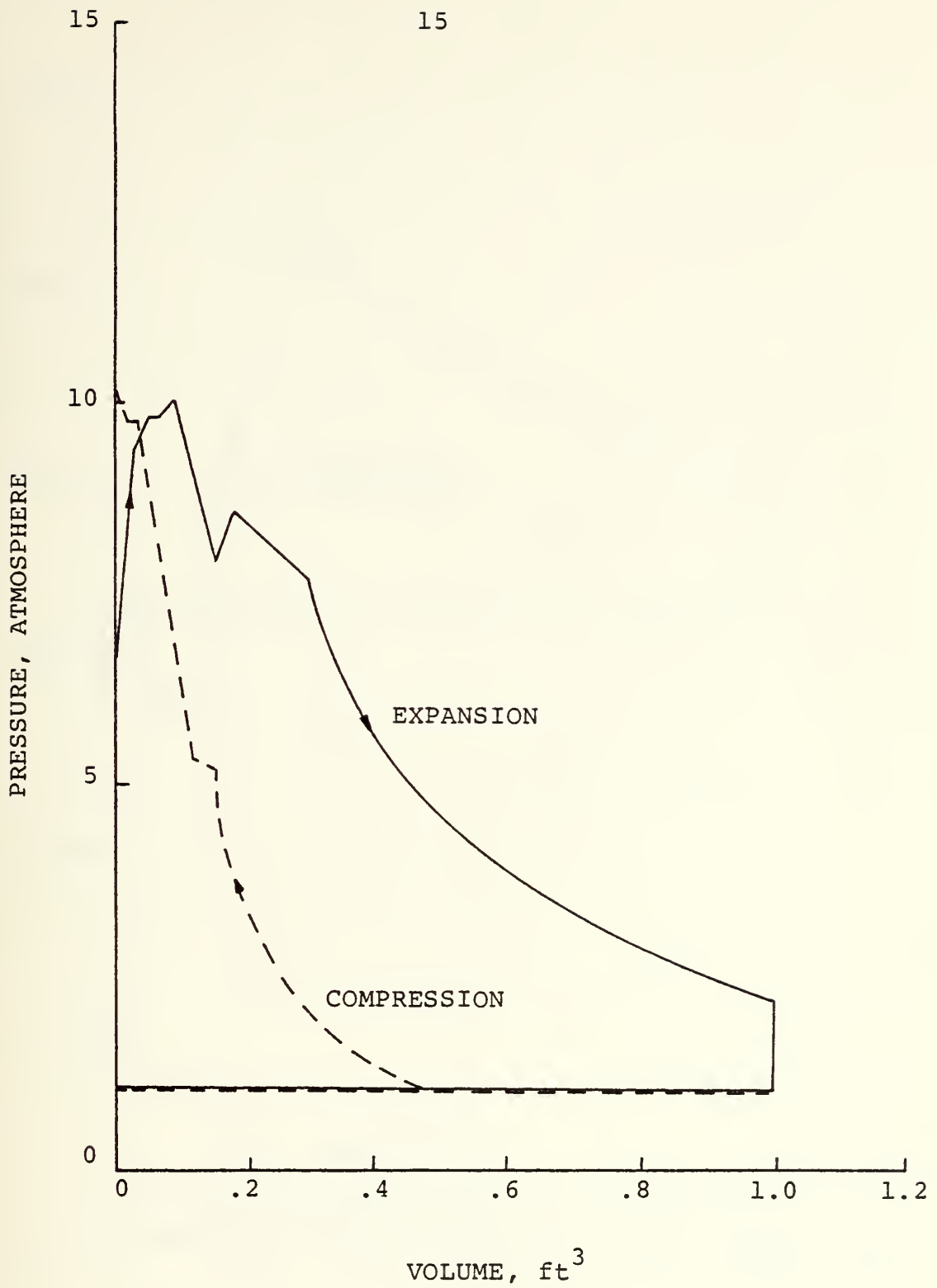


FIGURE 1.2: PRESSURE-VOLUME DIAGRAM OF NEW ENGINE

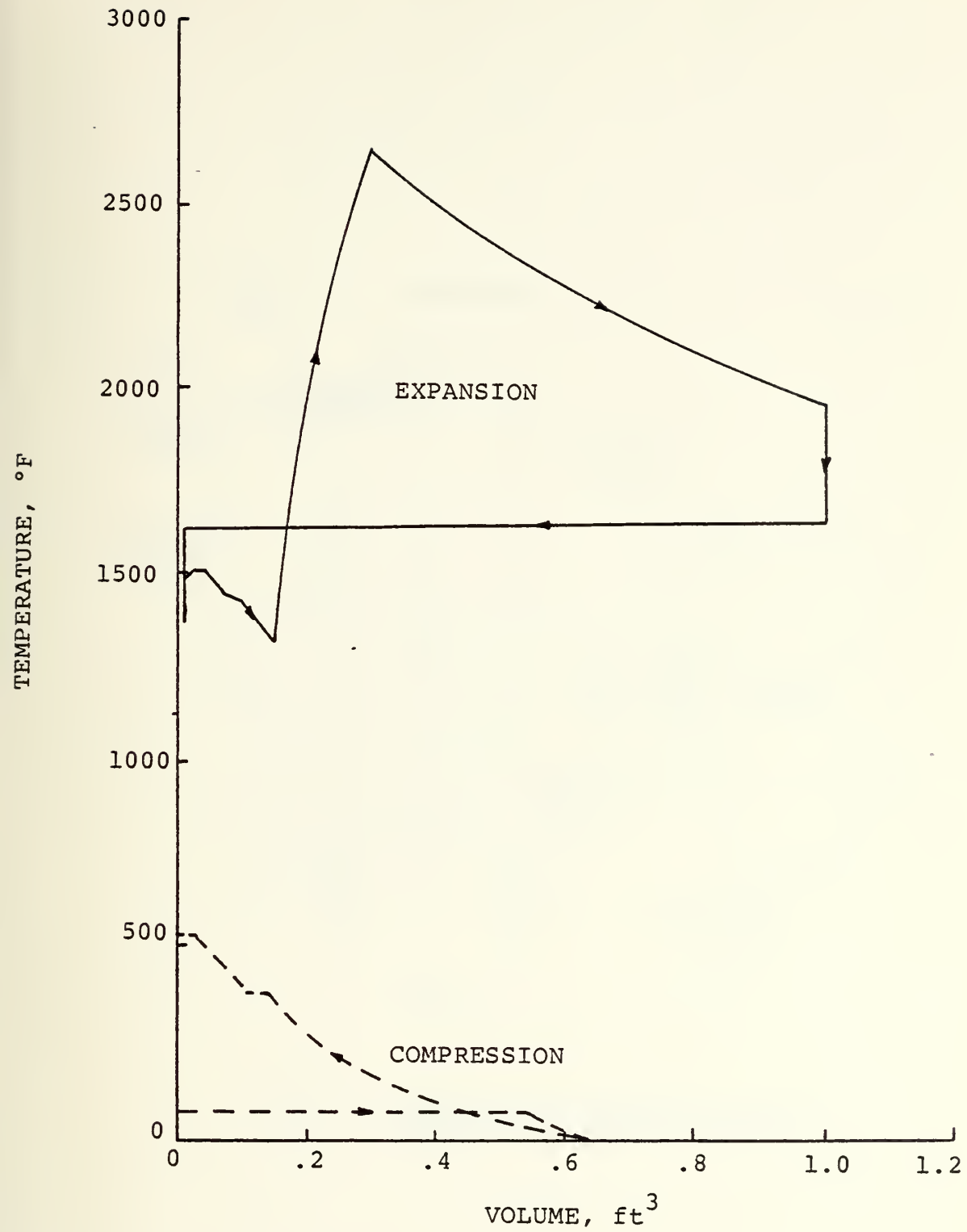


FIGURE 1.3: TEMPERATURE - VOLUME DIAGRAM OF NEW ENGINE

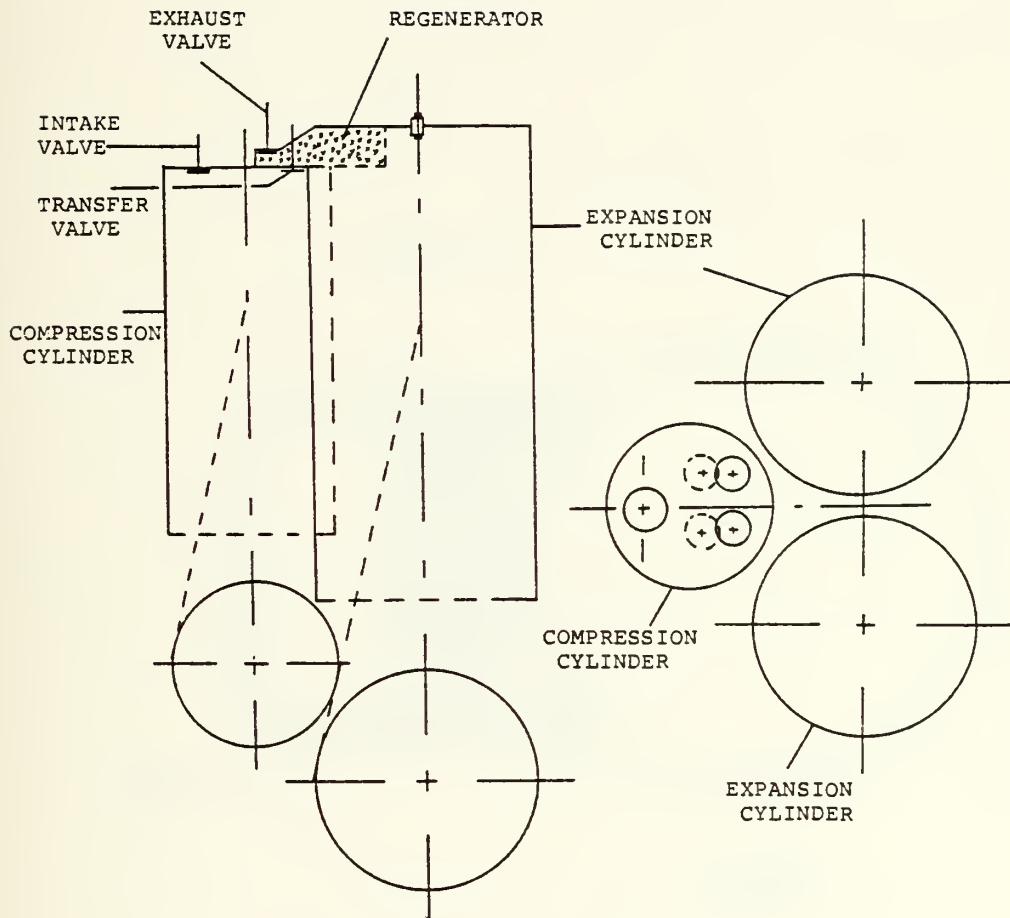


FIGURE 1.4: ARRANGEMENT OF THE COMPONENTS FOR THE DOUBLE-SPEED COMPRESSION CYLINDER DESIGN, IN-LINE ENGINE

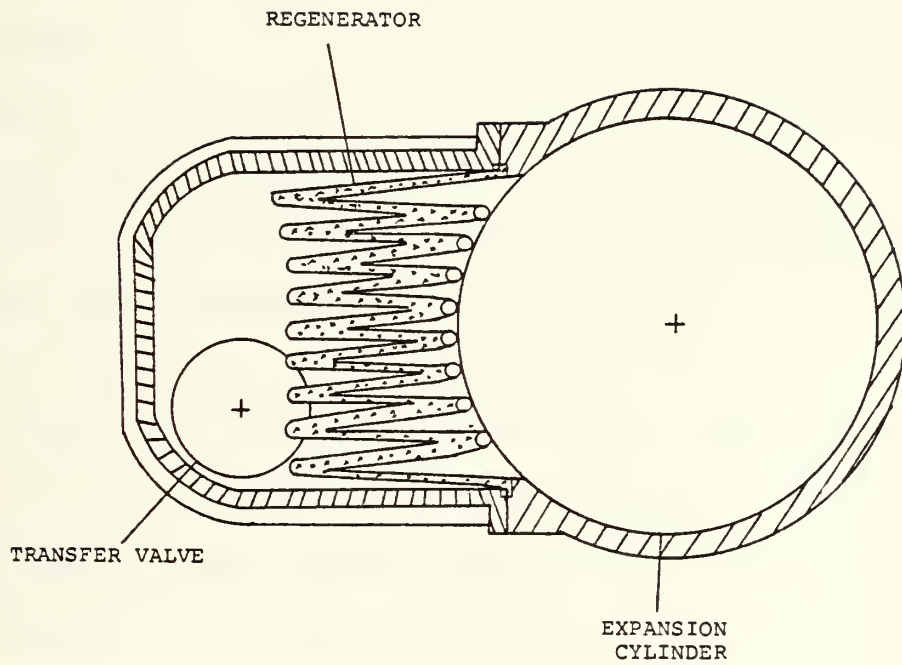


FIGURE 1.5: REGENERATOR ARRANGEMENT

materials, the following observations can be made directly from this comparison:

Metal melting point < Ceramic melting point

Metal thermal conductivity > Ceramic thermal conductivity

Metal expansion > Ceramic expansion

Metal density > Ceramic density

As detailed later, the above properties of ceramic materials are all desired qualities of the new cycle regenerator.

Table 1.1 indicates qualitatively the corrosion resistance data of several ceramic materials and representative superalloys. In general, the ceramic materials with the exception of graphite exhibited better corrosion resistance than the superalloys at typical engine operating conditions. Figure 1.6 compares raw material costs of superalloys and ceramics. The general observation is that ceramic materials cost much less than superalloys and therefore, if used for a high-temperature regenerator, ceramic materials would effect dramatic raw material cost savings.

In light of the above advantages of ceramics to superalloys, the following areas of research were conducted: (1) determine candidate ceramic materials and their properties for the regenerator of the new cycle engine; (2) fabrication techniques required to manufacture

MATERIAL	OXIDATION RESISTANCE (1093°C)	CORROSION Severe Molten Salt Test	RESISTANCE Simulated Engine Tests	EROSION RESISTANCE (Hardness, MOHS)
<u>CERAMICS</u>				
Silicon Nitride	B	C	B	9+
Silicon Carbide	B	C	B	9.6
Lithium-Aluminum- Silicate	A	A	A	6
<u>SUPERALLOYS</u>				
MAR-M-246	B	D	-	
INCO T13	B	D	-	
TRW 6A	B	C	-	

- A = NO ATTACK
 B = SLIGHT ATTACK
 C = MODERATE TO HEAVY ATTACK
 D = SEVERE ATTACK OR DESTRUCTION

TABLE 1.1: CORROSION RESISTANCE OF SUPERALLOYS AND CERAMICS

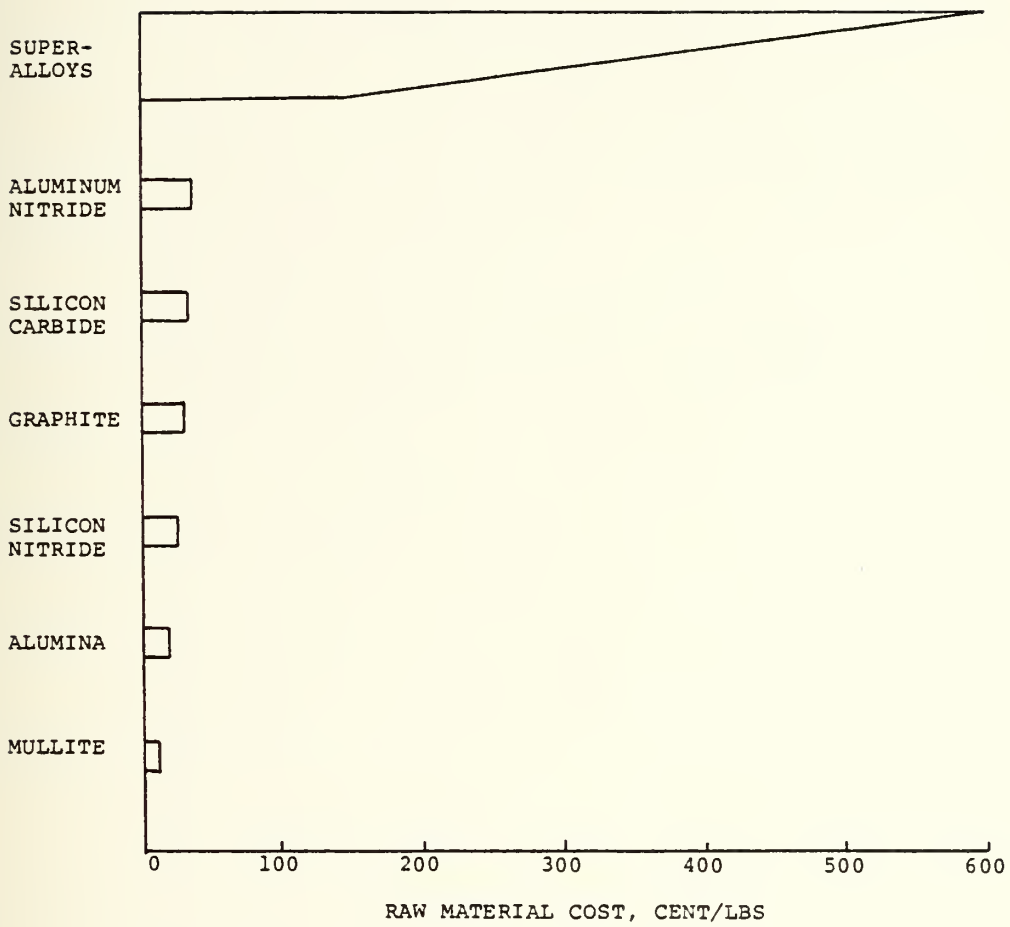


FIGURE 1.6: RAW MATERIAL COSTS OF HIGH-TEMPERATURE MATERIALS

the ceramic regenerator; (3) passage geometry design of the regenerator matrix; and (4) cost analysis of manufacture and processing of the candidate ceramic materials. -

INTRODUCTION

Numerous investigators have described the important design requirements of the material used in fabricating a regenerator for gas turbines and industrial regenerators and air preheaters (1, 2, 3, 4, 5, 6). Though each investigator may emphasize one particular parameter of the ceramic material to be most important, the following list is a summation of the accepted desirable parameters of a regenerator ceramic material.

1. Strength at the working temperatures (both the compressed air temperature and exhaust gas temperature).
2. Corrosion resistance at the working temperatures.
3. Thermal shock resistant.
4. Low thermal conductivity.
5. Material's ability to be fabricated to desired shape and design.
6. Economically competitive with existing regenerator materials.

All of these parameters however, are not of equal importance in the design of the regenerator for the new cycle. To assist in selecting the most desirable ceramic material that best meets all of the parameters previously mentioned, each ceramic material was analyzed using a

figure of merit scheme. Table 2.1 lists the weighting factors for each of the ceramic materials analyzed for operating temperatures up to 1200°C .

It is noteworthy to mention that the literature search conducted clearly established two distinct temperature groups of ceramics that were of interest to investigators as possible structural components such as a regenerator. One temperature group includes ceramics which experimentally performed well up to approximately 1200°C and the other temperature group includes ceramics which performed reasonably well up to about 1400°C . In light of the above and because of the expected tendency for exhaust temperatures to continually increase to improve engine efficiency, the selection of two candidate ceramic materials was performed. One satisfying the temperature regime up to 1200° (the ceramic material recommended for the new engine), the other satisfying the temperature regime from 1200°C to 1400°C (the ceramic material recommended to meet the requirements of future, higher temperature operating engines).

PARAMETER	WEIGHTING FACTOR	CERAMIC MATERIAL			
		MAS RATING VALUE	LAS RATING VALUE	AS RATING VALUE	
STRENGTH	10	3	30	2	20
CORROSION RESISTANCE	10	3	30	1	10
THERMAL SHOCK	7	3	21	2	14
THERMAL CONDUCTIVITY	7	2	14	2	14
FABRICABILITY	10	2	20	2	20
COST	10	3	30	2	20
			145		98
					74

TABLE 2.1: FIGURE OF MERIT FOR CERAMIC MATERIALS ANALYZED FOR THE LOWER TEMPERATURE RANGE

CHAPTER 3

CERAMIC MATERIALS ANALYZED FOR OPERATING
TEMPERATURES UP TO 1200°C3.1 Introduction

As previously mentioned, two distinct temperature groups of ceramics consistently appeared in the literature as possible regenerator materials. The ceramic materials that recurred continually in the discussion as candidate regenerator materials for gas temperatures up to 1200°C were magnesium aluminum silicate (MAS), lithium aluminum silicate (LAS), and aluminum silicate (AS). (3, 4, 7, 8, 9, 10, 11, 12, 13, 14).

3.2 LAS, AS and MAS

The initial material selected for development (by the Corning Glass Works and Owens-Illinois) was LAS because of its near-zero coefficient of thermal expansion (α) and the resulting extremely good thermal shock resistance.

Thermally, LAS worked fine, but a corrosion problem was identified during engine testing (4). Apparently, alkali lithium ions Li^+ react readily with hydrogen ions H^+ from the sulfuric acid in the engine exhaust and/or with sodium ions Na^+ found in the marine environment and exhaust gases. This ion exchange affected the regenerator structurally since Na^+ and H^+ ions are of different ionic

sizes compared to the replaced Li^+ ion. The larger Na^+ ion caused the structure to expand and coupled with the large regenerator surface area available for their reaction, this increased the matrix bulk volume of the regenerator. On the other hand, the smaller H^+ ion caused a corresponding contraction of the matrix bulk volume. Data from reference (4) indicate that prolonged exposure to dilute sulfuric acid solutions lead to material expansion followed by contraction which ultimately lead to microcracking of the regenerator matrix.

Work at Corning Glass, the manufacturer of the LAS core material, resulted in a procedure to remove the lithium oxide from LAS by leaching in hot sulfuric acid the LAS honeycomb regenerator matrix. The resulting AS material had acceptable thermal expansion properties and did not distort or crack in the engine under normal operating conditions.

MAS was developed and selected as a possible regenerator material because this compound combines relatively low thermal expansion with relatively good high temperature parameters.

3.3 Thermal Stability Comparison of LAS, AS and MAS

To analyze the capabilities of each of these regenerator materials, the Ford Motor Company, in association with the Department of Energy and the National Aeronautics and Space Administration, undertook the task

of testing these regenerator materials under normal gas turbine engine operating conditions. The results indicate clearly the superiority of the MAS regenerator matrix to both the AS and LAS matrices in gaseous environments containing sulfur and sodium by-products. Figures 3.1 and 3.2 illustrate that both MAS and LAS materials are practically immune to sulfuric acid attack at 315°C and 800°C , respectively. Tests conducted under sodium chloride contaminated exhaust gases resulted in AS and LAS undergoing significant changes in size as a result of 150 hours of exposure to accelerated corrosion testing. See Figures 3.3 and 3.4. The reasons for the AS and LAS matrices performing poorly under these test conditions is because when the lithium ion of these materials is replaced, this exchange results in a "stuffing" of the crystalline lattice due to the size disparity between Na^{+} and Li^{+} ions. This resultant ionic displacement creates a lattice deformed by residual strain, thereby changing the reaction of the unit cell to changes in temperature. The degree of change varies with the magnitude of the ion exchange, as evidenced by the more pronounced change observed in the LAS material compared to the AS material.

The MAS regenerators on the other hand are impervious to ion exchange and proved practically immune to the corrosion attack under normal engine operating conditions as evidenced by Figures 3.5, 3.6, and 3.7. For these reasons, the relative ratings for these three ceramic

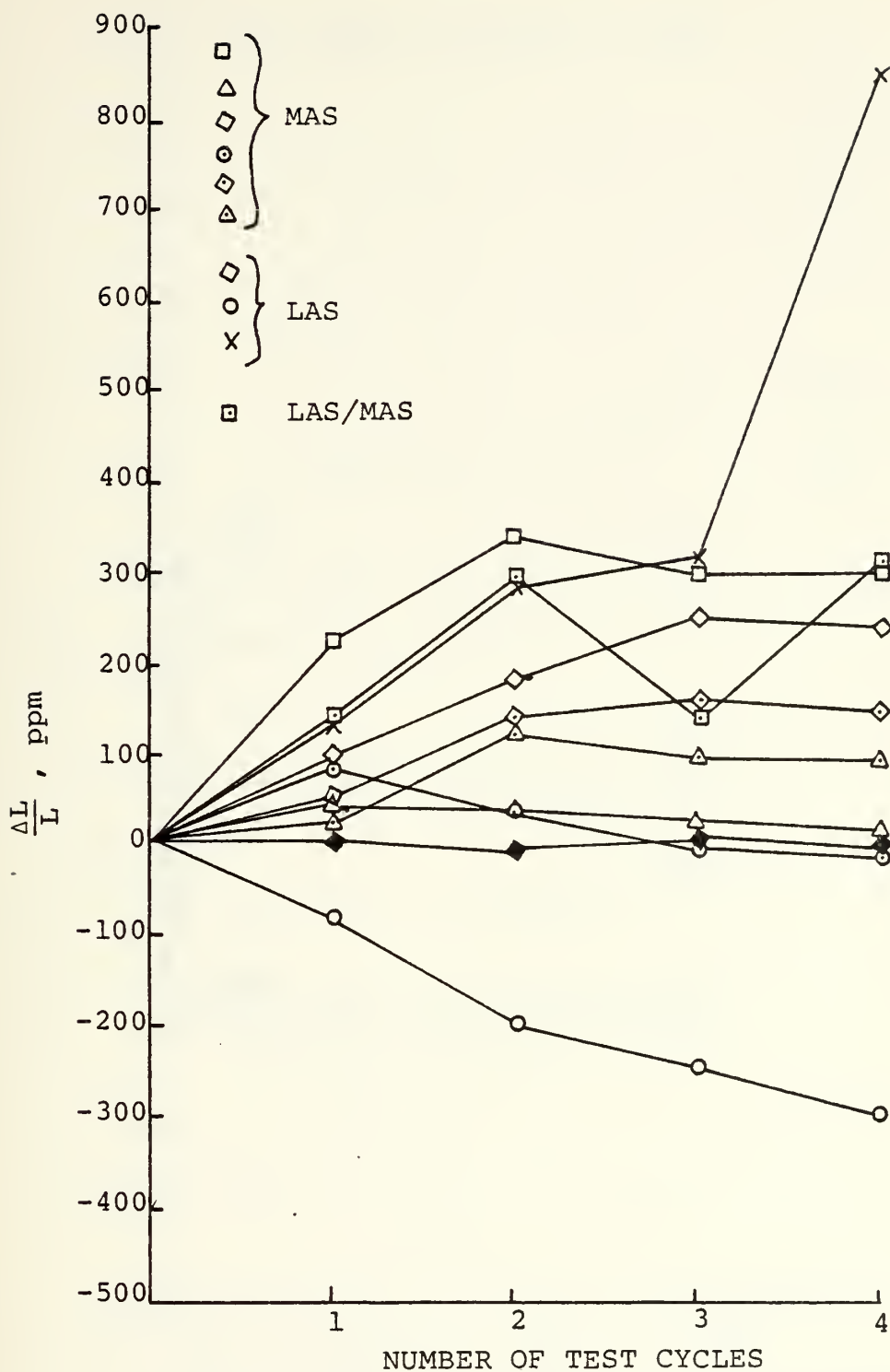


FIGURE 3.1: PHYSICAL STABILITY OF VARIOUS MATERIALS AT 315°C

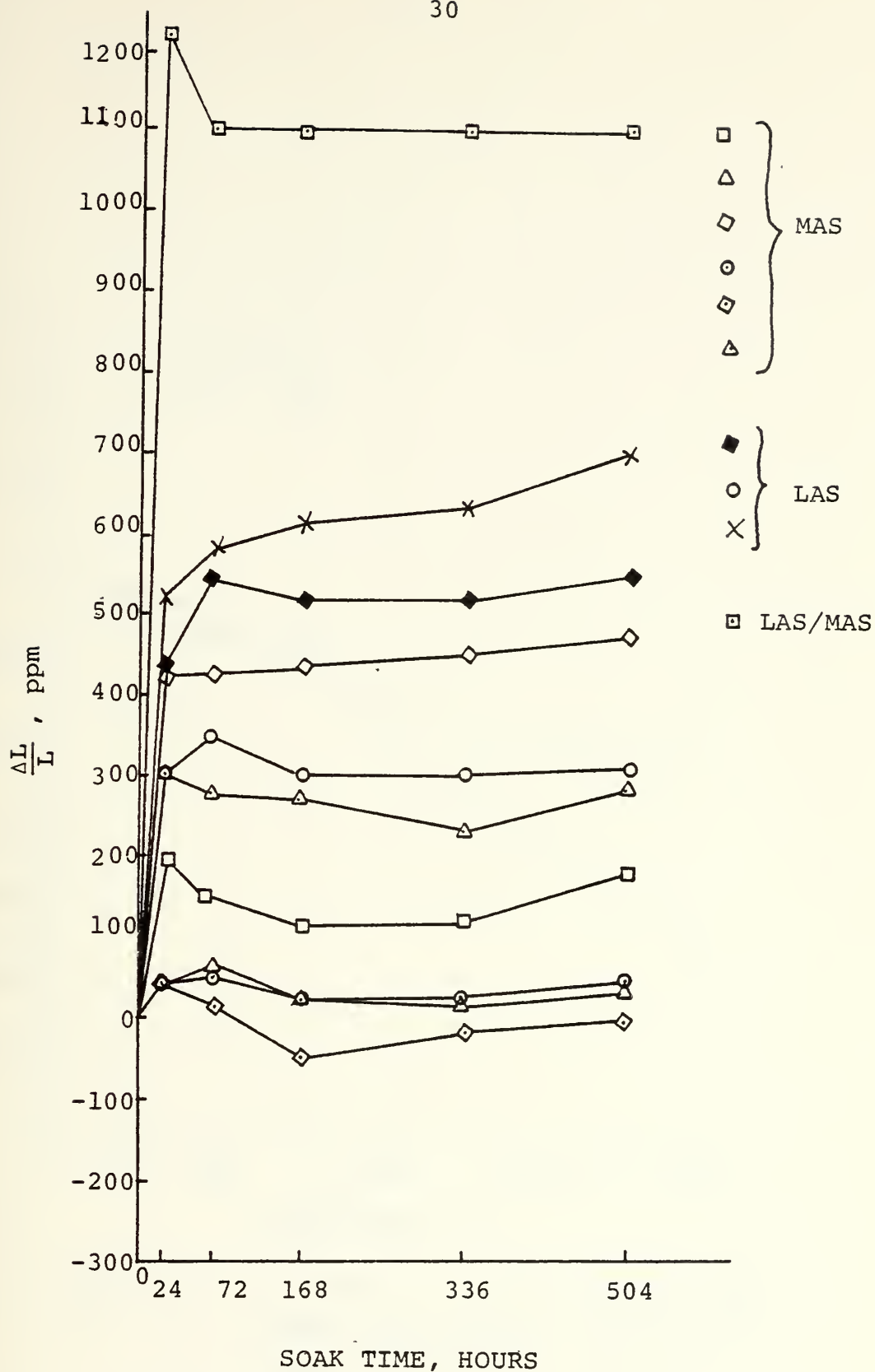


FIGURE 3.2: PHYSICAL STABILITY OF VARIOUS MATERIALS AT 800°C

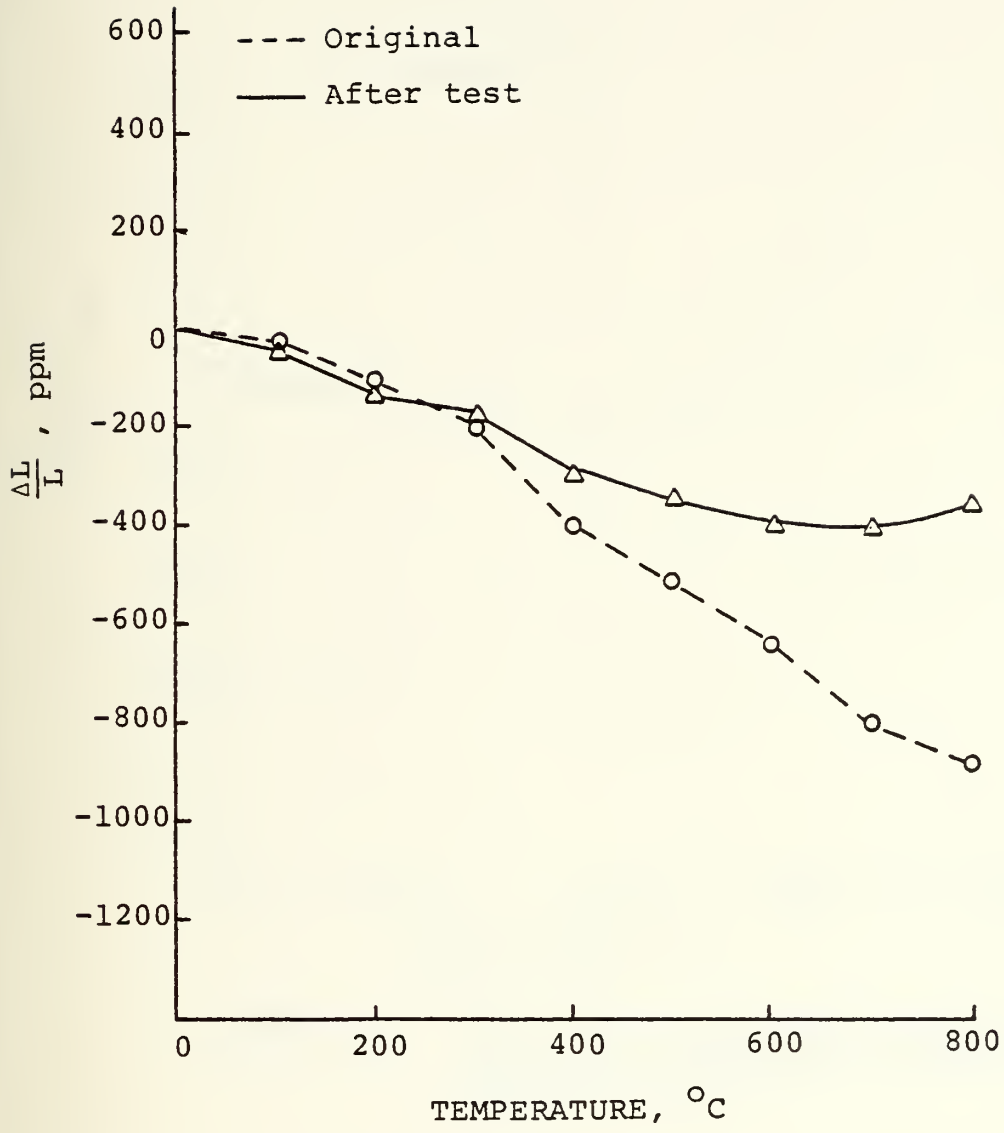


FIGURE 3.3: AS THERMAL EXPANSION BEFORE AND AFTER 150 HOURS OF ACCELERATED CORROSION TESTING

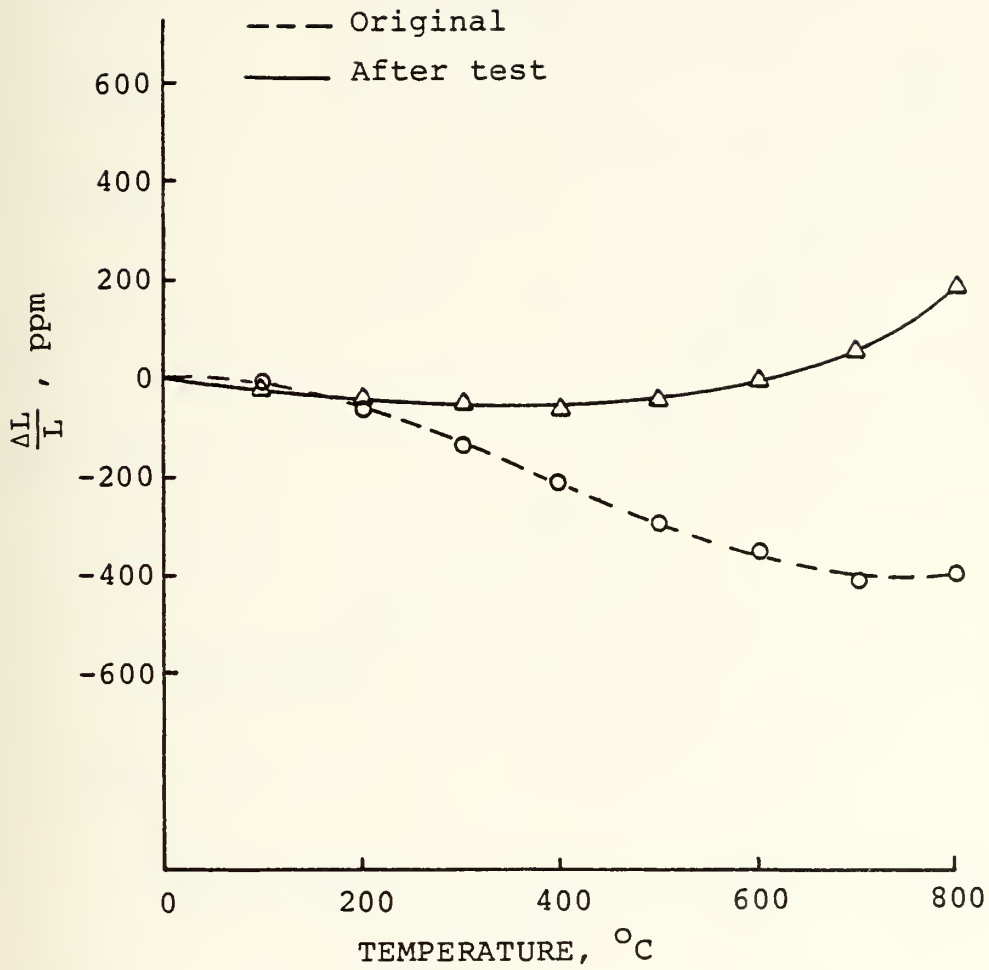


FIGURE 3.4: LAS THERMAL EXPANSION BEFORE AND AFTER 150 HOURS OF ACCELERATED CORROSION TESTING

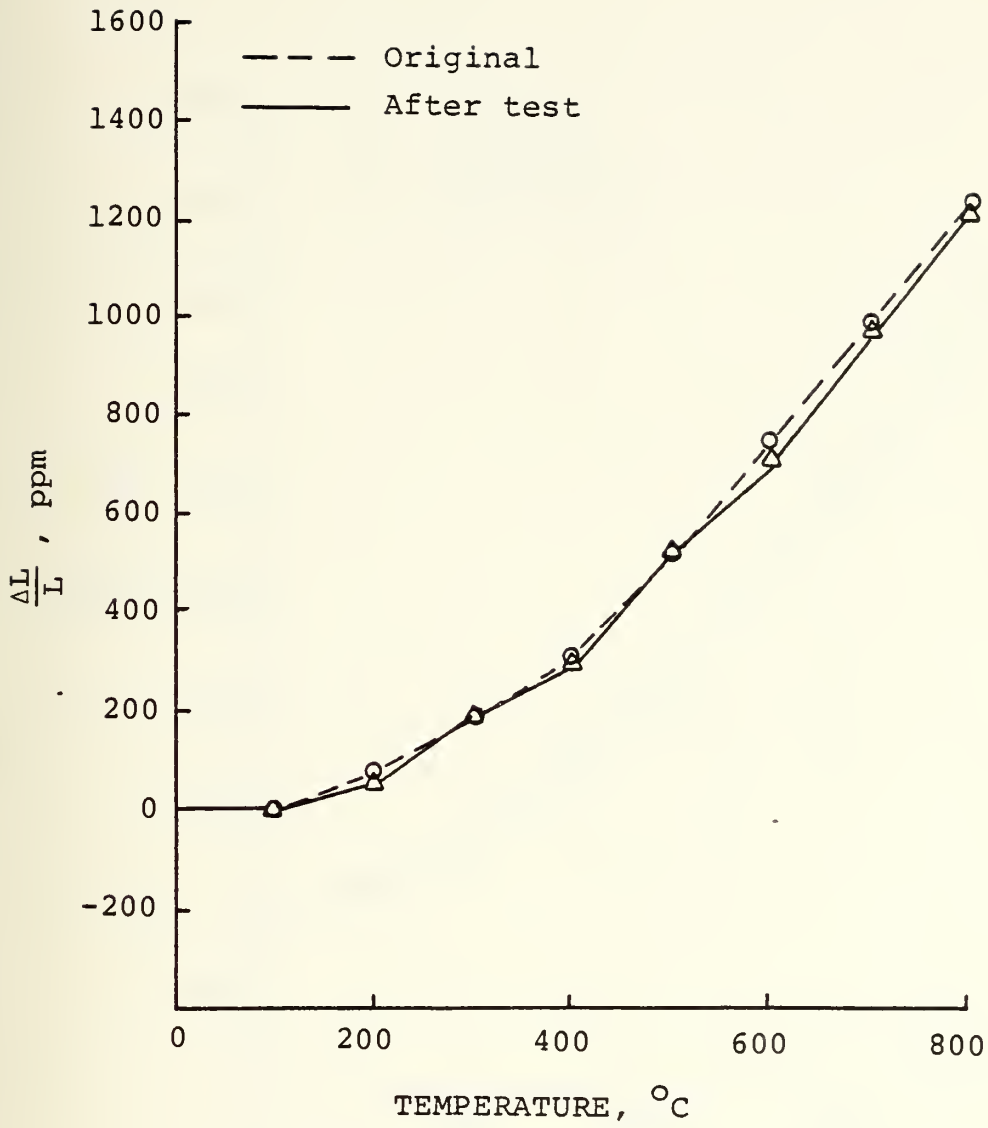


FIGURE 3.5: MAS #1 THERMAL EXPANSION BEFORE AND AFTER 150 HOURS OF ACCELERATED CORROSION TESTING

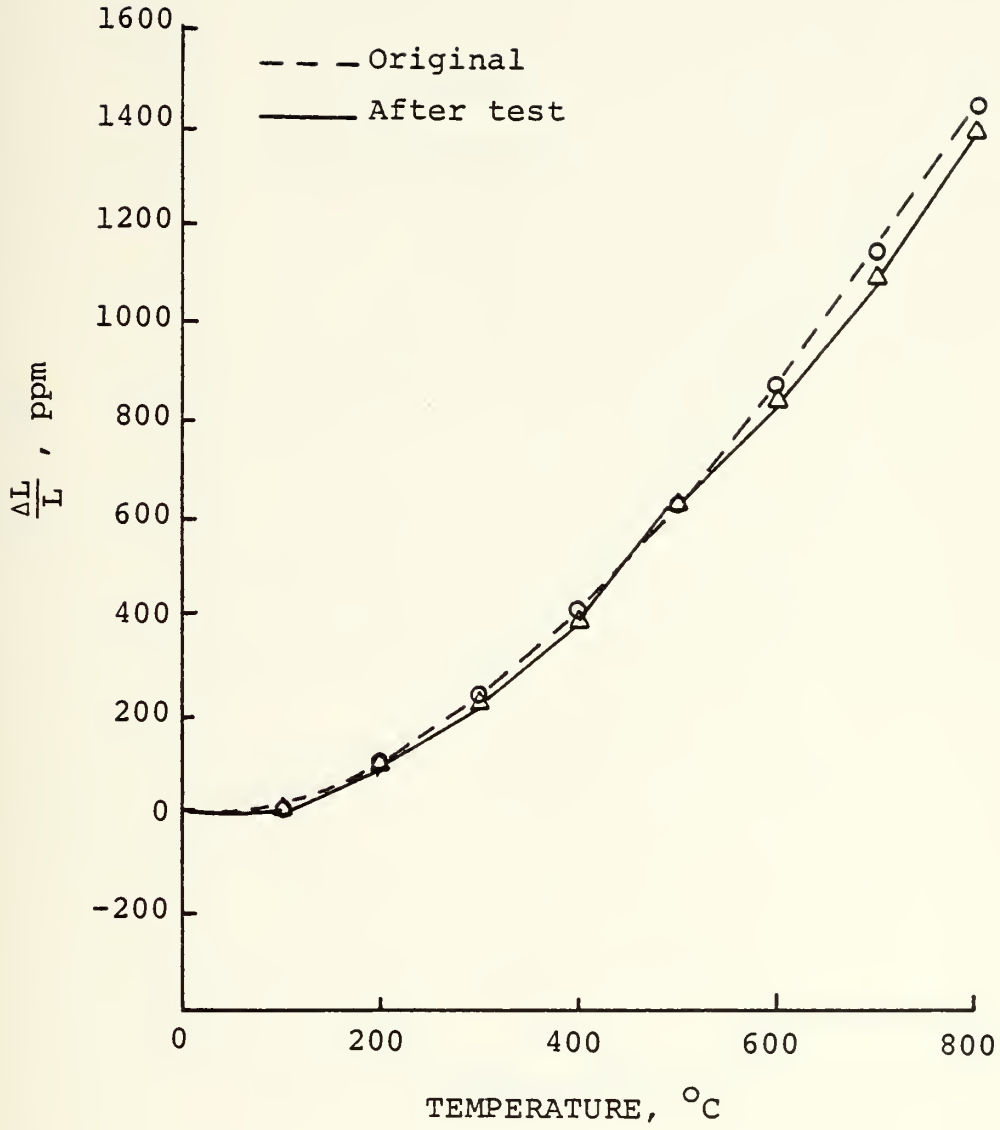


FIGURE 3.6: MAS #2 THERMAL EXPANSION BEFORE AND AFTER 150 HOURS OF ACCELRTED CORROSION TESTING

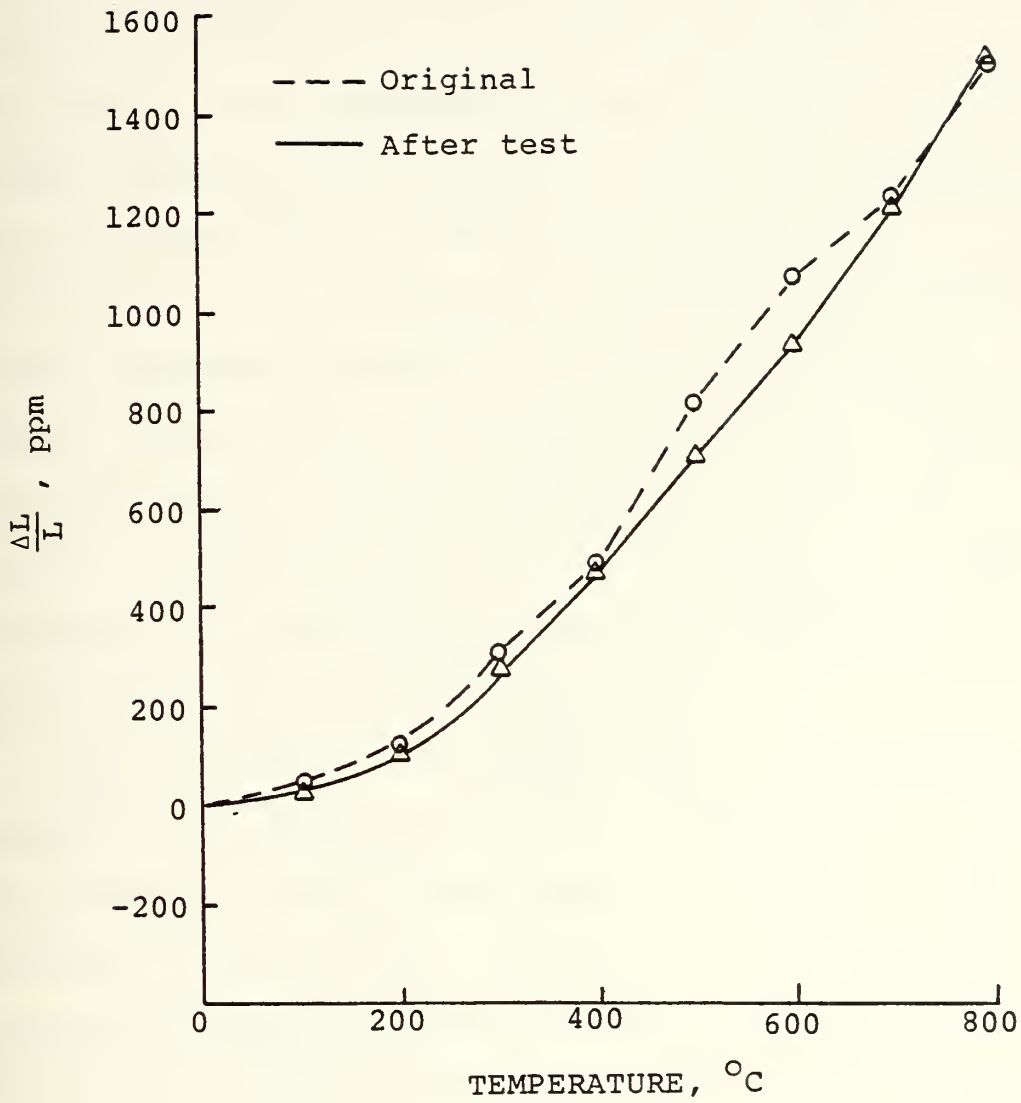


FIGURE 3.7: MAS #3 THERMAL EXPANSION BEFORE AND AFTER 150 HOURS OF ACCELERATED CORROSION TESTING

materials for their corrosive characteristics are given in Table 2.1.

Thermal stability data from references (4) and (15) clearly establish that the cordierite type MAS material regenerator offers the best potential for 1200°C application. The dimensional change (Table 3.1) and thermal expansion characteristics (Table 3.2) compared all three material types in sodium environments from 1000°C-1200°C. It is immediately apparent that the AS material undergoes unstable shrinking and undergoes extreme sodium corrosion at temperatures above 1000°C. In fact, the drastic changes in dimensions and thermal expansion characteristics of the AS material terminated the testing at temperatures higher than 1000°C prior to the 1008 hour objective of testing (4).

The LAS material fared better than the AS material throughout the temperature range of 1000°C-1200°C, however, the presence of sodium had a significant effect on the dimensional change of LAS. The LAS material expanded beyond the acceptable limits of 450 to 600 ppm (this limit was established by the Ford Motor Company Research staff (4)) in all three temperature steps. The thermal expansion data of LAS indicate that it is more stable than MAS or AS in both the sodium free and sodium contaminated environments.

The MAS material throughout the temperature excursion indicates excellent stability with respect to matrix

DIMENSIONAL CHANGE AFTER 1008 HOUR EXPOSURE (ppm)

<u>MATERIAL</u>	<u>WITHOUT SODIUM</u>			<u>WITH SODIUM</u>		
	<u>1000°C</u>	<u>1100°C</u>	<u>1200°C</u>	<u>1000°C</u>	<u>1100°C</u>	<u>1200°C</u>
LAS	- 80	- 120	-300	1220	550	800
AS	-450	-2250 (672 hours)		- 600	-3070 (168 hours)	-9190 (168 hours)
MAS #1	- 80	400	800	300	600	1050
MAS #2	- 50	- 100	-200	400	275	- 400

TABLE 3.1: MATRIX DIMENSIONAL CHANGE AFTER 1008 HOUR EXPOSURE AT
TEST TEMPERATURE WITH AND WITHOUT SODIUM PRESENT

MATERIAL	INITIAL PPM AT TEST TEMPERATURE			FINAL PPM AT TEST TEMPERATURE AFTER 1008 HOUR EXPOSURE					
	1000°C	1100°C	1200°C	WITHOUT SODIUM			WITH SODIUM		
				1000°C	1100°C	1200°C	1000°C	1100°C	1200°C
LAS	650	750	1050	725	800	1125	1000	1000	1300
AS	40	100	200	280	930 (672 hours)		400	1100 (168 hrs)	4100 (168 hrs)
MAS	1480	1750	2400	1380	1425	1550	1380	1500	1200
MAS	1800	1950	2250	2100	2025	2500	2100	2200	2300

TABLE 3.2: MATRIX THERMAL EXPANSION AT TEST TEMPERATURE AFTER 1008 HOUR EXPOSURE WITH AND WITHOUT SODIUM PRESENT

dimensional change. The MAS material not only proved impervious to the presence of sodium, but also had the smallest absolute values for dimensional change. Though MAS did not have the smallest thermal expansion data, the presence of sodium had the slightest effect on the thermal expansion of MAS compared to LAS and AS. The data of Tables 3.1 and 3.2 establish the guidelines for the relative ratings of the three materials for the strength at working temperature parameter of Table 2.1.

3.4 Thermal Shock Resistance Comparison of LAS, AS and MAS

Thermal shock resistance comparisons between the three ceramic materials is a measure of the materials ability to resist fracture or the propagation of cracks due to the thermal stresses that occur in a component (regenerator matrix) as a result of exposure to a temperature difference between the surface and interior or between various regions of the regenerator matrix.

Table 3.3 lists the various thermal shock resistance parameters currently utilized in analyzing the ability of ceramics to resist thermal shock. It is noteworthy that the effects of E , Young's modulus, σ flexural strength, ν , Poisson's ratio are opposite for crack initiation versus crack propagation. Low E and ν with high σ provide high resistance to propagation of existing cracks, while high E and ν with low σ provide low resistance to fracture initiation.

PARAMETER DESIGNATION	PARAMETER TYPE	PARAMETER	PHYSICAL INTERPRETATION/ HEAT TRANSFER CONDITION	TYPICAL UNITS
R	Resistance to frac- ture initiation	$\frac{\sigma(1-\nu)}{\alpha E}$	Maximum ΔT allowable for steady heat flow	$^{\circ}\text{C}$
R'	Resistance to frac- ture initiation	$\frac{\sigma(1-\nu)K}{\alpha E}$	Maximum heat flux for steady flow	$\text{cal/cm}\cdot\text{sec}$
R''	Resistance to frac- ture initiation	$\frac{\sigma(1-\nu)\alpha_{\text{TH}}}{\alpha E}$	Maximum allowable rate of sur- face heating	$\text{cm}^2\cdot^{\circ}\text{C/sec}$
R'''	Resistance to propa- gation damage	$\frac{E}{\sigma^2(1-\nu)}$	Minimum in elastic energy at fracture available for crack propagation	$(\text{psi})^{-1}$
R''''	Resistance to propa- gation damage	$\frac{\gamma E}{\sigma^2(1-\nu)}$	Minimum in extent of crack propagation on initiation of thermal stress fracture	cm
R _{St}	Resistance to further crack propagation	$\left[\frac{\gamma}{\alpha E} \right]^{1/2}$	Minimum ΔT allowed for propa- gation long cracks	$^{\circ}\text{C/m}^{1/2}$

σ , Tensile strength; ν , Poisson's ratio; α , Coefficient of thermal expansion;
 E , Young's modulus of elasticity; K , thermal conductivity; α_{TH} , thermal density;
 γ , fracture surface energy

TABLE 3.3: THERMAL SHOCK RESISTANCE PARAMETERS

The procedure, therefore, when selecting a ceramic material for an application where thermal shock is expected to be a problem, is to calculate the appropriate thermal shock parameter for the various candidate materials and determine which material best suits the application. In the new engine cycle, the regenerator is expected to experience steady heat flux throughout the normal operating regime. Therefore, both the R and R' parameters are important. Table 3.4 summarizes the calculation of R and R' using typical material properties for each of the three candidate ceramic materials.

The MAS material is by far the most thermal shock resistant, due entirely to its very low value of modulus of elasticity, E . The LAS material also illustrates good thermal shock resistance, having R and R' values about half that of the MAS material, but twice that of the AS material. The thermal shock resistance of the LAS material is due solely to its very low thermal expansion coefficient, α . For these reasons, the figure of merit ratings are given in Table 2.1.

Increasingly, the effort of regenerator manufacturers toward higher engine efficiencies has resulted in a trend toward thinner wall regenerator matrices. However, as the wall thickness decreases, how are the R and R' parameters affected? Reduction of wall thickness from 0.160 mm to 0.083 mm resulted in a 10 percent reduction in fracture strength with a corresponding 10 percent increase in open

MATERIAL	FLEXURAL STRENGTH σ [psi]	POISSON'S RATIO ν	THERMAL CONDUCTIVITY α [IN/IN·°C]	ELASTIC MODULUS E [psi]	THERMAL CONDUCTIVITY k [CAL/CM·SEC·°C]	R [°C]	R' [CAL/CM·SEC]	σ/E
MAS	16,000	0.2	1.55×10^{-6}	1.01×10^6	0.0026	8,176	21.26	0.0158
LAS	20,000	0.27	0.3×10^{-6}	10×10^6	0.0026	4,867	12.65	0.0020
AS	25,000	0.27	3.12×10^{-6}	10×10^6	0.0095	585	5.56	0.0025

$$R = \frac{\sigma(1-\nu)}{E \alpha}$$

$$R' = \frac{k\sigma(1-\nu)}{E\alpha}$$

Data from references 3, 7, 13, 20, and 21

TABLE 3.4: THERMAL SHOCK PARAMETERS FOR MAS, LAS AND AS

area (14). However, the constant values of strain tolerance σ/E and linear coefficient of thermal expansion for the two wall thickness indicates that variations in wall thickness for the LAS, AS and MAS matrices, do not affect the thermal shock resistant parameters R and R' . In general, therefore when designing for thinner walled ceramic regenerators, since the strain tolerance does not appear to be affected by wall thickness, consideration should be given to lower linear coefficient of thermal expansion and higher fracture strength. This is exactly what makes the MAS material an attractive regenerator material with respect to the thermal shock parameters described in Table 3.4.

3.5 Thermal Conductivity Comparison of LAS, AS and MAS

A desirable parameter of the regenerator is to have a low thermal conductivity value to reduce heat conductive losses in the matrix. To understand, however, how heat conduction takes place in solids is no easy task.

There are two processes by which heat conduction takes place in solids. Energy can be transferred by coupling between lattice vibrations or by electronic movement and collisions with atoms. For dielectric materials, such as ceramics, electrons are not free to move through the structure in appreciable concentrations, and heat is mainly transferred by lattice vibrations. The mechanisms whereby these thermal waves are scattered are

reasonably well understood in a qualitative way, but more detailed analyses become quite difficult and there is still a good deal of confusion about the subject (16, 17, 18).

The description of thermal conduction is simplified if it is assumed that the excess energy is dissipated out of a normal mode in an exponential manner, using the concept of a relaxation time for that mode. Thermal conductivity can be described as

$$K = \sum_j c_j t_j (v_j)^2 \quad (3.1)$$

where the sum is over all modes j , c_j is the specific heat of mode j , t_j the relaxation time of mode j and v_j is the group velocity. Since the number of modes j is so large, the frequency spectrum can be taken as continuous without an appreciable error and the sum can be replaced by an integral. If the modes have an isotropic frequency distribution, that is, if the value of their group velocity is the same regardless of its direction, the equation for k reduces to

$$k = \frac{1}{3} \sum_i \int c_i \ell_i v_i n_i dw_i \quad (3.2)$$

where ℓ_i is the mean relaxation length defined as $t_i v_i$ and n_i as the density of modes. The subscript i refers to one

of the three polarization branches of the acoustical modes.

At low temperatures, low predominant lattice frequencies result and a point defect scatters as ω^{-4} . Also, at low temperatures, the group velocity is essentially a constant and the expression for k becomes

$$k \approx AT^3 \int_0^{\infty} \frac{x^4 e^x}{(e^x - 1)^2} \ell dx \quad (3.3)$$

If, only point defect scattering were of importance, $\ell = B\ell x^4 T^4$ where B is proportional to the average distance between defects (i.e., inversely dependent on defect concentrations). However, if this expression for ℓ is substituted into equation (3.3), the integral diverges due to the very low frequency modes not being sufficiently perturbed by the defect interactions. To circumvent this problem, Kelmens concluded that interaction processes between normal modes are very important at low temperatures, and these processes cause the following effects (17):

1. Longitudinal modes are very efficiently coupled to transverse modes of the same frequency.
2. Transverse modes with $\omega < kT/h$ are very efficiently coupled to transverse modes with $\omega \sim kT/h$ where T is the temperature, k is the Boltzmann constant and h Planck's constant.

These effects imply that when any longitudinal mode contains an excess amount of energy, it will almost immediately dump it into a transverse mode; similarly, any low-frequency transverse mode will immediately give its energy to the higher frequency modes which exist in thermal equilibrium at the given temperature. Thus, only transverse mode of frequencies above that for thermal equilibrium need be considered as far as scattering processes are concerned. Thus, equation (3.3) can be written as

$$k \approx AT^3 \left[l_{(x=1)} \int_0^1 \frac{x^4 e^x}{(e^x - 1)^2} dx + \int_1^\infty \frac{x^4 e^{x_l(x)}}{(e^x - 1)^2} dx \right] \quad (3.4)$$

where the first integral describes point defect scattering and the second integral boundary scattering. Substitution of the point defect relaxation lengths into equation (3.4) does not cause the integrals to diverge and equation (3.4) is simply the addition of resistivities if only point defect scattering and boundary scattering are important. Here, the boundary resistivity is proportional to T^{-3} and the defect resistivity to T with a resulting minimum in the resistivity curve versus temperature.

At high temperatures, essentially the same problems are encountered as in the low-temperature, defect scattering problem. For the longitudinal modes, phonon-phonon scattering which preserves momentum can take

place only with transverse waves of about the same frequency, and the probability for this happening is proportional to ω^{-4} . This scattering law leads to a divergent conductivity unless the low-energy longitudinal phonons are blocked by some auxiliary mechanism such as boundary scattering. At high temperatures, the effects of longitudinal waves cannot be neglected as in the low temperature case, and Pomeranchuk introduced 4-phonon collisions in an attempt to keep the conductivity finite. This removes the condition that longitudinal waves must interact only with transverse waves of the same frequency and avoids the divergence. Such a mechanism adds another factor of T to the temperature dependence. Therefore, for high temperature lattice thermal conductivity, k has a temperature dependence between $1/T$ and $1/T^2$.

Interestingly, the same conclusion for the behavior of thermal conductivity as a function of temperature is reached by the simple relationship

$$k \propto c v \lambda \quad (3.5)$$

for temperatures above the Debye temperature* where c is

* (the Debye temperature, θ , arising in the computation of the Debye specific heat $K\theta = h\nu$ where K is the Boltzmann's constant, h is Planck's constant, and ν is the Debye frequency (maximum allowable frequency) in the computation of the Debye specific heat. The Debye temperature reaches a maximum of 727°C for most ceramics (19))

the heat capacity, v the mean phonon speed and λ the mean free path. The heat capacity c approaches a constant with increasing temperature while the mean phonon speed remains relatively constant for all values of temperatures. Since it has been found that the mean free path λ is proportional to $1/T$, then equation (3.5) reduces to

$$k \propto \frac{1}{T} \quad (3.6)$$

Figure 3.8 illustrates experimental thermal conductivity for a number of materials indicating that this behavior is approximately followed.

Table 3.4 lists the thermal conductivity values for AS, LAS and MAS at 1200°C and the subsequent rating and figure of merit values for the three ceramic materials.

3.6 Fabricability of LAS, AS and MAS

Due to the importance and variety of fabrication processes available in industry to produce the ceramic regenerator, the fabrication details of the selected ceramic materials will be discussed separately in Chapter 5. It is sufficient to say at this point that the details of the differences between the manufacturer of AS, LAS and

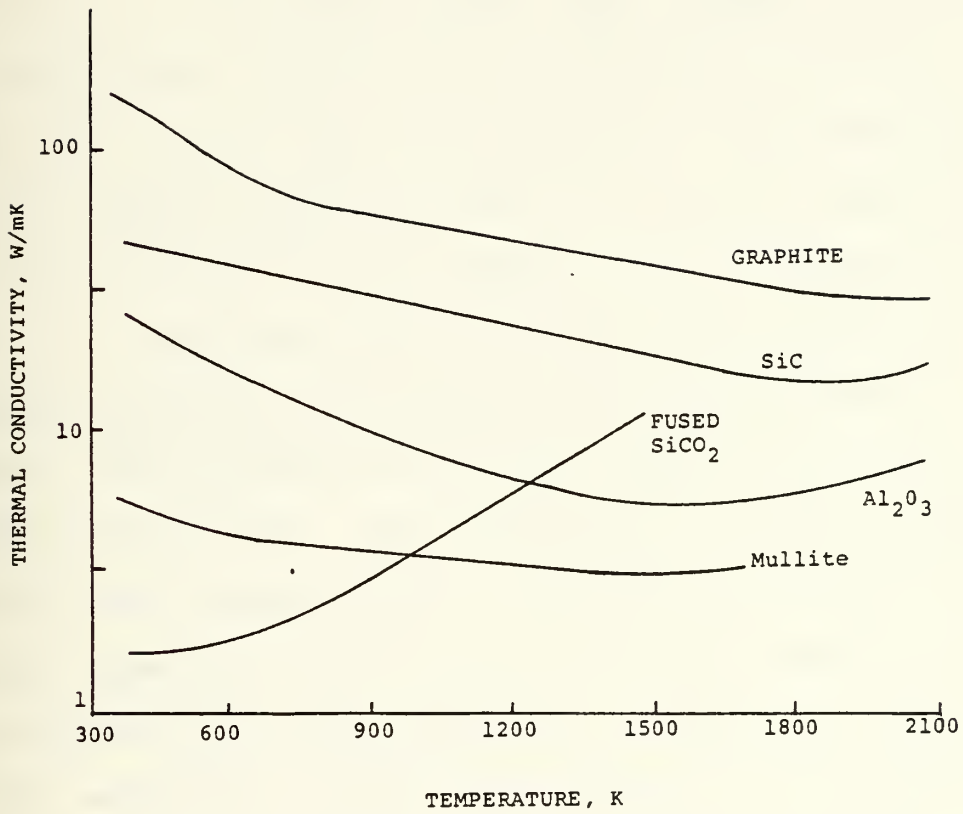


FIGURE 3.8: THERMAL CONDUCTIVITY OF VARIOUS MATERIALS

MAS regenerator matrices are minute and the scaling factors for the figure of merit scheme are equal as noted in Table 2.1.

3.7 Cost Comparison of LAS, AS and MAS

Cost comparisons between the three ceramic materials AS, LAS and MAS have been conducted by a few researchers (8, 15, 18). A 30 to 40 percent cost savings over AS can be realized if a MAS material is used for regenerator fabrication rather than an AS material. The AS material is more expensive because glass frit, the raw material of AS cost more than does raw mineral, the raw material of MAS. AS also cost more to produce than MAS due to the leaching requirement AS undergoes from an LAS based material and because the AS matrix requires refiring after the leaching process. The LAS material has essentially the same cost values as MAS. A qualitative argument can be made supporting the tendency of the MAS material to be less expensive than LAS because the primary raw material of MAS, magnesium, is much more abundant in the earth's crust than the primary raw material of LAS, lithium. See Figure 3.9.

From the discussion of this chapter and the results of Table 2.1, it becomes apparent that the ceramic material selected for the lower temperature range is magnesium aluminum silicate, MAS. The important



FIGURE 3.9: ABUNDANCE OF ELEMENTS IN THE EARTH'S CRUST

advantages that MAS has over the other two ceramic materials is strength at the working temperatures, corrosion resistance, and cost. These three advantages far out weigh MAS disadvantages in its thermal shock and thermal conductivity characteristics. It is reassuring to know that the literature frequently cited the large amount of interest researchers have in the capabilities and potential of MAS as a regenerator material.

CHAPTER 4

CERAMIC MATERIALS ANALYZED FOR OPERATION BETWEEN
1200°C-1400°C4.1 Introduction

Silicon nitride (Si_3N_4) and silicon carbide (SiC) based ceramics are being extensively studied for use as structural materials in gas turbine and adiabatic diesel engine components. Si_3N_4 is considered an ideal material for such applications due to its high strength, thermal shock resistance, chemical stability and excellent creep resistance. SiC likewise is an attractive candidate due to its ability to be fabricated into intricate shapes while still maintaining excellent high temperature strength and chemical and corrosion resistance.

However, both Si_3N_4 and SiC are fabricated and produced utilizing many different processes which in turn greatly influence the properties of the ceramic material. It became apparent from the multitude of silicon nitride and silicon carbide based ceramics, that only a handful of these ceramics had the ability to be fabricated into the intricate honeycomb regenerator matrix envisioned for the new cycle engine while still maintaining and/or providing the thermal and mechanical properties required of the regenerator.

With this perspective, only sintered and reaction bonded SiC and Si_3N_4 were analyzed. Reaction bonded Si_3N_4 and SiC (RBSN and RBSC respectively) have been developed largely to obtain a readily formable (little machining required), low cost material (22, 23). RBSN and RBSC usually maintain their strength to 1400°C but exhibit absolute strengths less than sintered Si_3N_4 and SiC. RBSN is at least 10 percent porous, resulting in oxidation properties being less desirable than sintered Si_3N_4 and SiC.

Sintered Si_3N_4 and SiC are rather recent developments (24, 25, 26, 27, 28, 29, 30, 31, 32, 33, 34). Their interest of late is due to the success in producing sintered Si_3N_4 and SiC of at least 95 percent of the theoretical density. This increase in density results in a decrease in porosity and subsequent improved strength and oxidation resistance at normal operating engine temperatures.

Due to the much better strength and oxidation properties of sintered SiC and Si_3N_4 compared to reaction bonded SiC and Si_3N_4 , only sintered SiC and Si_3N_4 will be analyzed as possible ceramic materials for the operating temperature range of $1200^\circ\text{--}1400^\circ\text{C}$.

4.2 Sintering Process

It is convenient at this point to present some background knowledge of sintering. Sintering is

essentially a removal of the pores between the starting particles (accompanied by shrinkage of the component), combined with growth together and strong bonding between adjacent particles. The following criteria must be met before sintering can occur:

1. A mechanism for material transport must be present.
2. A source of energy to activate and sustain this material transport must be present.

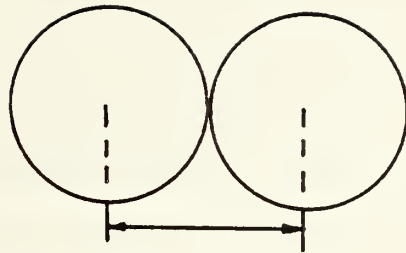
The primary mechanisms for transport are diffusion and viscous flow. Heat is the primary source of energy, in conjunction with energy gradients due to particle-particle contact and surface tension. Sintering can occur by a variety of mechanisms, as summarized in Table 4.1. SiC and Si_3N_4 involve solid-state sintering requiring material transport by diffusion. Diffusion consists of movement of atoms or vacancies along a surface or given boundary or through the volume of the material. Surface diffusion, like vapor-phase transport does not result in shrinkage. Volume diffusion, whether along grain boundaries or through lattice dislocation, does result in shrinkage, as illustrated in Figure 4.1.

Much of the early work on sintering demonstrated that for a constant sintering time, the density of the piece increases as the sintering temperature is raised. The terms sintering temperature or recrystallization temperature or maturing temperature refer to the temperatures at

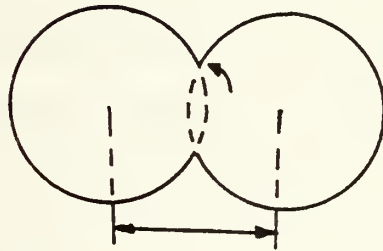
TYPE OF SINTERING	MATERIAL TRANSPORT MECHANISM	DRIVING ENERGY
Vapor Phase	Evaporation - Condensation	Differences in vapor pressure
Solid State	Diffusion	Differences in free energy or chemical potential
Liquid Phase	Viscous flow, diffusion	Capillary pressure, surface tension
Reactive Liquid	Viscous flow, solution - precipitation	Capillary pressure, surface tension

5 6

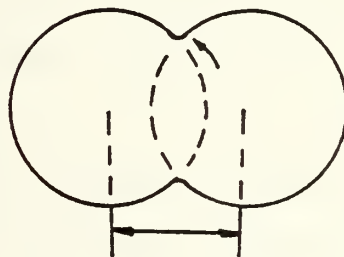
TABLE 4.1: SINTERING MECHANISMS



ADJACENT PARTICLES
IN CONTACT



NECK FORMATION
BY DIFFUSION



DISTANCE BETWEEN
PARTICLE CENTERS
DECREASED, PARTICLES
BONDED, PORE SIZE
DECREASED

FIGURE 4.1: SCHEMATIC OF SOLID-STATE MATERIAL
TRANSPORT

which shrinkage proceeds to the desired extent in the heating time selected. In general, the solid-state reactions proceed continuously at all temperatures and the only effect of increasing the temperature is to increase the rate.

Figure 4.2 taken from reference (3) shows the typical behavior of a powder compact upon heating. At any temperature, the initial shrinkage rate of the compact is high, and it decreases with time. At long times, the density appears to approach a limiting value. As the temperature is increased, the shrinkage rate increases and the ultimate density appears to increase. It is now constructive to plot the data on a logarithmic rather than an arithmetic scale. This is done in Figure 4.3. It is apparent from the examination of Figures 4.2 and 4.3, that the control of the temperature and the particle size are extremely important, but that the control of time is less important.

In the early stages of sintering, the plot of $\text{Log } (\Delta L/L_0)$ or its equivalent versus $\text{Log } (\text{time})$ is nearly a straight line. Thus the sintering law can be expressed empirically by the relationship

$$\Delta L/L_0 = kt^n \quad (4.1)$$

where k is a temperature-dependent proportionality constant, t is time, and the exponent n has a value

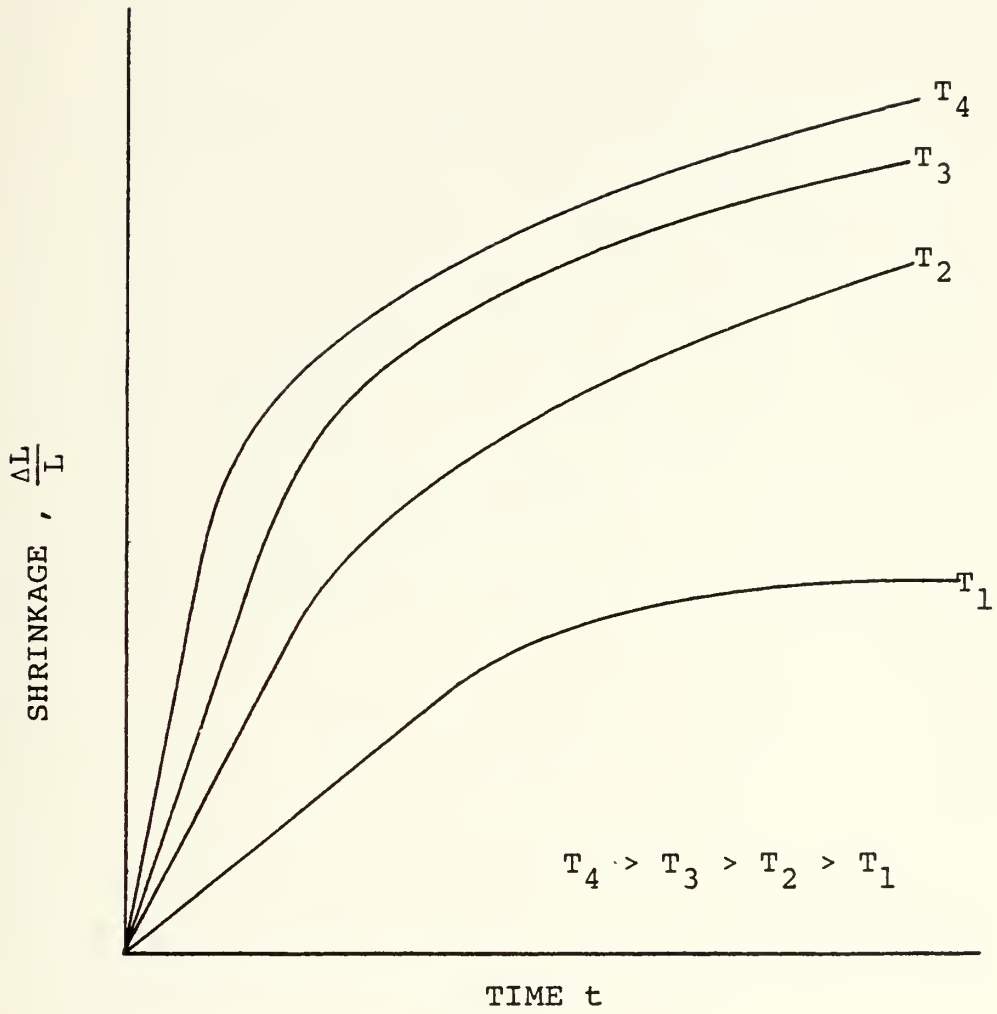


FIGURE 4.2: SINTERING RATE AS A FUNCTION OF TEMPERATURE AND TIME

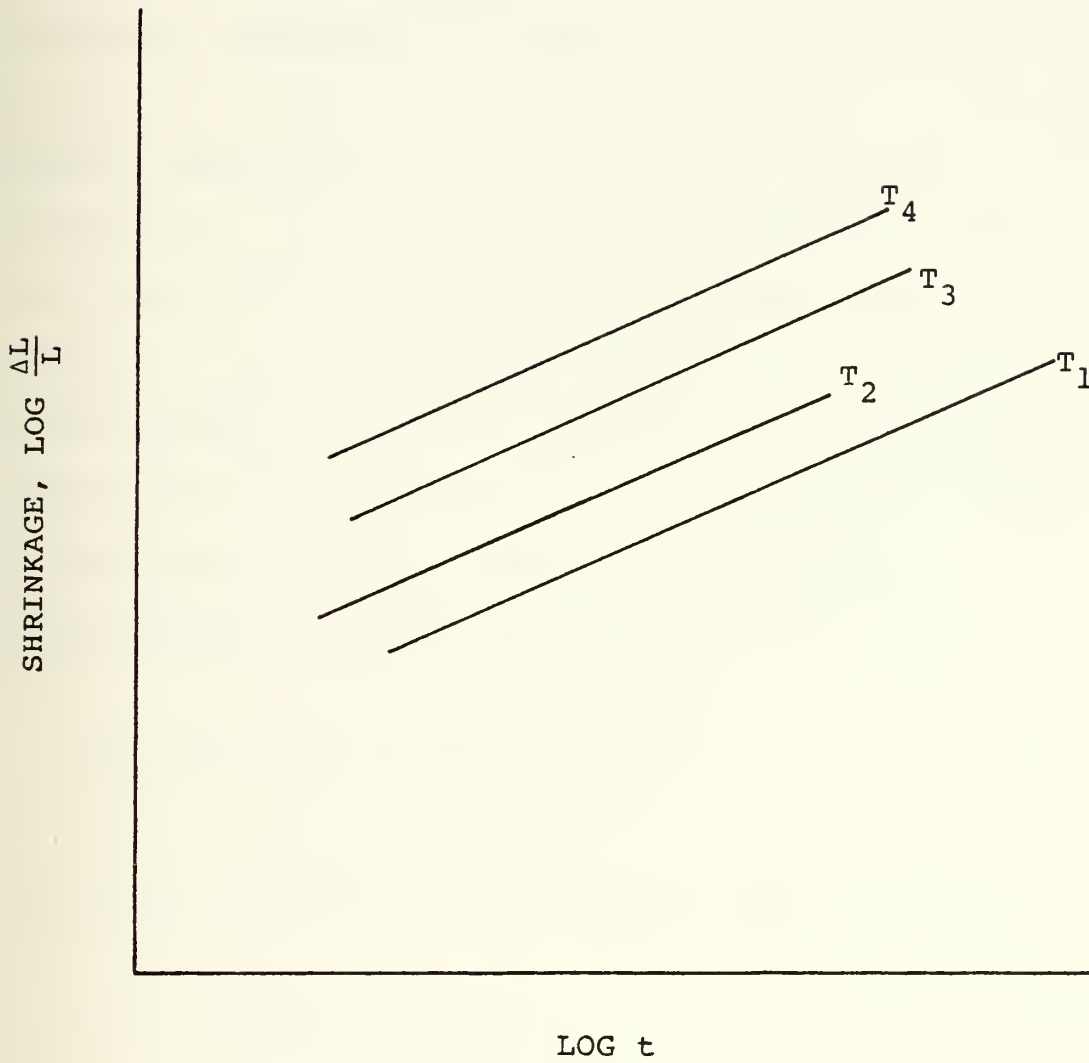


FIGURE 4.3: SINTERING RATE AS A FUNCTION OF LOGARITHMIC TEMPERATURE AND TIME

ranging between 0.4 and 0.5. Obviously, this equation does not apply at Log (time) because shrinkage will stop when the theoretical density is reached, if not before.

The sintering process will be described utilizing the development presented in reference (53). It is convenient to think in terms of the sintering together of two single crystal spheres as shown in Figure 4.4. In this illustration, r is the radius of the individual spheres, x the radius of the circular area of contact between the spheres, y is the difference between r and half the distance between the sphere centers, and ρ the radius of curvature of the lenticular contact between the spheres. By assuming, $y = x^2/2r$, the area of the cylindrical surface between the spheres is about

$$A = (2y)(2\pi x) = 2\pi x^3/r \quad (4.2)$$

The radius of curvature of the cylindrical surface is

$$\rho = 6 = x^2/2r \quad (4.3)$$

and the volume of the cylindrical lens is

$$V = \pi x^2 y = \pi x^4/2r \quad (4.4)$$

The model of the process assumed will be that vacancies diffuse from under the surface of curvature ρ to

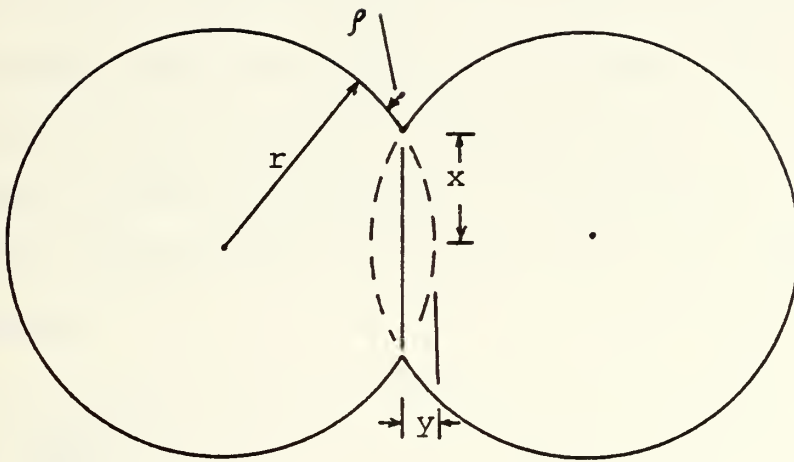


FIGURE 4.4: MODEL FOR SINTERING PROCESS

the grain boundary between the spheres to produce a shrinkage so that the centers of the spheres move together. The rate of matter transport is

$$\frac{dV}{dt} = A \frac{\Delta c}{\rho} D' \quad (4.5)$$

where Δc is the concentration for vacancies between the grain boundary and the lenticular surface. The assumption that the diffusion distance is about equal to ρ is made. D' is the diffusion coefficient for vacancies.

Δc is computed from the Kelvin equation by the relationship

$$\Delta c = \frac{2\gamma a^3}{KT\rho} C \quad (4.6)$$

where C is the equilibrium concentration of vacancies in the lattice given by

$$C = e^{-Q/RT} \quad (4.7)$$

$$D = D' e^{-Q/RT} \quad (4.8)$$

where D is the self-diffusion coefficient of atoms. Substituting equations (4.6), (4.7), and (4.8) into equation (4.5) yields

$$\frac{d\left(\frac{\pi x^4}{2r}\right)}{dt} = \frac{\pi x^3}{r} \frac{2\gamma a^3}{KT} \left(\frac{2r}{x^2}\right)^2 D \quad (4.9)$$

Simplifying and integrating equation (4.9) leads to

$$\frac{x^5}{r^2} = \left[\frac{4\gamma a^3 D}{KT} \right] = kt \quad (4.10)$$

since $x = 0$ at $t = 0$.

The fractional shrinkage is

$$\frac{\Delta L}{L_0} = \frac{Y}{r} = \frac{x^2}{2r^2} \quad (4.11)$$

Substituting equation (4.10) into equation (4.11)

leads to

$$\frac{\Delta L}{L_0} = \left[\frac{k^{2/5}}{2} \right] \left(\frac{1}{r^3} \right)^{2/5} t^{2/5} \quad (4.12)$$

which shows that the fractional shrinkage is proportional to the $2/5$ power of time.

A similar relationship to equation (4.12) was derived by Kingery (16) where

$$\frac{\Delta L}{L_0} = \left[\frac{20\gamma a^3 D^{*2/5}}{2 KT} \right] r^{-6/5} t^{2/5} \quad (4.13)$$

where $\frac{\Delta L}{L_0}$ is the fractional shrinkage, γ the surface energy, a^3 the atomic volume of diffusing vacancy, D^* the

self diffusion coefficient, k the Boltzmann's constant, T the temperature, r the particle radius and t is the time.

Extending this model of two spheres in contact to the situation when a number of spheres or particles are packed together to make an aggregate for sintering will be done. When a number of particles are packed together, voids will be left where fitting is imperfect. These voids are, of course, the pores, and they are the counterpart of the lenticular contacts of radius ρ . All these pores are initially joined by grain boundaries, just as the lenticular areas are joined by a grain boundary in Figure 4.4. Thus, equation (4.12), for the shrinkage, or the rate of approach of the two spheres, should apply equally well to the shrinkage of a powder compact. This is indeed the case as can be seen by comparing equation (4.12) and equation (4.1), which was empirically developed.

It must be emphasized that the shrinkage law presented in equation (4.1) will hold only if all pores are connected by grain boundaries. This situation will always occur during the early stages of sintering, because the pores are formed by the lack of fit of separate particles. However, in the latter stages of sintering, some grain growth may occur, as a result, the diffusion distance for vacancies, the distance pores must diffuse to a grain boundary, becomes much greater so the rate of sintering decreases.

Since pores far removed from boundaries can disappear only with difficulty, it is important that the phenomenon of grain growth, and the factors that control the mobility and position of grain boundaries in a polycrystalline, porous material be understood.

From a large variety of observations it has been well established that the driving force for grain growth is the surface tension of the grain boundaries. Grains have various number of sides, and because of this, it is necessary that most of the grain boundaries be curved. Grains having six sides can have straight boundaries and meet the requirement that all boundaries meet at 120° . Grains having fewer than six sides will have boundaries which are concave when observed outward from the center of the grain. Most of the boundaries of grains having more than six sides will be convex when observed outward from the center of the grain, as illustrated in Figure 4.5. In their attempt to decrease their total area, boundaries will move toward their centers of curvature. Thus, grains having more than six sides will grow smaller.

Researchers have determined that the rate at which a boundary will move is inversely proportional to the radius of curvature of the boundary. Therefore, on the average, the rate at which a grain will grow will be inversely proportional to its diameter, or, the rate at which grain

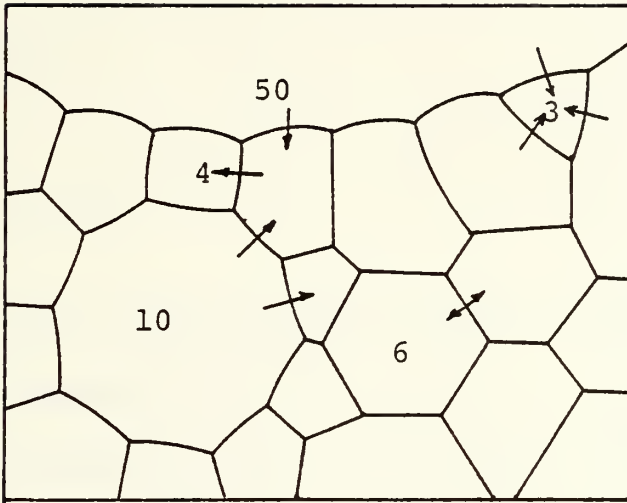


FIGURE 4.5: SCHEMATIC DRAWING OF
POLYCRYSTALLINE SPECIMEN
(ARROWS INDICATE DIRECTIONS
IN WHICH BOUNDARIES WILL
MIGRATE)

growth will occur in a polycrystalline aggregate will be inversely proportional to the average diameter of the grains that are present.

In other words, the growth law is

$$\frac{dD}{dt} = 1/D \quad (4.14)$$

or integrating,

$$D - D_0 = kt^{1/2} \quad (4.15)$$

where D is the instantaneous diameter of the grains, and D_0 is the diameter at $t = 0$.

Grain growth will then continue in principle until the piece becomes a single crystal. This, of course, is not observed. There exist a limiting grain size which a number of investigators have demonstrated to be a result of second phase inclusions.

The reason for this is that a grain boundary has difficulty migrating past an inclusion, because an area of boundary equal to the cross-sectional area of the inclusion must be formed in the boundary on the far side of the inclusion. The surface energy of this area of boundary must be provided by a decrease in the area for the rest of the boundary, thus the inclusion impedes boundary movement.

The ultimate grain size will be controlled by the total impeding effect of all the inclusions in the piece. Thus, the final grain size D_f will be smaller the greater the volume fraction of inclusions. It will also be smaller the greater the number of inclusions, so a given volume fraction of inclusions will be least effective when the inclusions are large. Ultimate grain size will be given roughly by the equation

$$D_f = d/f \quad (4.16)$$

where D_f is the limiting grain size, d is the average inclusion diameter, and f is the volume fraction of inclusions in the specimen.

As mentioned previously and from equations (4.12) and (4.13), finer-particle size powder can be sintered more rapidly and at a lower temperature than coarser powder. Not apparent in the equation, but highly important to the final properties, are the uniformity of particle packing, the particle shape, and the particle size distribution. If particle packing is not uniform in the greenware (unfired ceramic piece), it will be very difficult to eliminate all the porosity during sintering.

Particle shape is also important. Too high a concentration of elongated or flattened particles can result in bridging during forming, producing a large or

irregularly shaped pore that is difficult to remove during sintering. Particle size distribution is also critical. Particles that are all of one size do not pack efficiently, they form compacts with large pores and a high volume percentage of porosity.

4.3 Sintered SiC

Returning now to the two ceramic materials being analyzed, SiC has two crystallographic forms, β -SiC the low temperature form, which is stable to roughly 2000°C having a cubic structure, and the high temperature form α -SiC consisting of a number of hexagonal polytypes.

Until recently, fully dense SiC could be fabricated only by hot pressing using densification aids such as boron, B and aluminum, Al. Pressureless sintering of SiC was first reported by Prochazka in 1973. In this work, high purity β -SiC with a high surface area was sintered to greater than 95 percent theoretical density at 1950°-2100°C. Simultaneous additions of 0.3 percent B and 0.5 percent carbon, C proved most effective in promoting sintering. Microstructurally, a problem developed resulting from sintering at temperatures near the β to α (phase) transition. During sintering, if α -SiC grains were nucleated, or if seed α -SiC grains were in the raw materials, these grains would undergo exaggerated grain growth of α -SiC up to 100 μm in length as compared to the

average grain size of 10 μm (35, 36). To minimize the phase change and grain growth, careful control of the entire processing sequence including raw material phase purity, levels of B and C, sintering temperature and atmosphere became essential.

A more economical procedure was developed by Coppola and McMurty. They successfully sintered α -SiC, again employing simultaneous additions of B and C. The distinct advantage of sintering α -SiC is that this material avoids the phase change problems of sintered α -SiC since it is already in the α -SiC form. Due to the inherent cost advantages of the α -SiC sintering process and its subsequent greater strength characteristics compared to β -SiC, α -SiC will be the material selected for comparison to sintered Si_3N_4 .

Extending the figure of merit scheme introduced in Chapter 2 to sintered Si_3N_4 and SiC, Table 4.2 was developed from the results of the elimination process detailed thus far in this chapter, together with the conclusions to be made in the subsequent sections of this chapter.

4.4 Strength Comparison of Sintered Si_3N_4 and SiC

The strength comparison between sintered Si_3N_4 and SiC is clearly illustrated in Figure 4.6. Figure 4.6

<u>PARAMETER</u>	<u>WEIGHTING FACTOR</u>	<u>CERAMIC MATERIAL</u>			
		<u>SiC</u>		<u>Si₃N₄</u>	
		<u>RATING</u>	<u>VALUE</u>	<u>RATING</u>	<u>VALUE</u>
Strength	10	2	20	1	10
Corrosion Resistance	10	2	20	1	10
Thermal Shock	7	1	7	2	14
Thermal Conductivity	7	1	7	2	14
Fabricability	10	1.5	15	1.5	15
Cost	10	1.5	<u>15</u>	1.5	<u>15</u>
			84		78

TABLE 4.2: FIGURE OF MERIT FOR CERAMIC MATERIALS
ANALYZED FOR THE HIGHER TEMPERATURE
RANGE

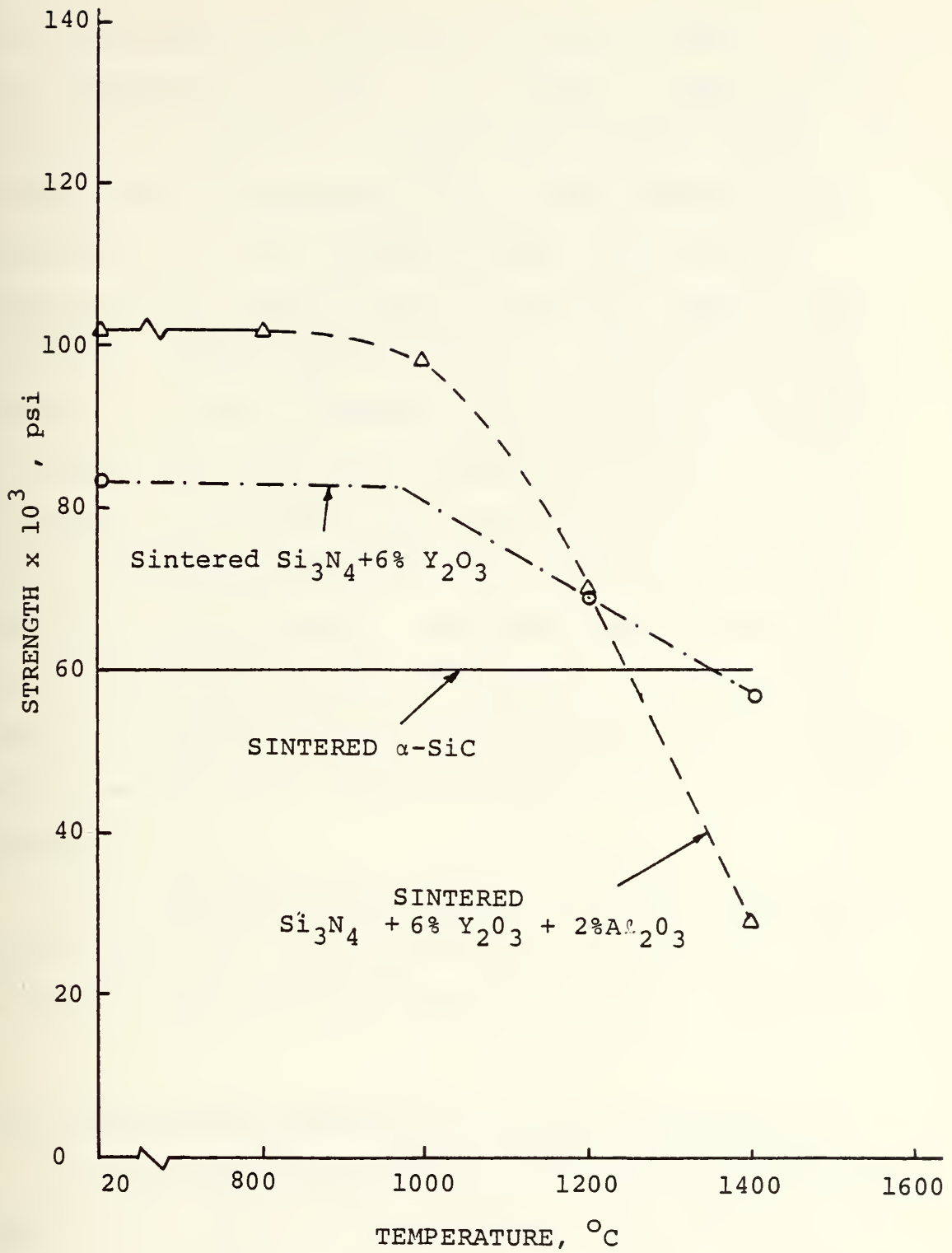


FIGURE 4.6: ELEVATED TEMPERATURE STRENGTH OF SiC AND Si_3N_4

illustrates that α -SiC strength increases slightly from room temperature to 1380°C. In contrast, a sharp loss in strength was observed in sintered Si_3N_4 above 1000°C. The strength loss in sintered Si_3N_4 at high temperature is attributed to a grain boundary glassy phase which is retained during cooling from the sintering temperature. This grain boundary phase softened at high temperature, leading to a loss in strength. The fracture mode of SiC is transgranular from room temperature to 1500°C (34). The strength of sintered Si_3N_4 and SiC is not significantly affected by exposure to hot combustion gases at 1100°C for up to 25 hours. The tests were conducted at three atmospheres pressure, 152 meters/second velocity using No.2 diesel oil with a sulfur content of 0.35 weight percent (maximum) and carbon residue of 0.2 weight percent (maximum) (37).

On the basis of Figure 4.6 and the data researched to produce Table 4.6, the ratings of Si_3N_4 and SiC for the material strength characteristic are listed in Table 4.2.

4.5 Corrosion and Oxidation of Sintered Si_3N_4 and SiC

Corrosion and oxidation resistance data for sintered Si_3N_4 and SiC are numerous and fairly well understood (28, 37, 38, 39, 40, 41, 42). Cyclic oxidation tests consisting of one hour of testing at 1380°C in air followed by cooling to room temperature for 20 minutes for a 90 hour

period indicated that the oxidation resistance of sintered α -SiC is better than sintered Si_3N_4 (24). Figure 4.7 clearly illustrates the far superior oxidation resistance of sintered α -SiC compared to two different manufacturer's sintered Si_3N_4 . Figure 4.8 shows the average weight change for Si_3N_4 and SiC as a function of corrosion time at 1100°C , 3 atmospheres pressure. Both specimens lost weight with time linearly with Si_3N_4 losing more weight than SiC (37, 39). The Si_3N_4 specimens lost weight with time almost linearly and this weight loss can be expressed in terms of an average surface erosion, R , by the following expression

$$R(\text{Si}_3\text{N}_4) = 0.33 - 0.0134 t \quad (4.17)$$

where R is in microns, and t is the exposure time in hours. The average surface erosion for silicon carbide is represented by

$$R(\text{SiC}) = 0.022 - 0.0292 t \quad (4.18)$$

where R is the average surface erosion in microns, and t is the exposure time at 1100°C in hours.

Additional testing of Si_3N_4 and SiC subjected to hot combustion gases for 250 hours, 1100°C , 3 atmospheres with

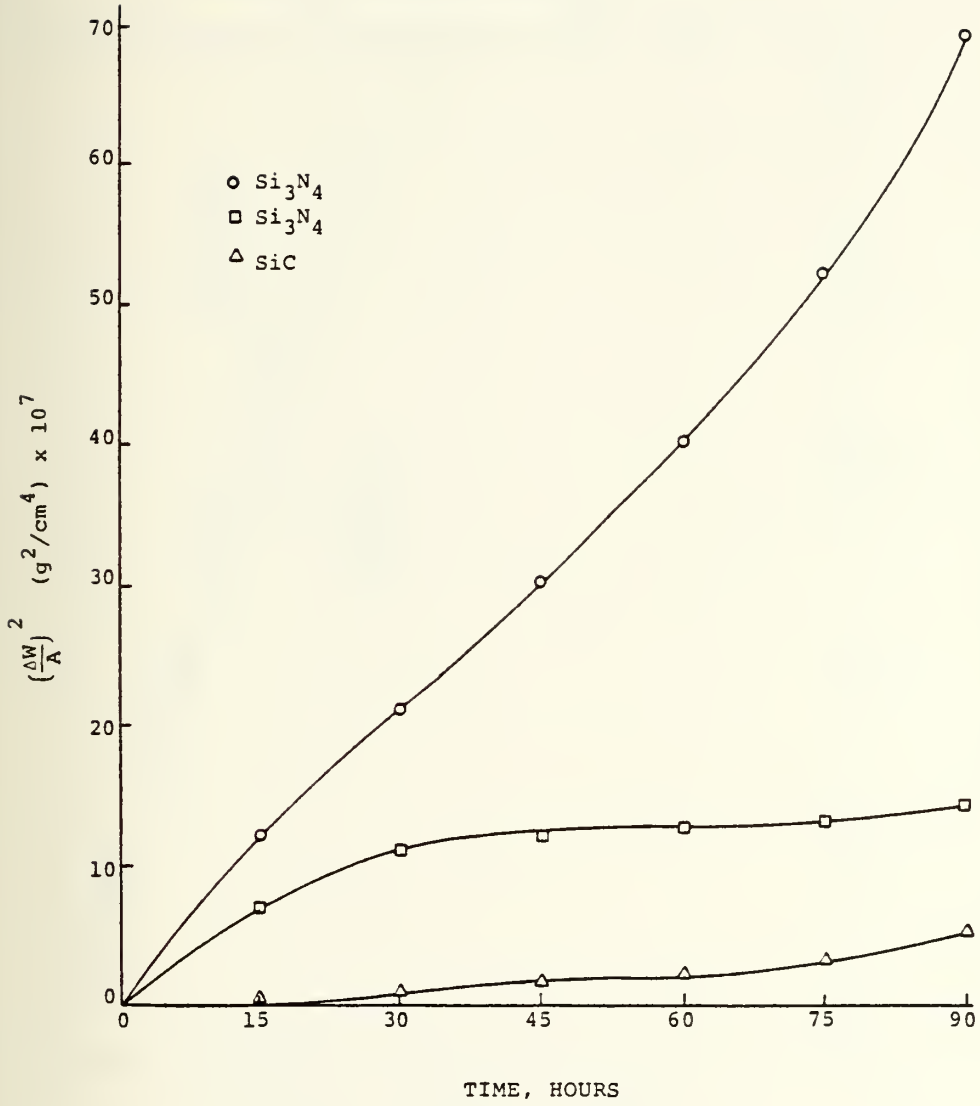


FIGURE 4.7: WEIGHT GAIN IN AIR AT 1380°C OF SINTERED Si_3N_4 AND SiC

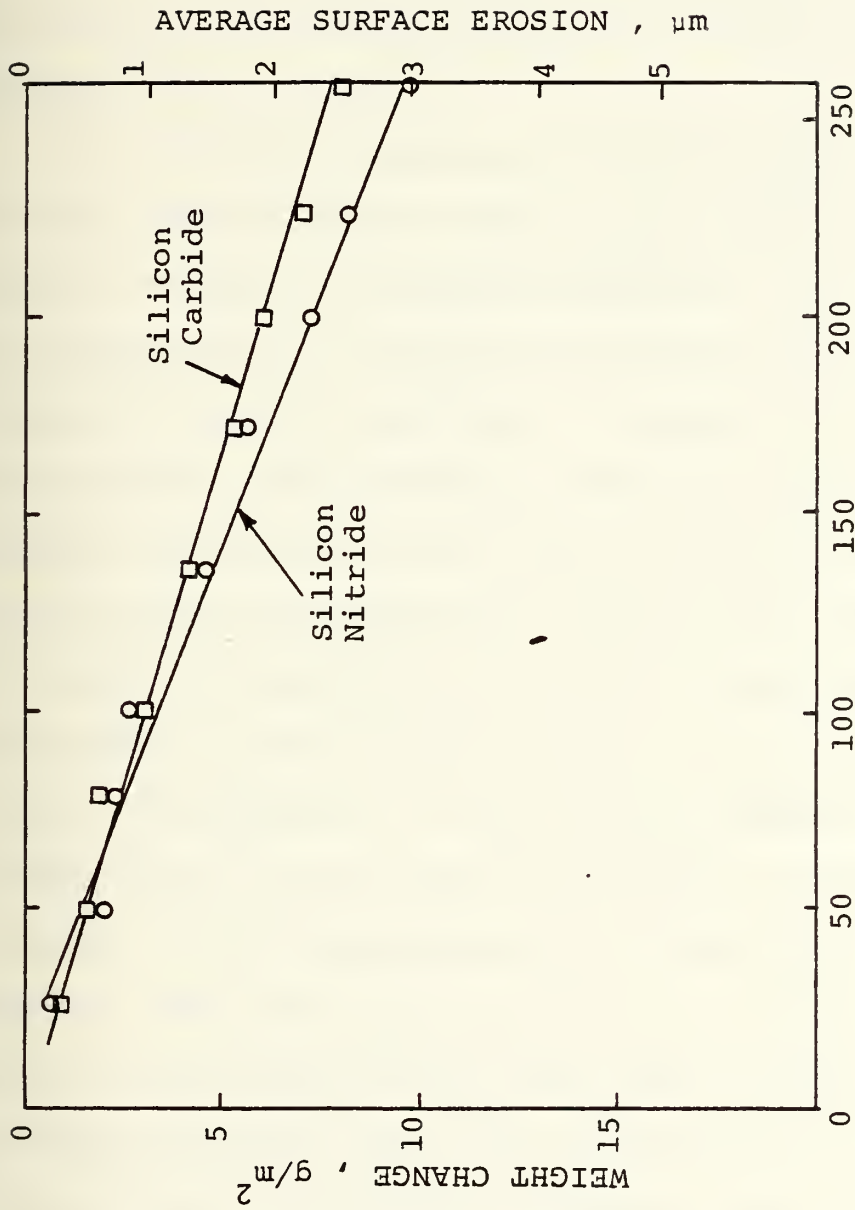


FIGURE 4.8: CORROSION-EROSION BEHAVIOR OF SILICON CARBIDE AND SILICON NITRIDE

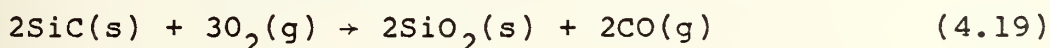
5 ppm sodium, 2 ppm vanadium, 0.6 ppm magnesium, and 0.5 weight percent sulfur added to No. 2 diesel fuel produced results indicating that the magnitude of corrosion attack using this fuel is about equal to clean fuel corrosion attack data. No compounds of sodium, vanadium, or sulfur were found in the surface deposits of the Si_3N_4 and SiC samples (37).

The effects of vanadium contamination on Si_3N_4 and SiC were analyzed under normal engine conditions. Vanadium oxidizes to vanadium pentoxide (V_2O_5) and enters the regenerator in a gaseous or condensed form from the combustion cylinder depending on temperature or concentration. The literature indicates that with 100 ppm vanadium contamination, all V_2O_5 is found to be in the gaseous state for temperatures above 700°C (38). To test this result, experiments using No. 2 diesel fuel with 100 ppm vanadium, and 0.5 weight percent sulfur added at 1100°C , 3 atmospheres to Si_3N_4 and SiC samples were conducted (37). The results indicated no compounds of vanadium or sulfur were detected in the Si_3N_4 or SiC samples. Additional testing of high velocity exhaust gases on the surface oxide layer which eroded away as it is formed indicated that this simultaneous corrosion-erosion attack at 1100°C is extremely small. The average surface erosion after 250 hours of exposure at 1100° is only 2.3 μm for SiC and 3 μm for Si_3N_4 .

The apparent oxidation resistance advantage of SiC to Si_3N_4 accounts for the figure of merit ratings given to SiC and Si_3N_4 in Table 4.2. It should be noted that from the references cited, the corrosion resistance behavior of Si_3N_4 and SiC are quite similar with SiC having slightly better performance characteristics under normal engine operating conditions.

The normal excellent oxidation resistance of SiC depends on the formation of a thin, self-healing, passive SiO_2 scale on all exposed surfaces. Many investigators have been concerned with various aspects of this passivation phenomenon, e.g., the kinetics and mechanism of oxidation and the microstructure of the SiO_2 layer. Under certain conditions, however these materials can show other modes of behavior; e.g., accelerated corrosion in the presence of basic oxides or active oxidation or loss by SiO gasification when exposed to low ambient partial pressures of oxygen. Figure 4.9 summarizes schematically the different types of behavior that maybe exhibited by SiC in a variety of gas-salt environments at temperatures near 1200°C .

At high oxygen partial pressures, passive oxidation of SiC proceeds by either or both of the following reactions:



BEHAVIOR OF SiC IN GAS-MOLTEN SALT ENVIRONMENTS

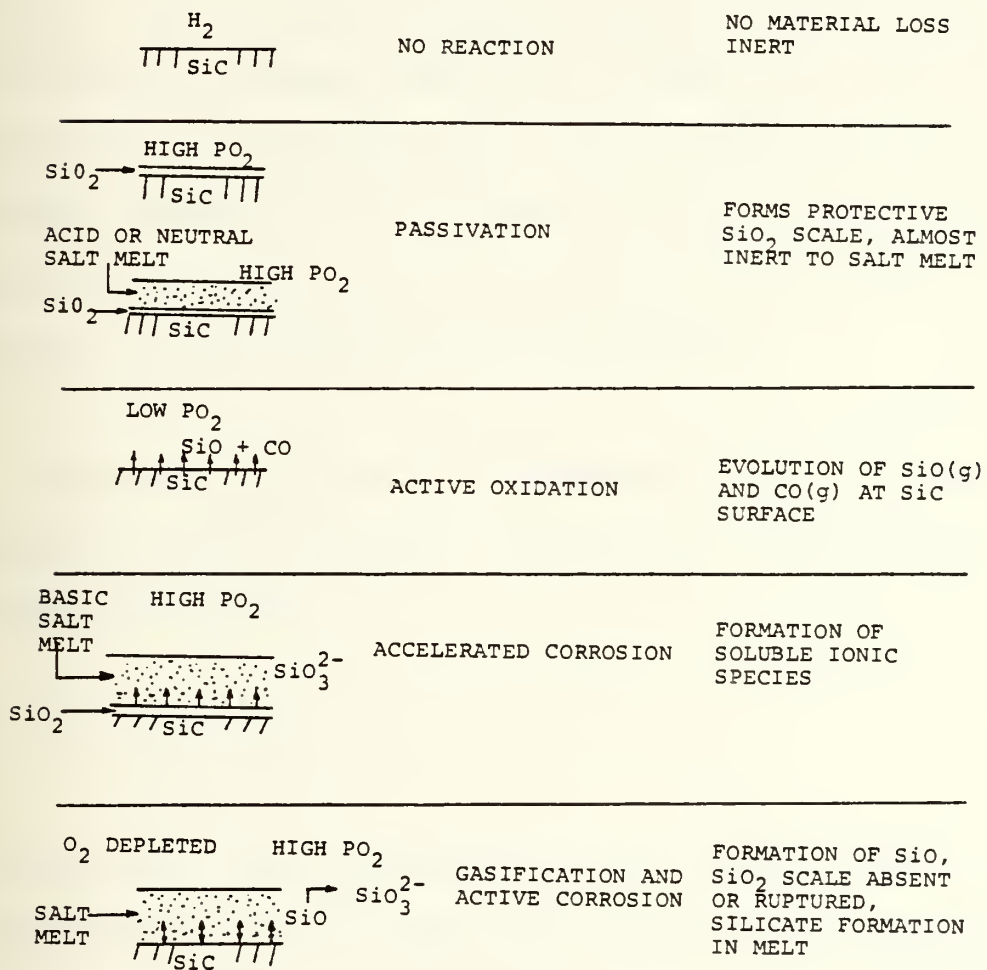
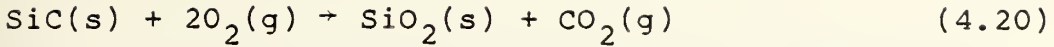


FIGURE 4.9: POSSIBLE MODES OF BEHAVIOR OF SiC IN GAS-MOLTEN-GAS ENVIRONMENTS



The formation of the SiO_2 layer on the SiC surface is accompanied by the evolution of gaseous CO or CO_2 which may cause pores to develop in the growing silica scale. Oxygen diffuses through this silica oxide scale to the SiC surface. But, as the protective coating of SiO_2 thickens, the oxidation process slows down. Therefore, the stability of this oxide layer and its effect on the further oxidation of the silicon carbide surface become important considerations in the application of SiC ceramics to high temperature environments.

The model used for the oxidation of SiC is that proposed by Deal and Grove. This model leads to the governing equation

$$x^2 + Ax = B(t + \tau) \quad (4.21)$$

in which the oxide thickness, x , is a function of oxidation time, with temperature incorporated into the constants A , B , and τ . In the limit of long oxidation times, which result in thick oxide layers, equation (4.21) yields the parabolic law of oxidation growth

$$x^2 = Bt \quad (4.22)$$

and since B is proportional to the diffusion coefficient of O_2 through SiO_2 , the parabolic growth region is governed by the diffusion of O_2 through the oxide (28, 33, 34, 39).

Solving equation (2.21) for x yields

$$x = \left(\frac{A}{2}\right) \left(1 + [(t-\tau)/(A^2/4B)]^{1/2} - \left(\frac{A}{2}\right) \quad (4.23)$$

For small values of t , equation (4.23) can be approximated by

$$x \approx \left(\frac{B}{A}\right)^{1/2} (t + \tau) \quad (4.24)$$

where B/A is proportional to the chemical-surface reaction rate constant. A relationship of this type indicates that the oxidation products formed during heating offer no resistance to the diffusion of the oxidizing gas toward the SiC surface. This is probably attributed to a porous oxide layer for small values of time. Figure 4.10 illustrates that for oxide thicknesses of greater than 2500 \AA , the oxidation rate curves have a slope of $1/2$ while below 2500 \AA , the curves increase in slope, tending to approach the predicted linear oxidation (41).

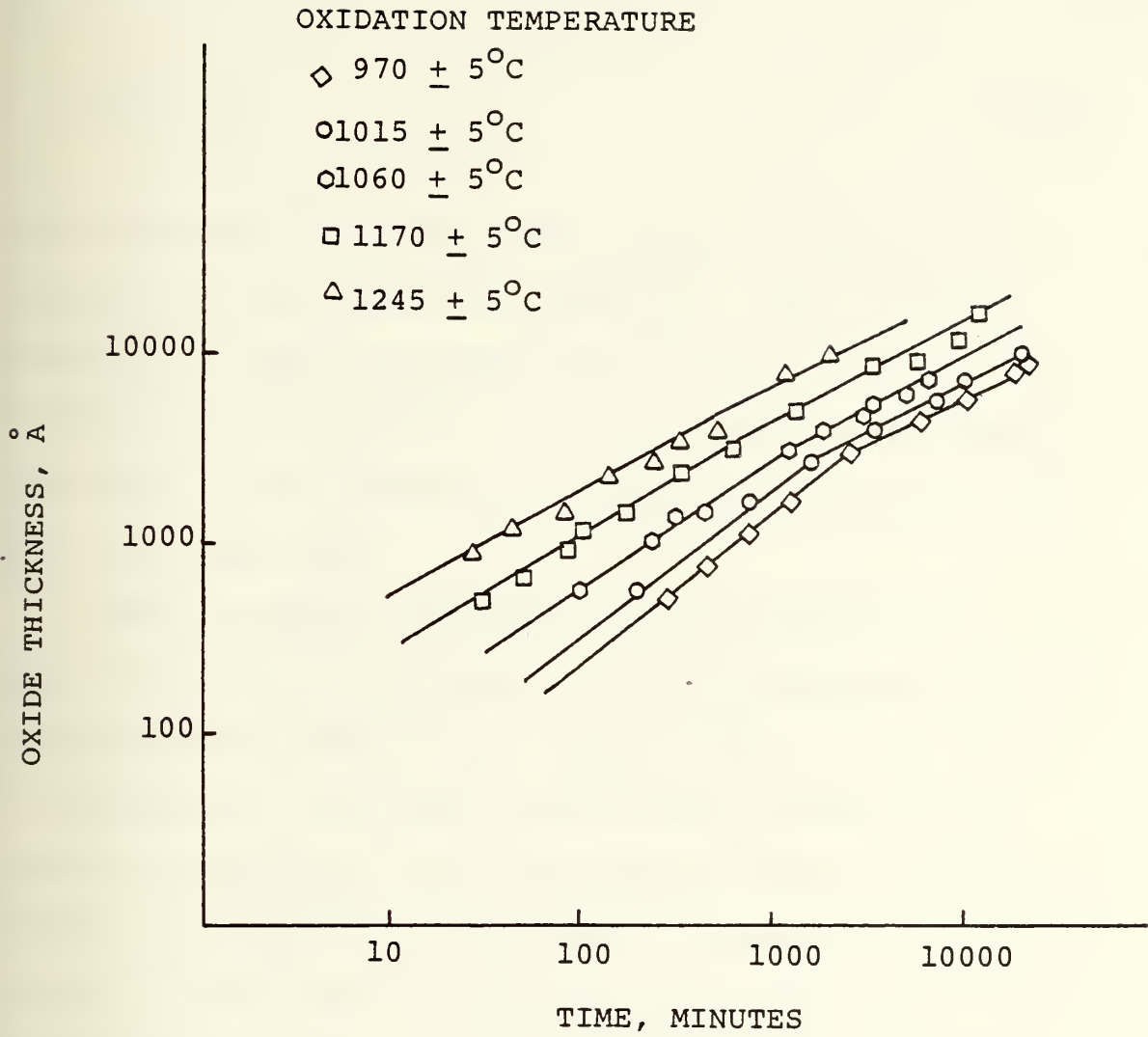


FIGURE 4.10: OXIDE THICKNESS VERSUS OXIDATION TIME

On a weight gained basis, the oxidation of SiC in air also exhibits a parabolic behavior. Classical parabolic behavior for oxidation can be represented by the following equation

$$W^2 = k_p t \quad (4.25)$$

where W is the weight gain after time, t , and k_p is the parabolic rate constant for oxidation. From a plot of weight gain versus the square root of time, Figure 4.11 illustrates that parabolic oxidation behavior is observed. Note that as the oxidizing air temperature increases, so does the weight gain.

Similar results were obtained for corresponding higher oxidation temperatures in an O_2 atmosphere in a gas stream velocity of 0.6 m/sec (Figure 4.12). With a rise in temperature, the kinetic relationship changes from linear to quadratic. At temperatures between 1647° and 1697°C , a parabolic oxidation law is observed, which is typical for the case of formation of a continuous, non-porous oxide film firmly adhering to the starting substance and having a molecular volume greater than that of the starting substance. Parabolic rate constants for the oxidation of SiC in static air are listed in Table 4.3. Similar tendencies and observations are made from

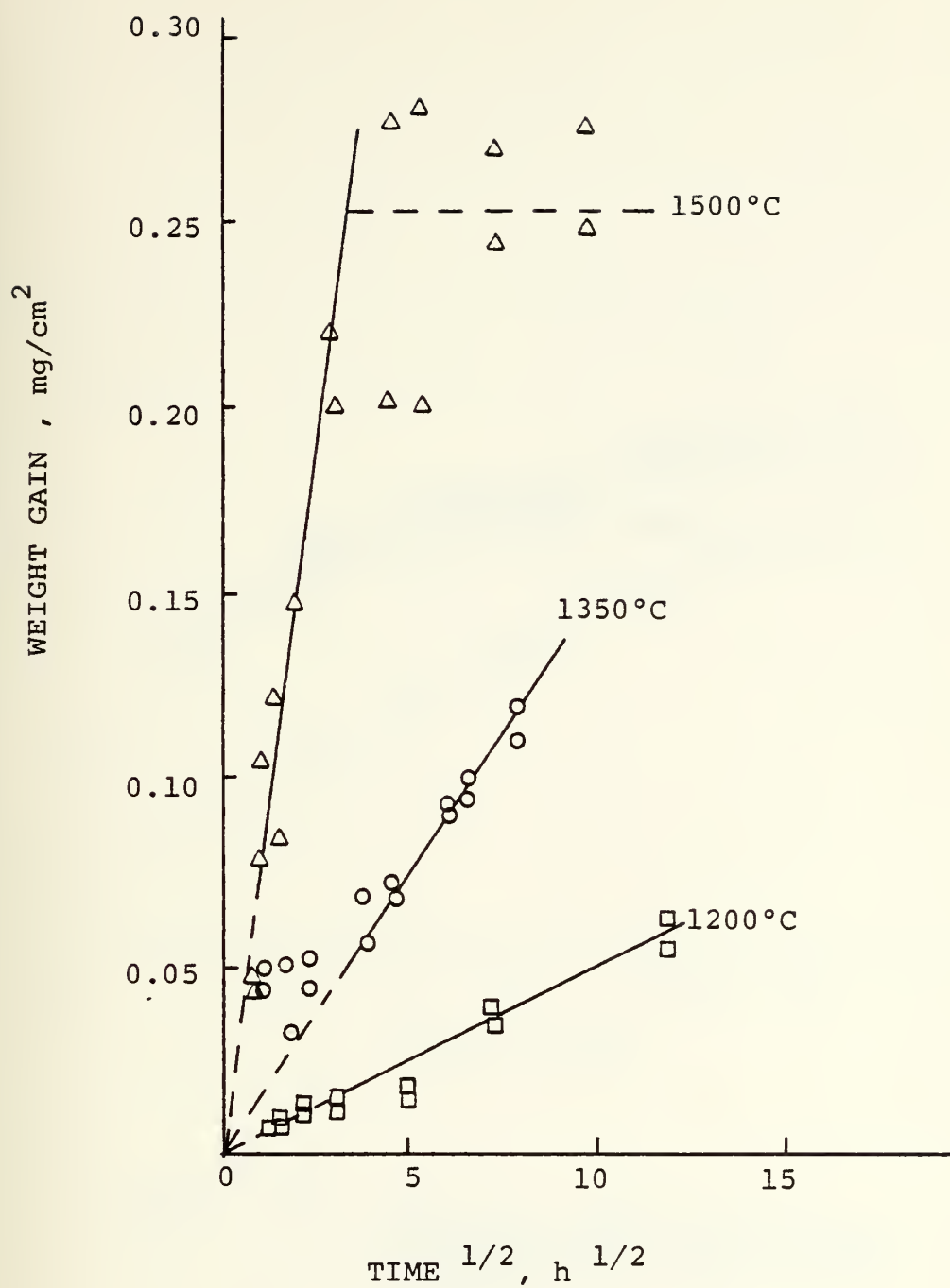


FIGURE 4.11: OXIDATION WEIGHT GAIN
VERSUS TIME 1/2 FOR
SINTERED ALPHA SiC

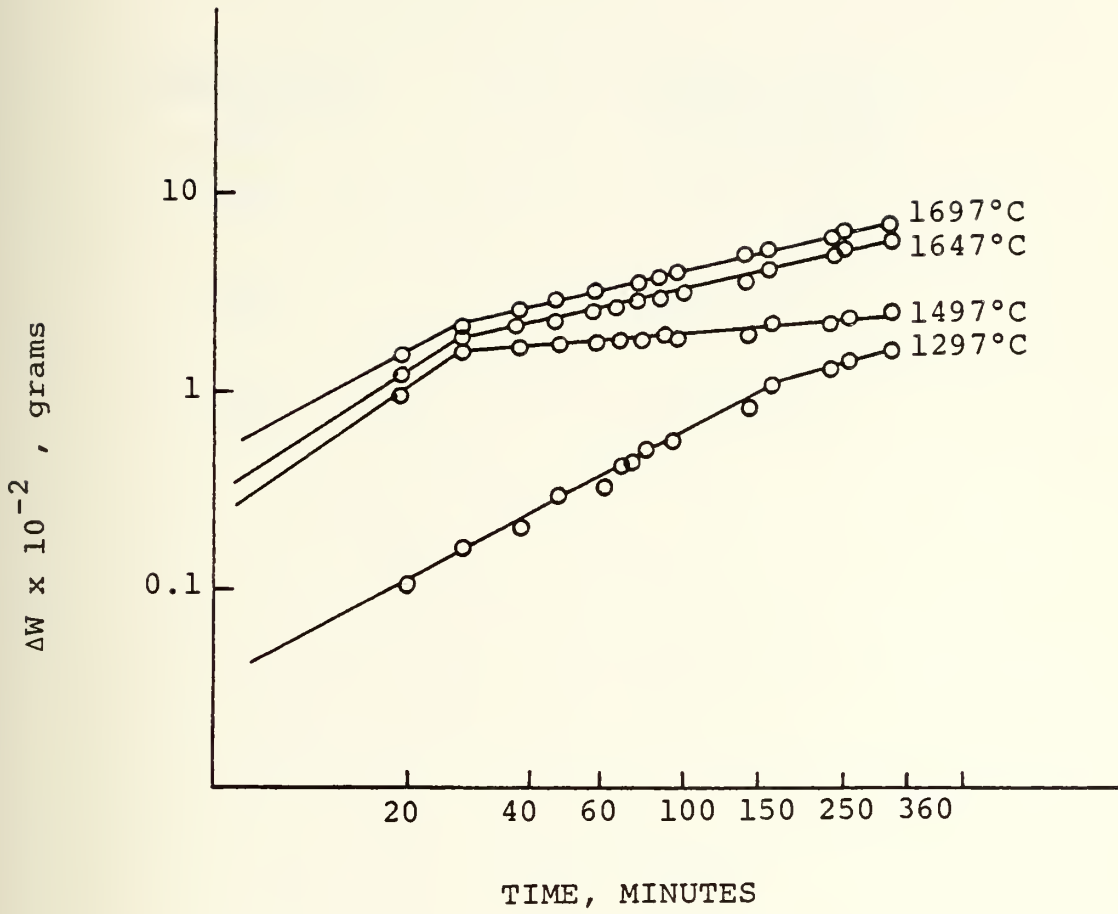


FIGURE 4.12: OXIDATION ISOTHERMS FOR POLYCRYSTALLINE SiC IN OXYGEN AT TEMPERATURES FROM 1297°C TO 1697°C

TEMPERATURE (°C)	RATE CONSTANT (g ² /cm ⁴ ·sec)
1200	7.08 x 10 ⁻¹⁵
1350	5.09 x 10 ⁻¹⁴
1500	7.64 x 10 ⁻¹³

TABLE 4.3: OXIDATION RATE CONSTANTS

Table 4.4 which is taken from reference (42) which show the oxidation rate constant as a function of time and temperature for various oxidizing atmospheres. Where

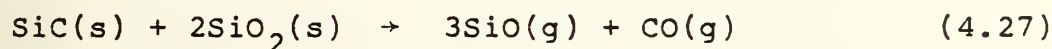
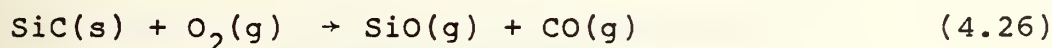
$$g = 4.98 \times 10^{-3} t^{.31} \quad \text{for } T = 1497^{\circ} \text{ C}$$

$$g = 3.34 \times 10^{-3} t^{.5} \quad T = 1647^{\circ} \text{ C}$$

where g is the weight change and t the oxidation time.

As may be expected, any impurities in the raw material base for SiC have detrimental effects on the oxidation rate of SiC. The impurities lower the viscosity of the layer, thereby causing an increased amount of oxidant to cross the layer to the silicon carbide base.

As detailed in Figure 4.9, active oxidation of SiC may also occur if the partial pressure of oxygen is sufficiently low. The active oxidation of SiC at low oxygen partial pressures occur according to the following equations:

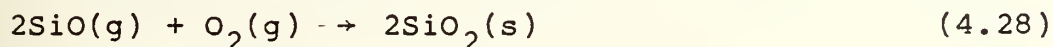


Though there is some disagreement about the details of active oxidation, it has been established that this

OXIDIZING ATMOSPHERE	TIME (HOURS)	OXIDATION RATE (mg/cm ² ·h) AT TEMPERATURE °C OF	
		1497	1647
Carbon Dioxide	0.25	2.43	3.41
	3.00	0.1	0.11
Air	0.25	1.6	6.6
	3.00	0.1	1.2
Water Vapor	0.25	1.1	5.2
	3.00	0.3	1.0
Oxygen	0.25	3.5	3.6
	3.00	0.3	0.76
	6.00	0.15	0.4

TABLE 4.4: OXIDATION OF POLYCRSTALLINE
SILICON CARBIDE

mode of reaction is initiated at any temperature when the ambient oxygen partial pressure or chemical potential, PO_2 at the SiC surface falls below a critical value determined by the thermodynamic equilibria at the SiO_2 -SiC interface. Experimental values for the critical active-passive transition pressure at temperatures in excess of 1100°C have been determined by Gulbransen and Jansson (28) and are shown by the solid line of Figure 4.13. In tabular form, the values of $P_{SiO}(eg)$ and $PO_{2(max)}$ for various temperature values are shown in Table 2.5. However, since oxygen pressures encountered in the new engine exhaust are higher than the values of $PO_{2(max)}$ of Figure 4.13 and Table 4.5, a stable $SiO_2(s)$ layer will be maintained on the surfaces of the SiC regenerator. Note that any $SiO(g)$ formed at the $SiC(s)$ - $SiO_2(s)$ interface will diffuse outwards through the pores and fissures in the surface oxide layers and will be oxidized to $SiO_2(s)$ by the reaction with gaseous oxygen in the surrounding atmosphere by the reaction



One final statement about the oxidation of SiC is that active oxidation always results in a weight loss of SiC by the formation of $SiO(g)$ and $CO(g)$ according to equations (4.26) and (4.27). On the other hand, passive

TEMPERATURE , °C

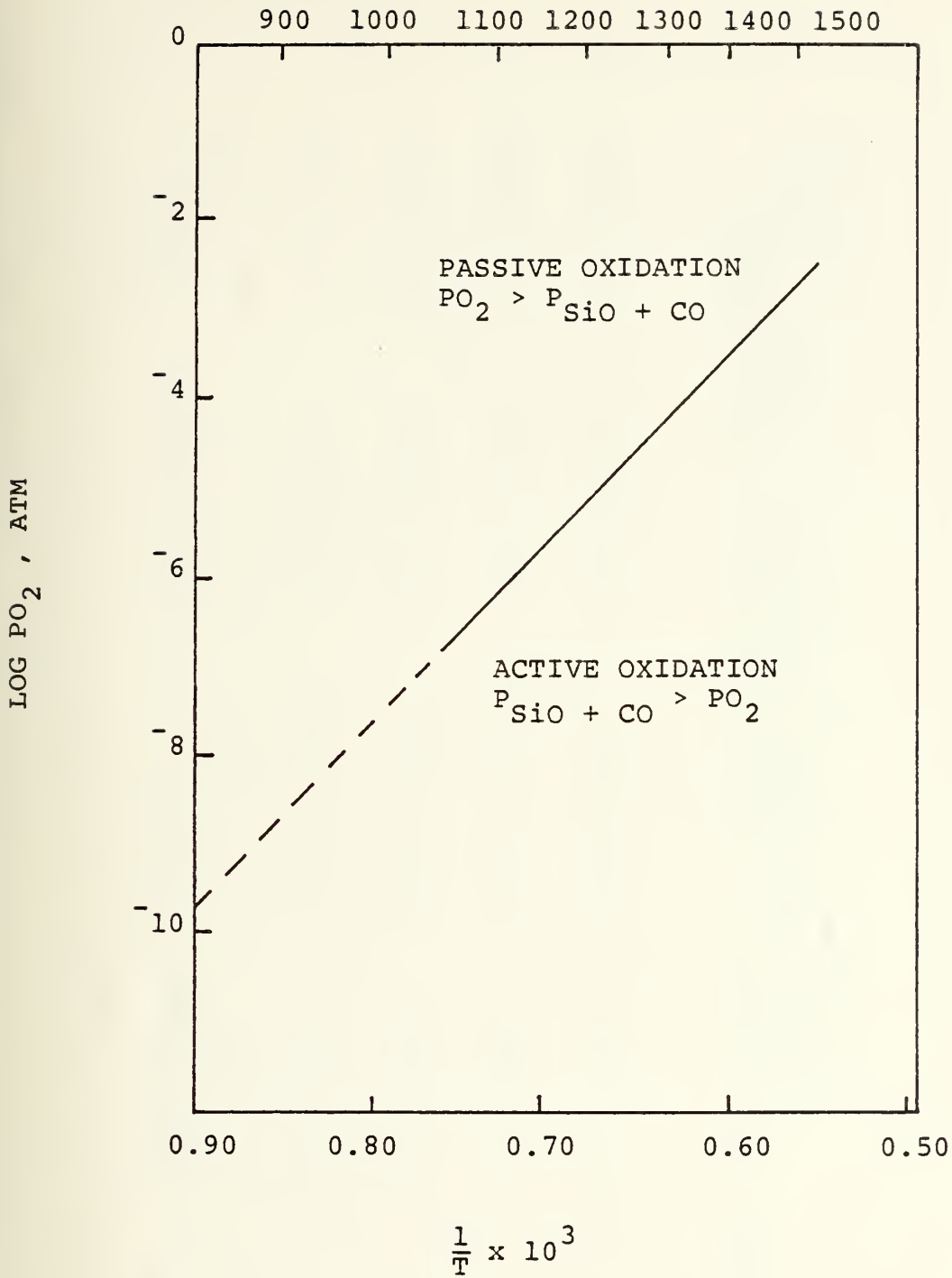


FIGURE 4.13: TRANSITION PRESSURES FOR
SiC ACTIVE-PASSIVE OXIDATION
VERSUS TEMPERATURE

TEMPERATURE (°C)	Si ₃ N ₄		SiC	
	P _{SiO(eq)} (atm)	PO ₂ (max)	P _{SiO(eq)} (atm)	PO ₂ (max)
927	3.3×10^{-7}	1.32×10^{-7}	1.2×10^{-7}	4.8×10^{-8}
1127	4.9×10^{-5}	1.96×10^{-5}	1.0×10^{-5}	8.0×10^{-6}
1327	2.0×10^{-3}	8.00×10^{-4}	9.0×10^{-4}	3.6×10^{-4}
1527	3.6×10^{-2}	1.44×10^{-2}	1.75×10^{-2}	7.0×10^{-3}
1727	3.5×10^{-1}	1.40×10^{-1}	1.82×10^{-1}	7.3×10^{-2}

TABLE 4.5: THEORETICAL VALUES OF EQUILIBRIUM PARTIAL PRESSURE, P_{SiO(eq)} AND MAXIMUM OXYGEN PARTIAL PRESSURE, PO₂(max) FOR REMOVAL OF ALL THE OXIDE ON Si₃N₄ AND SiC SURFACES

oxidation results in a weight gain of the SiC material due to the formation of $\text{SiO}_2(\text{s})$ according to equations (4.19) and (4.20).

4.6 Thermal Shock Comparison of Sintered Si_3N_4 and SiC

As mentioned in Chapter 3, thermal shock comparisons for the regenerator of the new engine are made using the R and R' parameters which best represent the steady heat flux conditions expected to be experienced by the regenerator. An examination of Table 4.6 using typical material property data for sintered Si_3N_4 and $\alpha\text{-SiC}$ indicate that Si_3N_4 is better suited for the largest ΔT allowed for steady heat flow while the $\alpha\text{-SiC}$ material is better suited under conditions of maximum heat flux for steady flow. Due to this inconclusive result, the value of strain tolerance, σ/E , was computed for each material and the linear coefficient of thermal expansion of both materials was also compared. These comparisons were made for the new cycle, because maximum efficiency of the heat-regenerator operation has been shown to be achieved through a thin walled matrix, where the fracture strength and strain tolerance are high and the linear coefficient of thermal expansion is at a minimum (14). The thermal shock parameter value, the strain tolerance value and the linear coefficient of thermal expansion advantages of Si_3N_4 compared to SiC (Table 4.6) are the basis for the

MATERIAL	FLEXURAL STRENGTH σ [psi]	POISSON'S RATIO ν	THERMAL EXPANSION α [IN/IN·°C]	ELASTIC MODULUS E [psi]	THERMAL CONDUCTIVITY k [CAL/CM·SEC·°C]	R [°C]	R' [CAL/CM·SEC]	σ/E
Si ₃ N ₄	58,800	0.27	3.96×10^{-6}	40×10^6	0.027	271	7.32	0.0015
SiC	48,200	0.12	5.3×10^{-6}	55×10^6	0.06	146	8.73	0.0009

$$R = \frac{\sigma(1-\nu)}{E\alpha}$$
$$R' = \frac{k\sigma(1-\nu)}{E\alpha}$$

Data from references 24, 29, and 35

TABLE 4.6: THERMAL SHOCK PARAMETERS FOR SINTERED Si₃N₄ AND SiC

figure of merit rating assigned to each of the materials in Table 4.2.

4.7 Thermal Conductivity Comparison of Sintered Si_3N_4 and SiC

The thermal conductivity values of sintered Si_3N_4 and SiC at 1200°C are approximately $0.027 \text{ cal/cm}\cdot\text{sec}\cdot^\circ\text{C}$ and $0.06 \text{ cal/cm}\cdot\text{sec}\cdot^\circ\text{C}$, respectively. Figures 4.14 and 4.15 (20) illustrate the thermal conductivity values for SiC and Si_3N_4 as a function of temperature. The curves of Figures 4.14 and 4.15 illustrate tendencies identical to equation (3.6). Based upon the data stated in this paragraph and the desirability of having a ceramic material with a low thermal conductivity value, the figure of merit ratings for Si_3N_4 and SiC are assigned as shown in Table 4.2 for the thermal conductivity parameter.

4.8 Fabricability of Sintered Si_3N_4 and SiC

The differences between fabricating a regenerator made from Si_3N_4 material versus a SiC material are minimal. Since both materials have starting powders consisting primarily of high purity silicon powder of greater than 98.5 percent, the major difference between the two materials in terms of fabricability, is the sintering aids required and length of sintering. Si_3N_4 requires fine yttrium oxide powder (5 μm average) at a concentration of 8 weight percent to obtain a density of

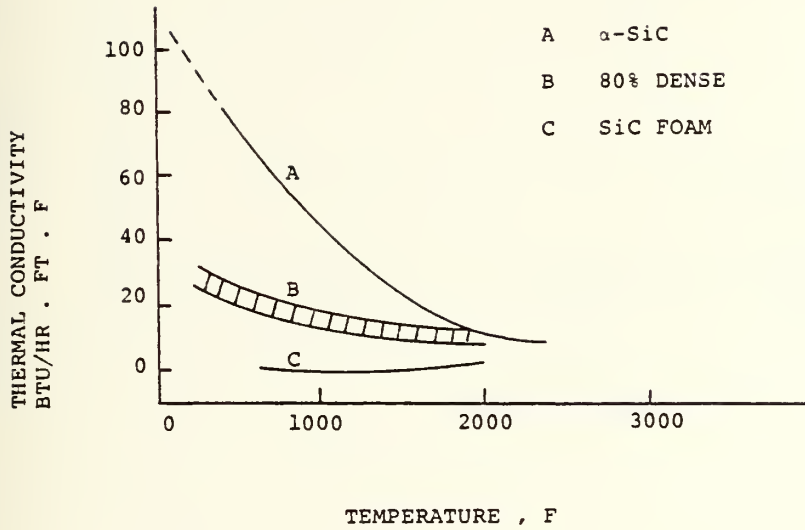


FIGURE 4.14: THERMAL CONDUCTIVITY OF SiC

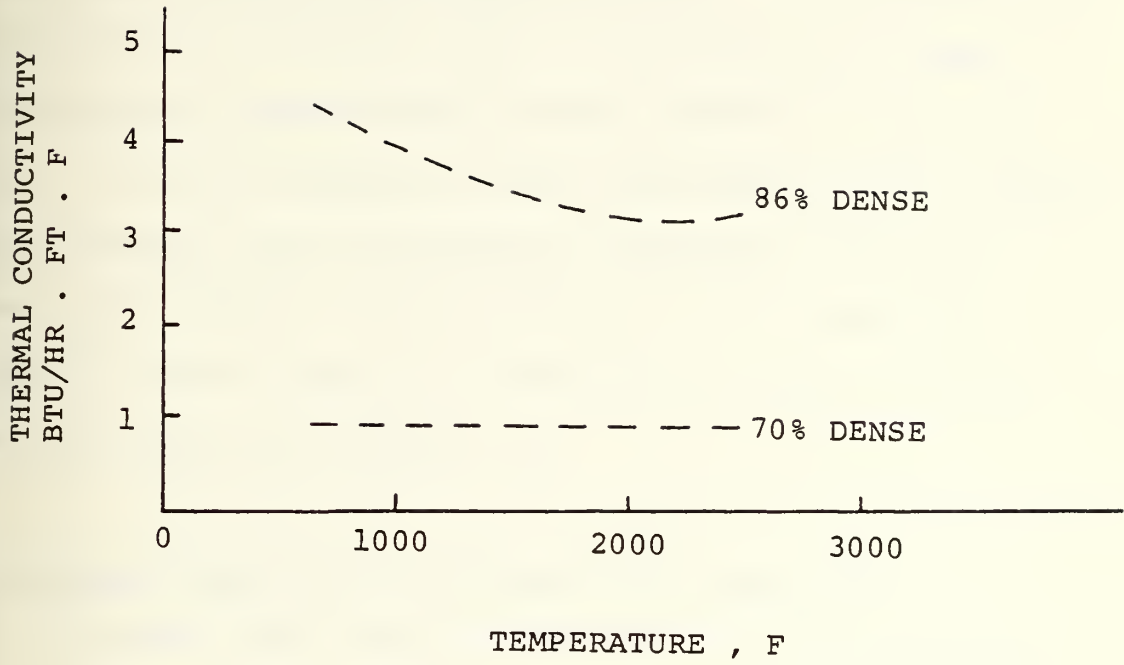


FIGURE 4.15: THERMAL CONDUCTIVITY OF Si_3N_4

3.27 g/cm³ (97 percent of theoretical). Densification is by liquid phase sintering and is carried out in a nitrogen atmosphere at temperatures between 1800^o-1925^oC for four hours. On the other hand, SiC requires 0.5 weight percent boron and 3 weight percent carbon to obtain a density of 3.08 g/cm³ (96 percent of theoretical). Densification is by solid state sintering and is conducted in an argon atmosphere at temperatures of about 2000^oC for one half hour. From this comparison, the fabricability of sintered Si₃N₄ and SiC into the required regenerator shape and design are similar. This accounts for the identical figure of merit values for fabricability given to both ceramic materials in Table 4.2.

4.9 Cost Comparison of Sintered Si₃N₄ and SiC

A direct cost comparison between sintered Si₃N₄ and sintered SiC could not be found in the literature. However, on the basis of raw material, fabrication, sintering and machining comparisons, it appears that the cost for production of a Si₃N₄ regenerator is about equal to the cost incurred by the production of a SiC regenerator. If however, the Si₃N₄ regenerator is treated by additional process steps to improve its strength and oxidation characteristics to make it comparable to the SiC regenerator, the cost of the Si₃N₄ regenerator may be significantly increased (21). Process steps such as

chemical vapor deposit (CVD) to increase the resistance to oxidation and chemical attack, and post-heat treatment to increase the strength of the Si_3N_4 regenerator are two process steps currently under investigation. The literature however does not detail quantitatively the costs of these two processing steps, therefore, the figure of merit values for cost for sintered Si_3N_4 and sintered SiC are assumed to be equal as in Table 4.2. This assumption is made with the knowledge that sintered SiC probably has a slight cost advantage compared to sintered Si_3N_4 , but the amount or percent is not known.

CHAPTER 5

MANUFACTURING AND FABRICATING PROCESS5.1 Introduction

The properties of ceramic materials can be influenced by the processing technique utilized to a greater degree than most other materials. Metal alloys are manufactured by several companies to established specifications, and it makes little difference to the user who the manufacturer might have been. In the ceramic industry however no such system exists. A sampling of property data from manufacturers of similar ceramic materials reveal that there are no two compositions having identical properties and the major reason for this difference is due to differences in the processing techniques used by each manufacturer which in turn affects the properties of the final product.

Though there are a wide variety of ceramic fabrication processes, the basic steps of each of the ceramic fabrication processes are similar. Figure 5.1 is a simplified representation of the major steps. Both MAS and α -SiC ceramic materials follow the basic steps outlined in Figure 5.1. To provide the necessary detail and to avoid confusion, each ceramic material selected for the two temperature ranges will be discussed individually.

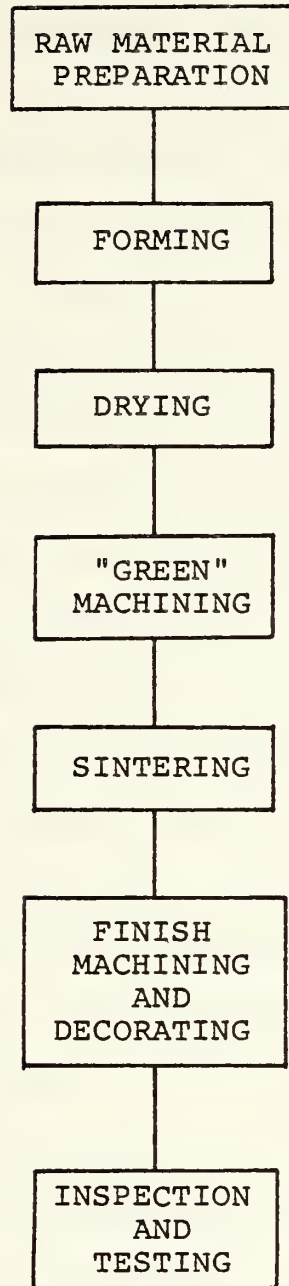


FIGURE 5.1: BASIC STEPS OF THE CERAMIC FABRICATION PROCESS

5.2 α -SiC

As mentioned previously, the properties of a ceramic material are attributable to specific events in the component's processing history, extending from powder synthesis through all the handling steps to the final consolidation into a densified part. To achieve the desired level of property reliability requires that the starting powders fulfill both physical and chemical characteristics. The physical requirements include fineness, homogeneity (single-phase), narrow size distribution, non-agglomerated, and equiaxed shape.

There are currently two sources of SiC powders meeting all or most of these physical requirements. One source is the Carborundum Company (43), the other source is the SiC powder produced by the Department of Materials Science and Engineering at Massachusetts Institute of Technology (44, 45). The Carborundum Company produces a 6H silicon carbide powder of 99.5 percent SiC purity with an average particle size of 0.4 microns and surface area of $12.3 \text{ m}^2/\text{gm}$. The impurities contained are as follows in ppm: oxygen (3300), Fe (100), V (40), Se (20), Ti (20), Mg (9), Cu (6), free C (2400) and free Si (2500). The SiC powder developed at the Massachusetts Institute of Technology is synthesized from CO_2 laser heated gas phase reactions having mean diameters of 0.02 to 0.05 μm with a standard deviation of about 25 percent of the mean

diameter. The major impurity contained in the powder in ppm by weight is O_2 at 3,300 to 13,000.

5.2.1 Raw Material Preparation of SiC

With the selection of either one of these SiC powders, the fabrication processes of Figure 5.1 can commence. The silicon carbide powder with its required additives (Section 5.2.5) are mixed in a ball mill jar in the wet condition. A ball mill, shown in Figure 5.2, is a steel cylinder rotating at a relatively low speed, lined with porcelain or aluminum blocks and is usually half full of porcelain or alumina balls. As the mill rotates, the balls roll over one another in the lower portion of the mill, creating a high shear force on the grains of ceramic material between the balls. The result of this mixing is a fine-grained homogeneous mixture. Since silicon carbide is mixed in the wet condition during milling, filtering the water out by either filter presses or vacuum filters is required prior to forming by extrusion. The silicon carbide mixture is also passed through fine screens to remove unmilled and foreign material, and is further processed through a magnetic separator to remove any unwanted iron particles.

5.2.2 Forming the SiC Regenerator

At this point in the ceramic fabrication process, the raw material powder is ready for consolidation and

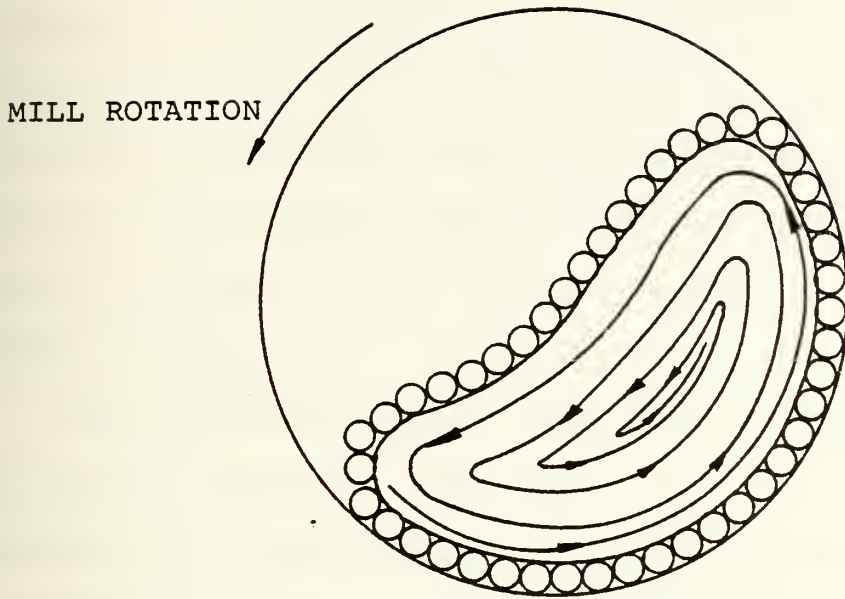


FIGURE 5.2: BALL MILL

production into the desired shape. The choice of which forming method to use depends upon several factors. The most important factor in fabricating a regenerator is the size and shape constraints imposed by the flow passage geometry selected for the regenerator. Table 5.1 summarizes the major forming processes. A review of these forming processes leads to the conclusion that only the tape forming techniques known as corrugating and embossing along with the plastic forming technique of extrusion are capable of producing the required regenerator passage geometry tolerances.

The corrugated process dates back to the early 1950's and is well developed. See Figure 5.3 for a pictorial description of this process. For this process, variations in corrugating roll pressure, winding tension and shrinkages during firing can produce significant discrepancies in cell geometry. Due to this resulting cell non-uniformity and because researchers at NASA/FORD (4, 8, 15) have shown that cell non-uniformity results in serious performance losses, the corrugating process was eliminated as a possible forming process.

The embossing technique consists of forming ribbed tape by either extruding or calendering a flat ceramic sheet which is then embossed or wrapped around a mandrel to produce a rectangular passage regenerator as illustrated in Figure 5.4. The most difficult aspect of

PRESSING	:	UNIAXIAL PRESSING ISOSTATIC PRESSING HOT PRESSING HOT ISOSTATIC PRESSING
CASTING	:	SLIP CASTING THIXOTROPIC CASTING SOLUBLE-MOLD CASTING
PLASTIC FORMING:		EXTRUSION INJECTION MOLDING TRANSFER MOLDING COMPRESSION MOLDING
OTHERS	:	TAPE FORMING FLAME SPRAY GREEN MACHINING

TABLE 5.1: MAJOR TECHNIQUES FOR POWDER
CONSOLIDATION AND SHAPE FORMING

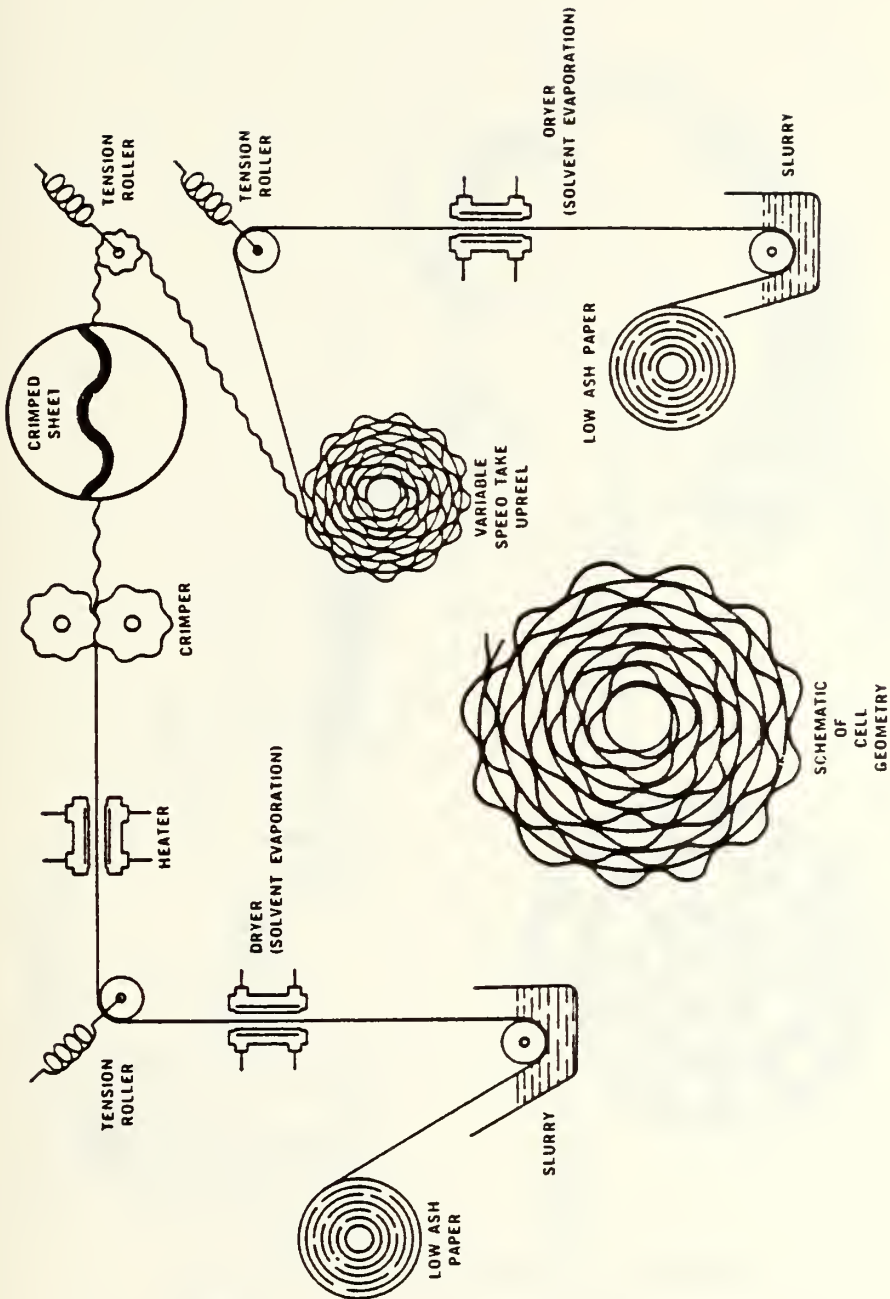


FIGURE 5.3: TYPICAL COATED PAPER WRAPPING OPERATION

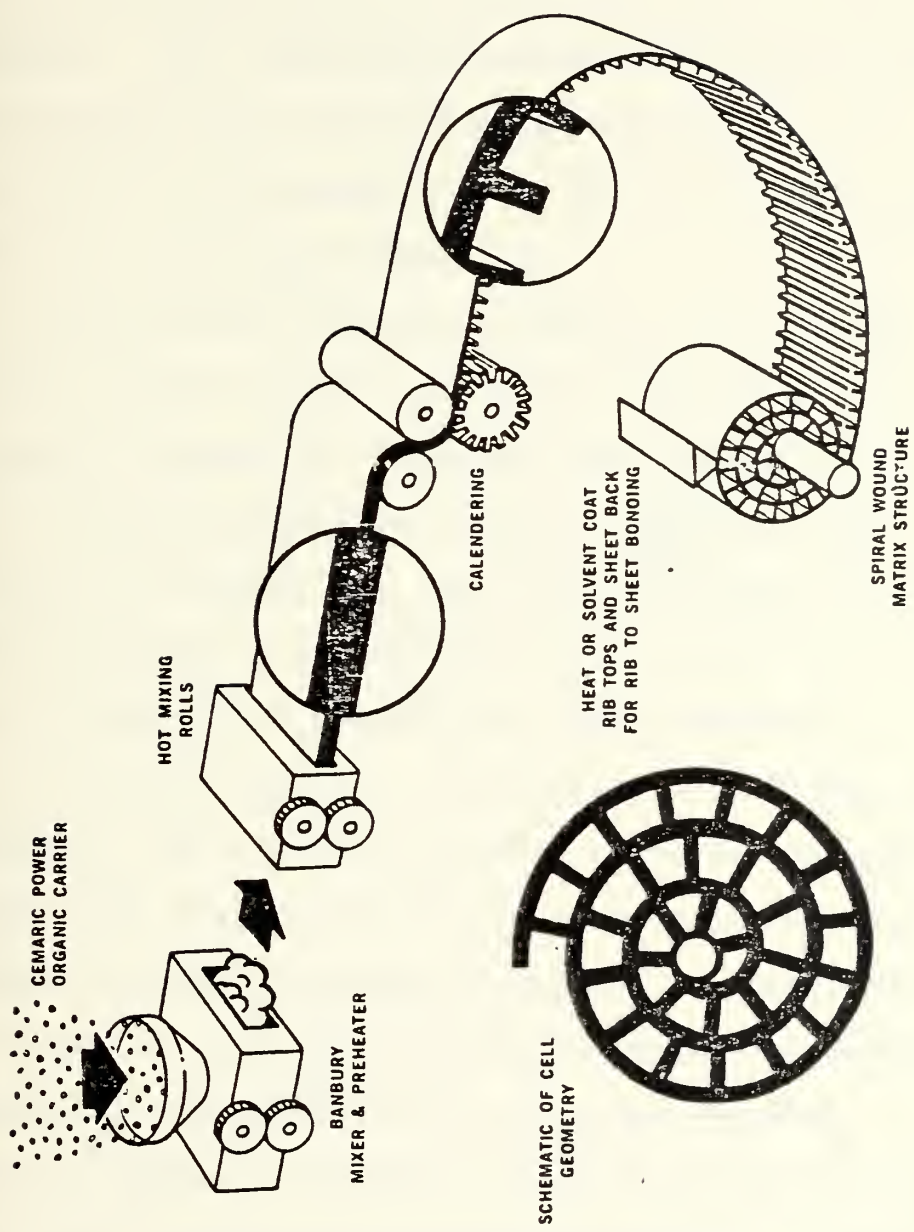


FIGURE 5.4: TYPICAL CALENDERING OPERATION

embossing thin wall matrices is filling the groove in the embossing roll to obtain uniform fin height with a very thin rib. The embossed tape is susceptible to buckling of either the rib or back web if the rib is too high, which ultimately leads to cell non-uniformities and subsequent uneven flow distribution into the matrix and a loss in performance. The likelihood of producing non-uniform cells throughout the regenerator matrix caused the elimination of the embossing process as a feasible forming process for a SiC regenerator.

In the extrusion process, Figure 5.5, a die can be machined to form a variety of passage geometries such as the square or isosceles triangular cell shapes, which have proved to have desirable performance characteristics (discussion in Chapter 6). The major advantage of the extrusion process is the ability of the extruder to yield the most uniform cell geometry and wall thickness, resulting in more efficient flow passages throughout the regenerator. The extrusion process requires the most development (and is currently the subject of the greatest developmental effort) since the process was developed only ten years ago. Analytical results conducted by NASA/FORD concluded that the better quality of the extruded structure compared to an embossed matrix would provide a 2 percent gain in regenerator effectiveness (8). Through the recent volume production of extruded matrices as

CERAMIC POWDER
AND ADDITIVES

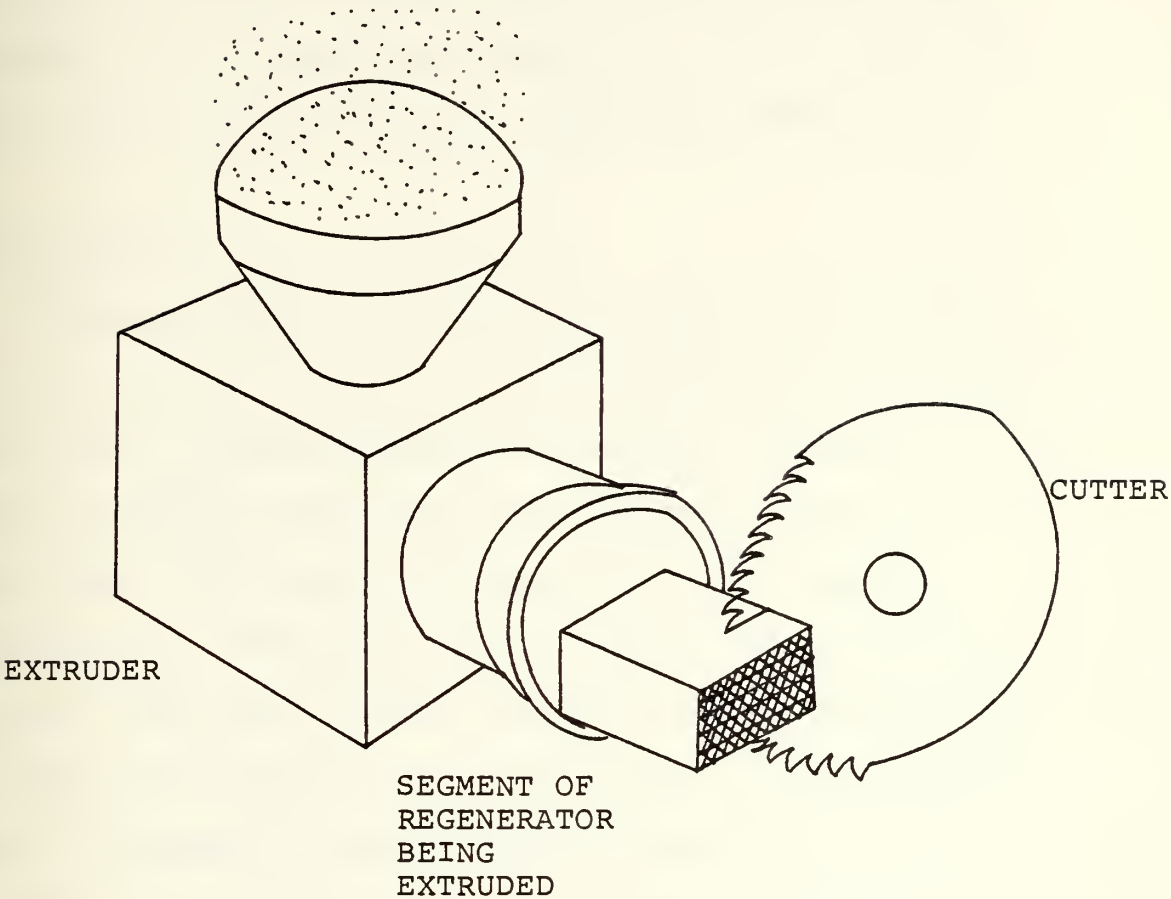


FIGURE 5.5: TYPICAL EXTRUSION OPERATION FOR
FABRICATING A CERAMIC REGENERATOR

automotive catalyst substrates, which have proved highly successful, and because of the inherent superior cell uniformity of this process, the extrusion process was selected as the forming process best suited to meet the needs and requirements of the new cycle regenerator.

5.2.3 Drying

Products made by wet processes such as extrusion usually contain from 5 to 20 percent by weight of water which must be removed before sintering. Although it is a simple process, drying does contain many pitfalls which will affect the material properties of the ceramic regenerator. Since water can be evaporated only from the surface, the rate of water removal from the surface must be equal to or greater than the rate of water migration from the interior regions of the regenerator to the surface. Warping and cracking will result if this drying is not done properly (46, 47). Periods of air drying are often utilized prior to entering the drying ovens, and humidity controls are often employed. The operation and tendencies of such a drying scheme is illustrated in Figure 5.6.

5.2.4 Machining

Another important operation performed before sintering, is machining. Since most ceramics are very

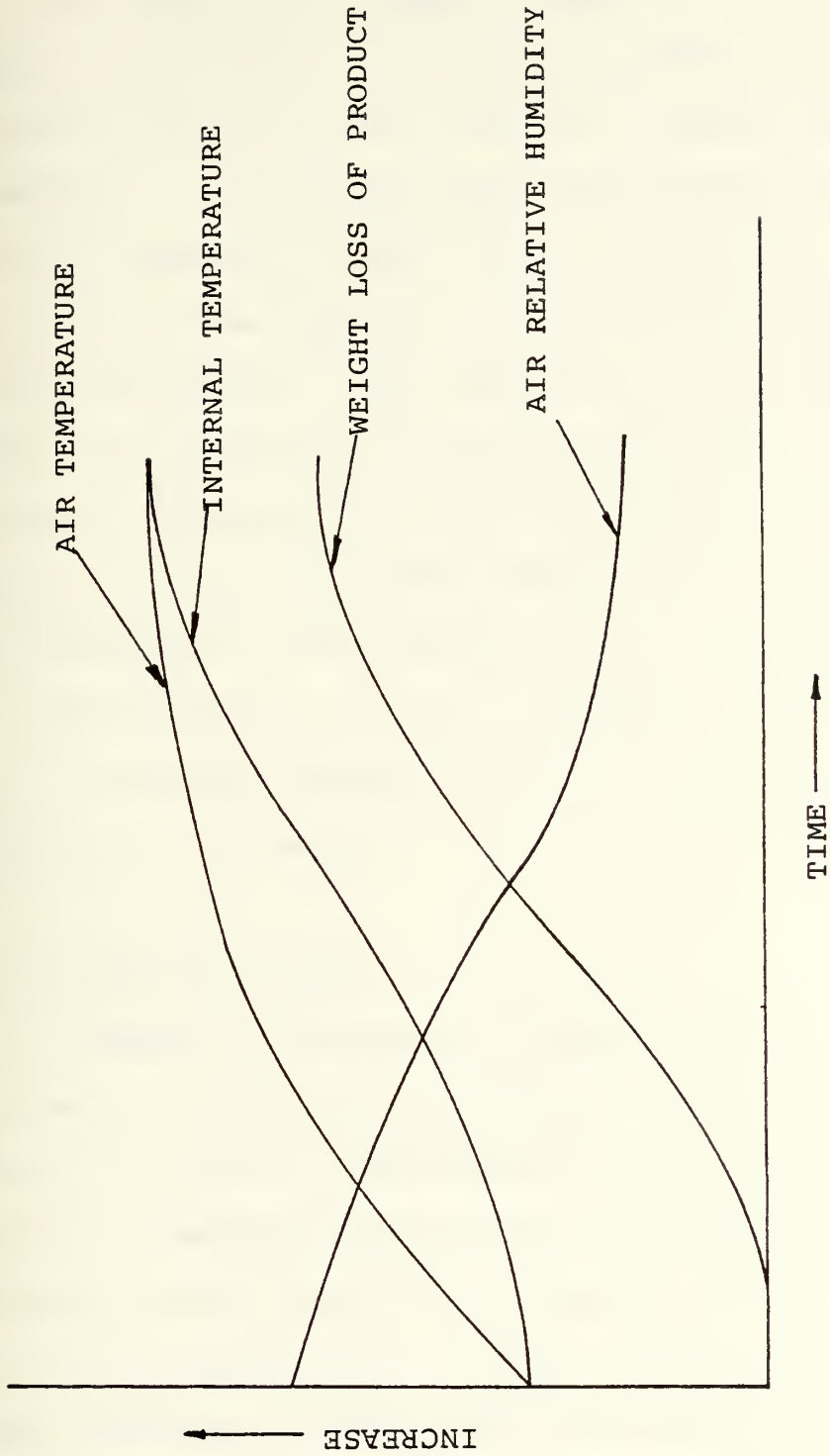
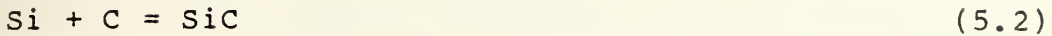
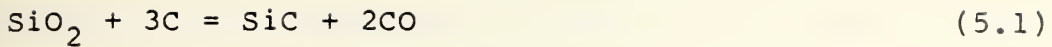


FIGURE 5.6: CHANGES IN TEMPERATURE, WEIGHT LOSS, AND RELATIVE HUMIDITY DURING DRYING CYCLE

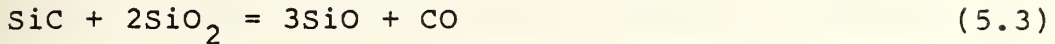
hard after sintering and require machining by diamond grinding if performed, it is more economical to machine the ceramic article in the unfired or "green" state if at all possible. As a general rule, dimensional tolerances can be maintained no closer than one percent by "green" machining of those ceramic materials having normal sintering shrinkage. The literature does not address whether SiC regenerator matrices are machined prior to sintering. However, due to the intricate passage geometry envisioned for the regenerator matrix, and due to the very small dimensions of the passages, it is highly unlikely that "green" machining will be performed on the SiC matrix prior to sintering, except possibly on the outer extremities of the matrix.

5.2.5 Sintering of SiC

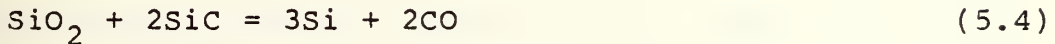
In addition to the general comments stated in Section 4.2, there are many specific details required for the sintering of α -SiC. Experimental work has shown that the cessation of densification in SiC is strongly impurity dependent and that oxygen and elemental silicon are the main contributing factors. Powders with low oxygen content invariably exhibit more densification than powders rich in oxygen. Carbon, C, is required as a sintering aid for α -SiC for deoxidizing and desiliconizing according to the following two reactions



It might be expected that the reaction



would be sufficient to deoxide the system without the assistance of carbon, but probably the simultaneous reaction



forms silicon which also inhibits sintering. Thus, carbon is necessary to deoxidize and desiliconize the SiC system while at the same time increasing the effective surface energy, γ_{SV} , of the α -SiC particles by the cleansing action of equations (5.1) and (5.2).

Boron, B, is also required as a sintering aid in α -SiC. Boron is required to reduce the grain boundary energy of the α -SiC particles by diffusing into the grain boundary, thereby reducing the grain boundary energy, γ_{GB} . This reduction of γ_{GB} and increase of γ_{SV} causes the grain boundary to surface energy ratio, γ_{GB}/γ_{SV} , to fall below a critical value, which allows for the formation and

extension of grain boundaries leading to sintering of the α -SiC particles (34, 48, 49, 50).

Boron is best added in elemental form and carbon in solution as an organic decomposable substance during raw material preparation and mixing. The literature indicates that to attain high density pressureless sintered α -SiC, 0.5 weight percent B with 3 weight percent C sintered at 2060°C for 30 minutes in an argon atmosphere results in a density of 3.08 g/cm³ or 96 percent theoretical (36). The resulting grain sizes are generally 1-5 μ m with occasional 10 μ m grains.

Fluctuations in the boron and carbon concentrations mentioned above are detrimental to the proper sintering of α -SiC. Though increasing the carbon content results in a smaller grain size, the additional carbon concentration may create larger pore sizes. Higher concentrations of boron result in a coarsening in the grains. The resulting microstructure of a boron rich mixture is very inhomogeneous, with elongated grains up to 40 μ m for a boron content of 2.4 weight percent. The large increase in grain size and the high local concentration of boron indicate a liquid phase sintering process as a densification process rather than the normal solid state densification process (36). Higher sintering temperatures likewise increase grain size (43).

5.2.6 Finish Machining and Inspection

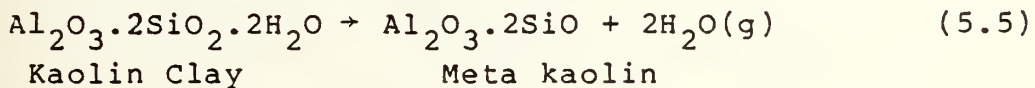
Since close dimensional control of the regenerator matrix is a must in the new cycle design, finish machining will be required. Wet grinding using diamond-impregnated metal wheels is the conventional technique. It is envisioned that the tolerances and dimensions of the regenerator matrix will require the diamond grinding operation to be automated with machined tolerances of less than 0.001 inch the norm while using high volume centerless diamond grinding.

The inspection process is required in all the steps of the fabrication process as outlined in Figure 5.1 to produce a good quality silicon carbide regenerator matrix. One of the most critical quality control steps in the process, is the forming operation of extrusion. It is imperative that the density of the unfired product at the forming step be sufficiently large to adequately control the final dimensions of the regenerator. The "green" density of the SiC regenerator must be greater than 50 percent or 1.605 g/cm^3 to ensure that the final density be greater than 95 percent and to prevent the possibility of excess shrinkage, leading to an undersized regenerator. Other difficulties encountered during the forming step are the formation of cracks, internal flaws, voids and contamination from the extruder die.

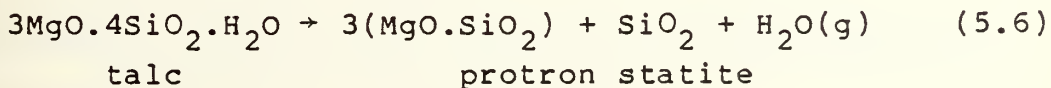
The measuring and testing of the SiC regenerator will likely be performed immediately after sintering. Evaluation of the SiC regenerator will be performed on a statistical basis, following the procedures documented in references (54) and (55). It is expected that quality levels of 99 percent of acceptable product yield can be achieved through tightly controlled manufacturing processes (46).

5.3 MAS

MAS has three possible raw material selections. They are raw mineral, calcined mineral and glass frit. The typical MAS raw material preparation would include weighing and mixing of high purity talcs, clays and aluminum oxide. In a calcining process, the batch is heated between 500° to 1000°C for a short period to remove all or part of the clay hydroxyl according to the following reaction



Calcining of the talc occurs as



Some calcining is performed at 1000°C to convert some meta kaolin to mullite and cristobalite according to the reaction

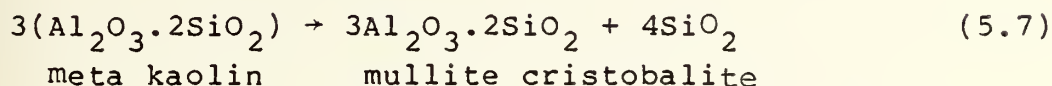


Figure 5.7 is a simplistic description of the steps required for the three different raw materials, from selection of the raw material to the finished product. The calcining process is selected primarily for its distinct advantage of reducing the firing shrinkage while still maintaining a high chemical reactivity during sintering which is associated with using clays and talc. Though mineral MAS is 10 percent cheaper to produce than calcined or frit MAS, calcined MAS is selected due to its distinct shrinkage advantage.

5.3.1 Forming the MAS Regenerator

Upon completion of mixing the calcined MAS raw materials, the homogeneous mixture undergoes a water removal process and filtering process to remove foreign material, exactly like the α -SiC raw material.

The calcined MAS material is now ready for consolidation and forming using the extrusion process detailed previously in Section 5.2.2.

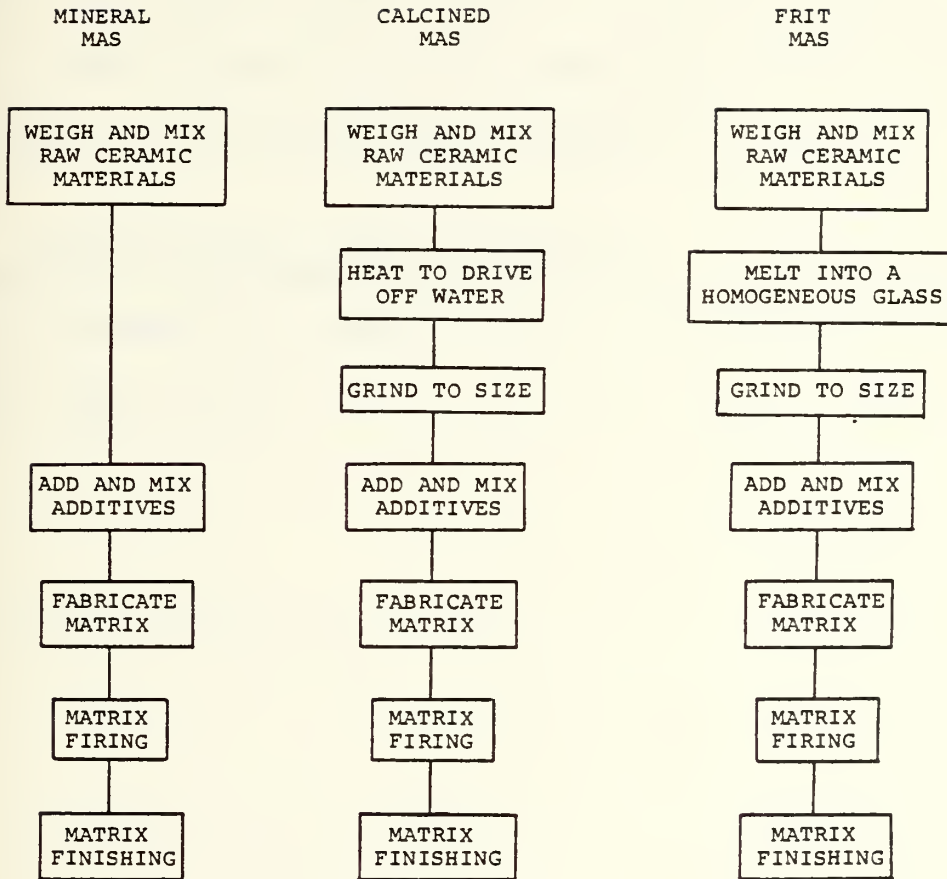


FIGURE 5.7: MAS MANUFACTURING PROCESS STEPS

5.3.2. Drying and Sintering the MAS Regenerator

Matrix firing commences by the removal of organic material at low kiln temperatures and culminates in chemical reactions occurring at high temperatures which yield the desired matrix properties. Maximum firing temperatures for calcined MAS is 1425°C . There are currently two types of kilns used to fire the "green" matrix, tunnel or periodic. For most high volume firing applications, the tunnel kiln is desired.

5.3.3 Finish Machining and Inspection

The comments of Section 5.2.6 are also applicable to the MAS regenerator.

PASSAGE GEOMETRY ANALYSIS6.1 Introduction

An optimum ceramic regenerator design requires an effective compromise between thermal and mechanical stress capabilities combined with aero-thermodynamic performance potential. Aerothermodynamic performance properties measure the ability of the regenerator to transfer heat effectively to and from the working fluids, to store heat in the regenerator with little conductance loss and to perform these functions with a minimum fluid pressure drop across the regenerator.

6.2 Aero-thermodynamic Analysis

A measure of the heat transfer characteristics is the Colburn Number, J , and the Fanning Friction Factor, F , which indicate the pressure drop characteristics of the regenerator. Both dimensionless parameters are functions of Reynold's Number, Re , for a given regenerator geometry and are defined as

$$J = C_2 Re^{x_2} \quad (6.1)$$

$$F = C_1 Re^{x_1} \quad (6.2)$$

where C_1 is the Fanning Friction Factor constant for laminar flow, C_2 is the Colburn Number constant for laminar flow, x_1 the Reynold's number exponent for Fanning Friction Factor, and x_2 the Reynold's number exponent for the Colburn Number.

Since erroneous estimates of the fin parameters such as open area ratio, σ , and hydraulic diameter, DH , can introduce significant discrepancies into the J and F curves, an alternate set of heat transfer and pressure drop characteristics which eliminate the necessity of estimating fin parameters was derived. The alternate characteristics allow a direct comparison of test data from different sources, since a universal method of determining pertinent fin parameters is non-existent at this time. The alternate pressure drop, $(\Delta P \cdot \frac{P}{L})$, and heat transfer, $\frac{NTU}{L}$, characteristics can be expressed in the following forms:

$$\frac{NTU}{L} = A \left| \frac{A_F T^{0.673}}{\dot{W}} \right|^{-x_2} \quad (6.3)$$

$$\Delta P \cdot \frac{P}{L} = C \left| \frac{\dot{W}(T^{0.673})}{A_F} \right| \quad (6.4)$$

where

$$C = 3.56 \times 10^{-9} \frac{C_1}{\sigma_{DH}^2} \quad (6.5)$$

$$C = \left| 3.506 \times 10^{-10} \frac{C_1}{\sigma_{DH}^2} \right| \quad (6.5a)$$

and

$$A = 4.98 [62.6 \times 10^{-7}]^{-x_2} \frac{C_2 \sigma^{-x_2}}{DH^{(1-x_2)}} \quad (6.6)$$

$$A = \left| 4.98 [21.9 \times 10^{-7}]^{-x_2} \frac{C_2 \sigma^{-x_2}}{DH^{(1-x_2)}} \right| \quad (6.6a)$$

T - fluid temperature $^{\circ}\text{K}$ ($^{\circ}\text{R}$)

ΔP - matrix pressure drop KPa (psi)

P - fluid pressure KPa (psia)

L - flow length cm (in)

W - air mass flow rate kg/sec (lbm/sec)

A_F - matrix frontal area m^2 (ft^2)

σ - open area ratio

DH - hydraulic diameter cmn (in)

NTU - by definition is the number of heat transfer units (determined from the maximum slope of the fluid temperature difference curve during the cooling transient)

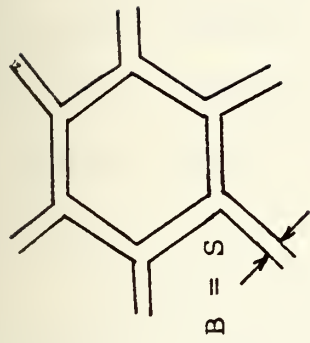
Once constants C and A have been determined from the equation of the line for the alternate performance characteristics, the pertinent constants C_1 and C_2 for the basic performance characteristics can be determined from the estimated values of σ and DH .

6.3 Passage Geometries Analyzed

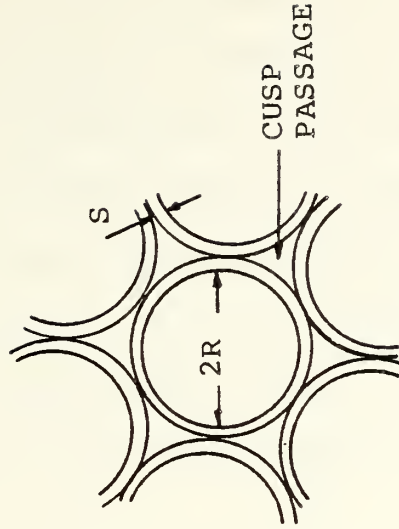
Five different passage geometries were analyzed. Figure 6.1 illustrates the different passage geometries and associated dimensions.

Initial experimental results among sinusoidal, square and isosceles triangular passage geometries indicated that for a fixed sized regenerator, the isosceles triangle was the best of the three geometries based upon a gross measure of the overall fin efficiency defined as the ratio of $J/F = C_2/C_1$ (4). The alternate performance characteristics which allows for a direct comparison of these fin geometries for a fixed regenerator size at identical flow conditions with the wall thickness and sample uniformity factored in, illustrated the importance of minimizing the wall material thickness (4). It has been determined that extremely thin wall thicknesses compensate for a lower heat transfer characteristic which produce slightly better heat transfer effectiveness with a significantly lower pressure drop (15).

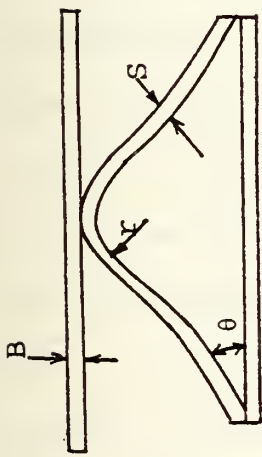
Researchers at the Ford Motor Company have determined that when selecting the best existing fin geometry for a



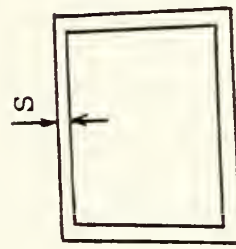
HEXAGONAL



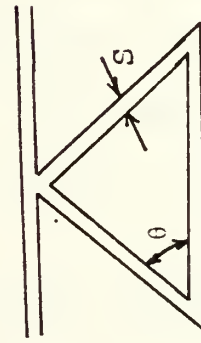
CIRCULAR



SINUSOIDAL



RECTANGULAR



TRIANGULAR

- B: PLATE THICKNESS
 S: FIN THICKNESS
 θ : SHAPE ANGLE
 r: RADIUS OF CURVATURE
 R: RADIUS OF CIRCLE

FIGURE 6.1: PASSAGE GEOMETRIES

given regenerator size and flow conditions, passage geometry, material thickness and limitations of the method of fabrication must be considered. By using the alternate heat transfer, A , and pressure drop, C , parameters, these factors are accounted for in matrices fabricated from existing tooling. To select the most efficient fin shape, the heat transfer, J , and pressure drop, F , characteristics are used since the wall thicknesses of the matrices are factored out.

This is the procedure followed and presented in Figure 6.2 which is based upon the actual openings of the fin configuration with the material wall thickness factored out. Table 6.1, the data for Figure 6.2 clearly illustrates the effectiveness of the isosceles triangle compared to the sinusoidal, square and rectangular geometries. The matrices listed are representative of each passage geometry. Figure 6.3 and Table 6.2, the data for Figure 6.3, provide for direct comparison of existing fin geometries for a fixed regenerator size at identical flow conditions with the material wall thickness factored in. In both comparisons, the isosceles triangle passage geometry produces the most effective aero-thermodynamic characteristics.

However, investigators at Sanford University have concluded, that theoretically, the performance characteristics of hexagonal and circular passages are

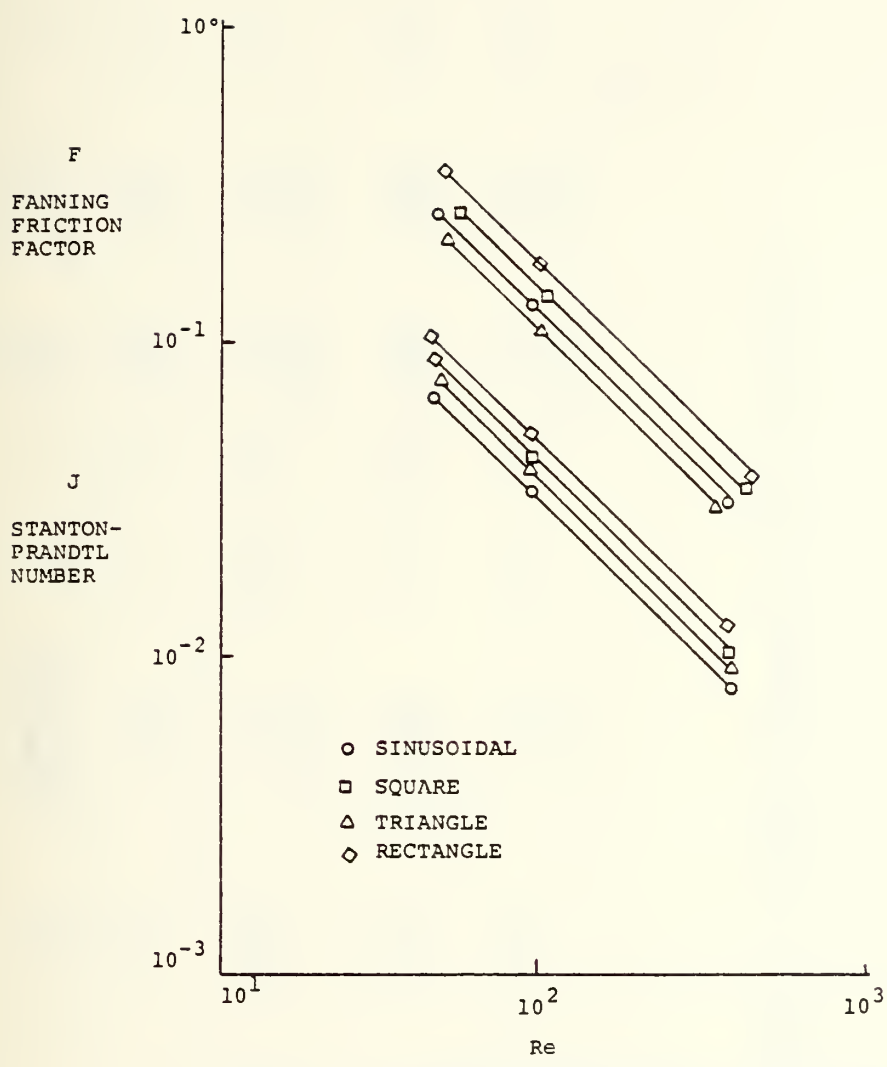


FIGURE 6.2: STANDARD THERMODYNAMIC PERFORMANCE CHARACTERISTICS

MATRIX PASSAGE	S (IN)	N HOLES/CM ² (HOLES/IN ²)	AR σ	DH MM (IN)	M ² /M ³ (FT ² /FT ³)	C ₁	X ₁	C ₂	X ₂	J/F
Sinusoidal	.0043	143 (924)	2.74 .673	.590 (.0232)	4566 (1392)	13.4	-1	3.34	-1	.249
Square	.0076	139 (900)	1.40 .599	.655 (.0258)	3654 (1114)	14.0	-1	4.19	-1	.299
Triangle	.0053	143 (924)	1.31 .642	.589 (.0232)	4356 (1328)	10.9	-1	3.93	-1	.361
Rectangle	.0015	83 (533)	4.57 .505	.645 (.0245)	3129 (954)	17.5	-1	5.0	-1	.287

TABLE 6.1: MATRIX CONFIGURATION DATA FOR FIGURE 4.2

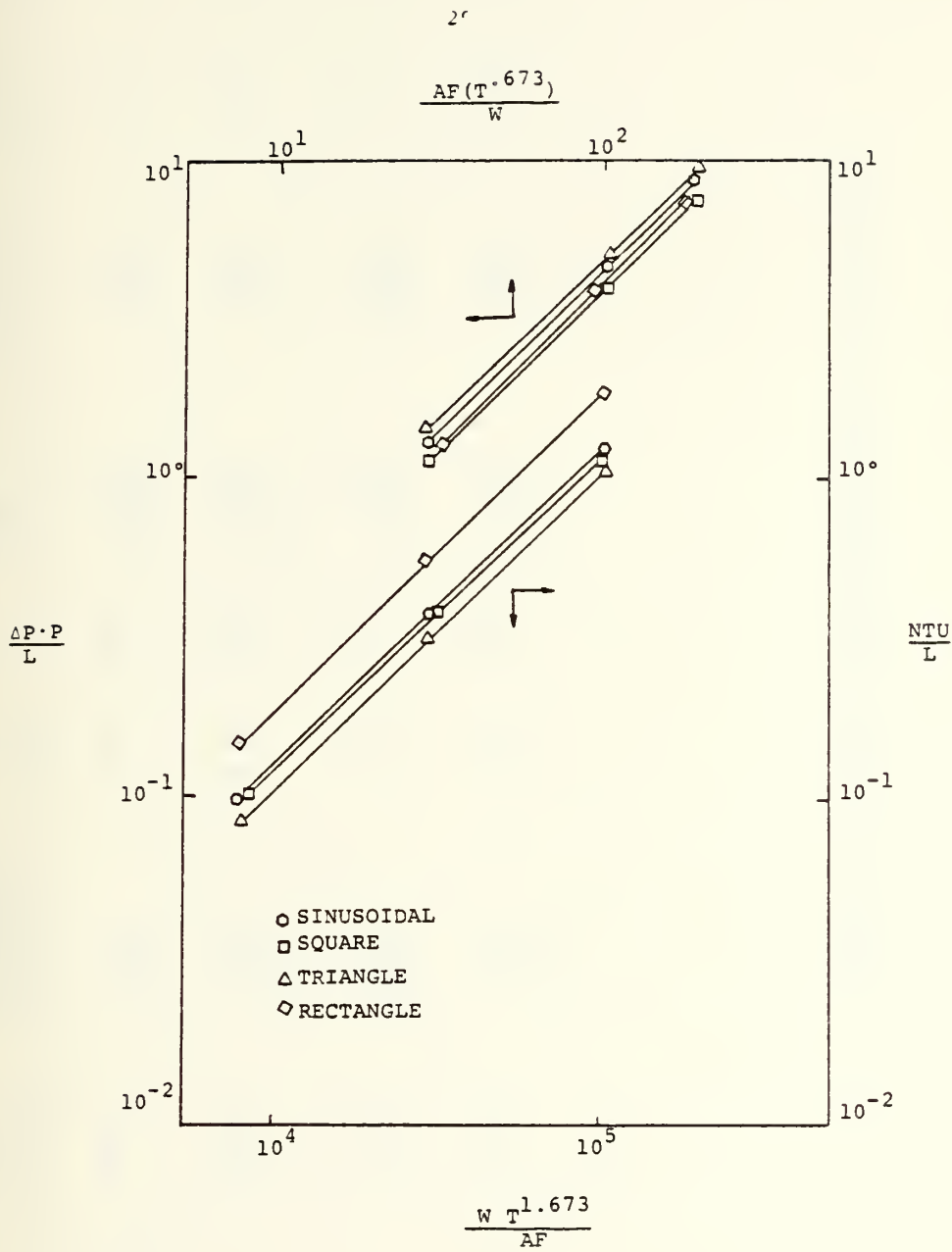


FIGURE 6.3: ALTERNATE THERMODYNAMIC PERFORMANCE CHARACTERISTICS

MATRIX PASSAGE	S (IN)	N HOLES/CM ² (HOLES/IN ²)	AR	σ	DH MM (IN)	M ² /M ³ (FT ² /FT ³)	C x 10 ⁵	A x 10 ²	A/C x 10 ⁻³
Sinusoidal	.0043	143 (924)	2.74	.673	.590 (.0232)	4566 (1392)	1.30	4.55	3.50
Square	.0076	139 (900)	1.40	.599	.655 (.0258)	3654 (1114)	1.23	4.11	3.34
Triangle	.0053	143 (924)	1.31	.642	.589 (.0232)	4356 (1328)	1.11	5.11	4.60
Rectangle	.0015	83 (533)	4.57	.505	.645 (.0254)	3129 (954)	1.89	4.29	2.27

TABLE 6.2: MATRIX CONFIGURATION DATA FOR FIGURE 4.3

significantly better than those of the equilateral triangular passage (51). By comparing Figures 6.4 and 6.5, which describe the design equations for the hexagonal and circular passages, respectively, an approximate gross overall fin efficiency ratio J/F of both geometries can be calculated. From the data presented in Figures 6.4 and 6.5, the circular passage seems to be more desirable when the analysis is performed on an aero-thermodynamic basis. However, the analysis which produced Figures 6.4 and 6.5 did not deal with:

1. Increased friction due to gross blockage of some flow passages.
2. Non-uniform flow distribution between adjacent passages due to passage-to-passage flow area non-uniformities.
3. Influence of cusped passages on the surface characteristics of circular tube matrices.

After consideration of the passage cross-sectional geometry and non-uniformities, passage blockage, influence of cusp passages and influence of passage length, it was concluded that the hexagonal passage characteristics provide more reliable results compared to the circular passage geometry. The major disadvantage of the circular passage geometry is due to the virtually blocked flow through the cusp passages (see Figure 6.1), which clearly demonstrated the infeasibility of this geometric design.

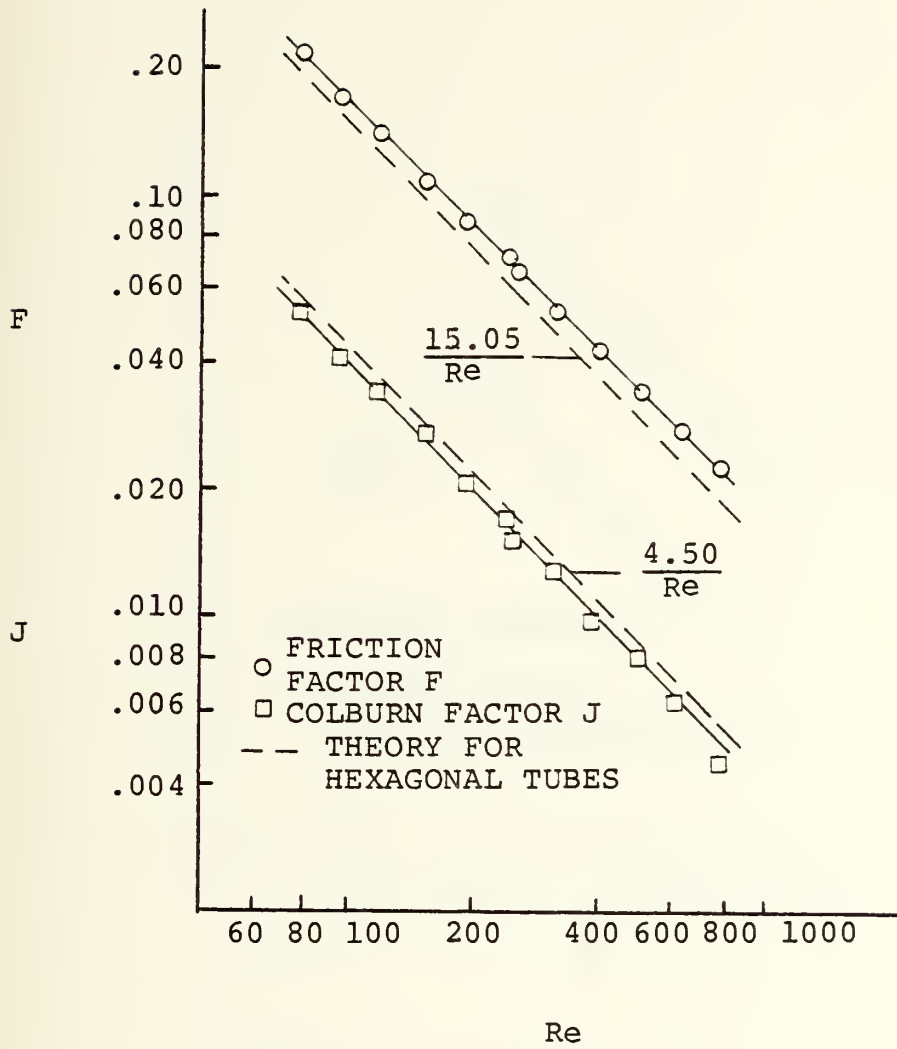


FIGURE 6.4: THERMODYNAMIC PERFORMANCE CHARACTERISTICS FOR HEXAGONAL PASSAGE

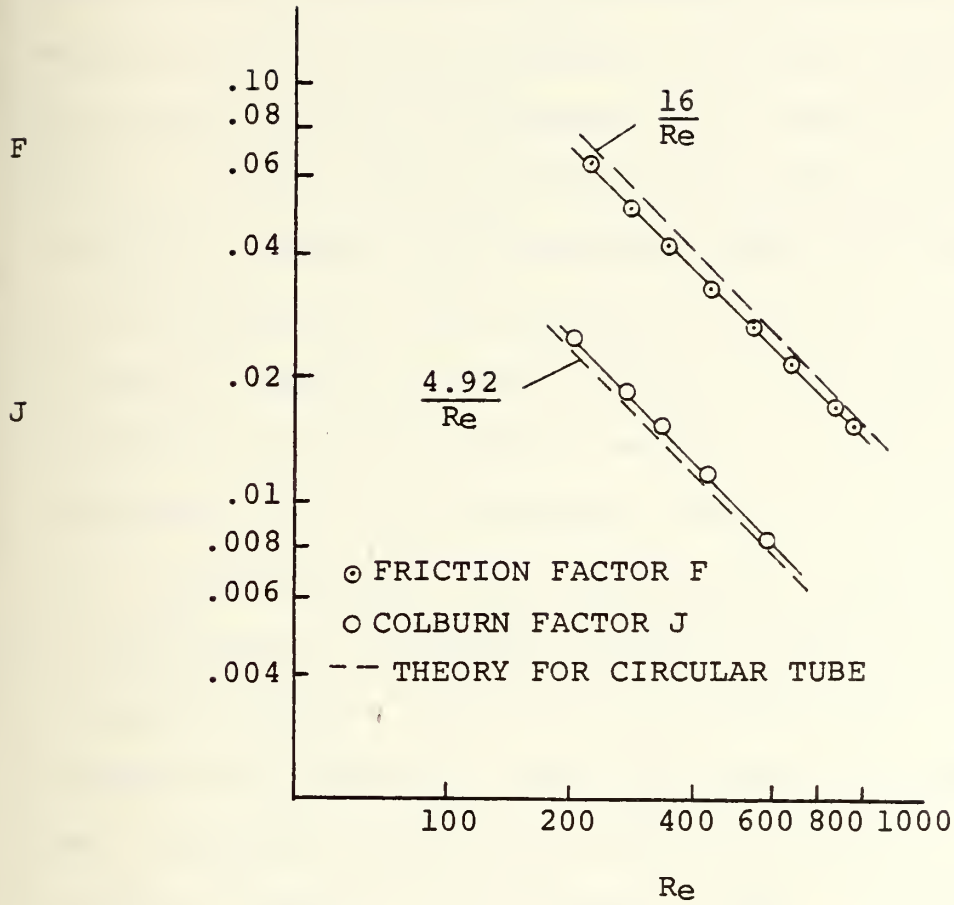


FIGURE 6.5: THERMODYNAMIC PERFORMANCE CHARACTERISTICS FOR CIRCULAR PASSAGE

Table 6.3 compares the data of references (4), (8), (51) and (52).

Though the researchers at Sanford University theoretically believed the performance characteristics of hexagonal and circular passages are better than those of equilateral triangular passages, the results of Table 6.3 clearly indicate that by changing the shape of the triangular passage to an isosceles shape, the resulting aero-thermodynamic characteristics of the isosceles triangular passage is more efficient than either the hexagonal or circular shaped passages. Another possible explanation for the discrepancy detailed in reference (51), which concluded that the hexagonal passage matrix has significant advantages relative to the currently used triangular passage matrices may be due simply to when the analysis was performed. Shah and London (51) compared their hexagonal design coded 519 and analyzed in 1973 to a triangular design (52) analyzed in 1970. In other words, the triangular designs of reference (52) being at least three years older than the hexagonal designs of reference (51), probably utilized older manufacturing processes resulting in greater matrix non-uniformity, therefore lower overall fin efficiencies, J/F . On the other hand, the Ford Motor Company researchers of references (4) and (8) analyzed regenerator passage designs of the late 1970's, detailing their analysis in 1980. These

PASSAGE GEOMETRY

PARAMETER	ISOSCELES ^{8*} TRIANGLE	ISOSCELES ⁴ TRIANGLE	HEXAGONAL ⁵¹ (519)	CIRCULAR ⁵¹ (514)	EQUILATERAL ⁵² TRIANGLE
Wall Thickness (IN)	.0035	.0053	.0026	.0059	
Frontal Area (IN ²)			10.546	10.499	10.52
Flow Area (IN ²)			8.547	4.524	7.448
Area Density α (IN ² /IN ³)	151	111	137	66	141
σ = Flow Area Frontal Area	.680	.642	.811	.431	.708
N HOLES/IN ²	1674	920	1683	794	1008
L (IN)	2.11		2.997	2.997	3.0
Effectiveness E (%)	97.0		91.0		
DH (IN)	.018	.023	.024	.026	.020
L/DH	117		125	115	150
$\Delta P/P$ (%)	2.0		3.4		
J/F	.361	.361	.235	.308	.253

*Data from numbered references.

TABLE 6.3: PASSAGE GEOMETRY COMPARISON

researchers analyzed the aero-thermodynamics characteristics of various matrix passage geometries from various manufacturers using state-of-the-art processing techniques, thereby avoiding the inconsistency of comparing older technologically produced matrices to state-of-the-art produced matrices. NASA/FORD researches concluded that the isosceles triangle geometry performed better than all other designs illustrated in Figure 6.1 on an aero-thermodynamic basis comparing either the overall fin efficiency ratio, J/F , or the alternative efficiency ratio, A/C .

6.4 Passage Geometry Selection

From the data compiled in Table 6.3 and from the aero-thermodynamic analysis presented in Figures 6.2, 6.3, 6.4, and 6.5, the isosceles triangular passage design is selected as the most effective and most suitable design for the new engine regenerator.

CHAPTER 7

COST ANALYSIS7.1 Introduction

As mentioned in the introduction, the emergence of low-cost high-temperature capable ceramic materials have the potential to greatly increase the operating temperatures of diesel and spark ignition engines and subsequently improving the fuel economy of these engines. But, are the costs of fabricating a matrix regenerator made from MAS or α -SiC less than the costs required for fabricating the regenerator from a superalloy metal? The following four sections will attempt to answer this question.

7.2 Comparison of Raw Material Costs

Most ceramic products are made from low cost raw materials, and MAS and α -SiC are no exception. Even though these two ceramic materials are higher in cost relative to other ceramic materials, as diagrammed in Figure 1.6, α -SiC and MAS raw material costs are still far less expensive than the raw material costs of superalloy metals. Though Figure 1.6 does not compare MAS to α -SiC or superalloy metals directly, reference (43) states that a MAS based regenerator is 30 to 40 percent less expensive

to fabricate than an AS (mullite of Figure 1.6) based regenerator. Therefore, based upon raw material costs alone, MAS is the least expensive material per pound, followed closely by α -SiC, and then superalloy metals, which require the most expensive raw materials. If the comparison between α -SiC, MAS and superalloy metals are based on the cost per cubic inch of product, the disparity would be even more, since the ceramic materials are less than half the density of the metals.

7.3 Comparison of Raw Material Availability

Another interesting comparison made between ceramic materials and superalloy metals which affects the costs of each, was presented by the Research and Development Division, of the Carborundum Company. At Carborundum (56), a producer of α -SiC, researchers state that their company has the capacity to produce hundreds of thousands of tons of α -SiC powder annually. On the other hand, some of the constituents, needed to produce the superalloy metals, such as cobalt, tungsten, manganese, nickel and chromium, are subject to government stock piling as they are considered critical materials because they are primarily the products of other countries. Therefore, on an availability basis, which in turn affects the raw material costs, the ceramic raw materials of α -SiC and MAS are more easily obtained for manufacture and processing, than the raw materials required for superalloy metals.

7.4 Comparison of Manufacturing Costs

Though a direct comparison of the manufacturing costs derived from producing a regenerator from ceramics and superalloy metals has not been made, this comparison has been conducted comparing the fabrication of gas turbine blades made from ceramic and superalloy material (57). In this comparison, the cost savings obtained by the ceramic blades was approximately 40 percent the metal blades, due primarily to the elimination of the requirement for extensive machining or grinding of the fired ceramic blade and reduced casting/molding costs of the ceramic blade. This same cost savings can be extended to ceramic and superalloy metal regenerators. The savings attributed to the grinding requirement is due to the ability of a ceramic product made from α -SiC or MAS, to be machined in the "green" state as described in Section 3.5. This ability greatly reduces the time required for grinding and associated wearing of the grinding equipment. The high casting/molding costs of the superalloy metal regenerator are due to remelting, casting, and scrap losses inherent in the processing of the super alloy metal regenerator (6).

Extrusion of α -SiC and MAS based regenerators have indicated that die-costs for the soft α -SiC material will be significantly lower than the highly abrasive MAS powder (21).

7.5 Comparison of Total Costs

The comparison between ceramic and superalloy metals costs on a per unit heat transfer area was not conducted and information related to this comparison was not found. However, from the comparative analysis conducted in the previous three sections, it can be concluded that a ceramic regenerator made of MAS or α -SiC will be much cheaper than a regenerator made from a superalloy metal. The cost advantage of the ceramic regenerator are due to the significantly lower costs required for the raw material, and casting and machining of the regenerator compared to the superalloy metal. Figure 7.1 depicts the cost breakdown of each material (6). Note that the largest percentage cost for the ceramic material is associated with the inspection and quality assurance requirement for satisfactory production. This conclusion was also made in Chapter 3, when describing the general fabrication and manufacturing steps required for a α -SiC and MAS regenerator (46). However, Figure 7.1 fails to compare the total cost on a per pound or per heat transfer area basis between a ceramic and superalloy metal regenerator.

When a comparison is made between the manufacturing costs for a MAS and a α -SiC regenerator, a definitive conclusion cannot be made as to which ceramic material produces the less expensive regenerator. The MAS's raw

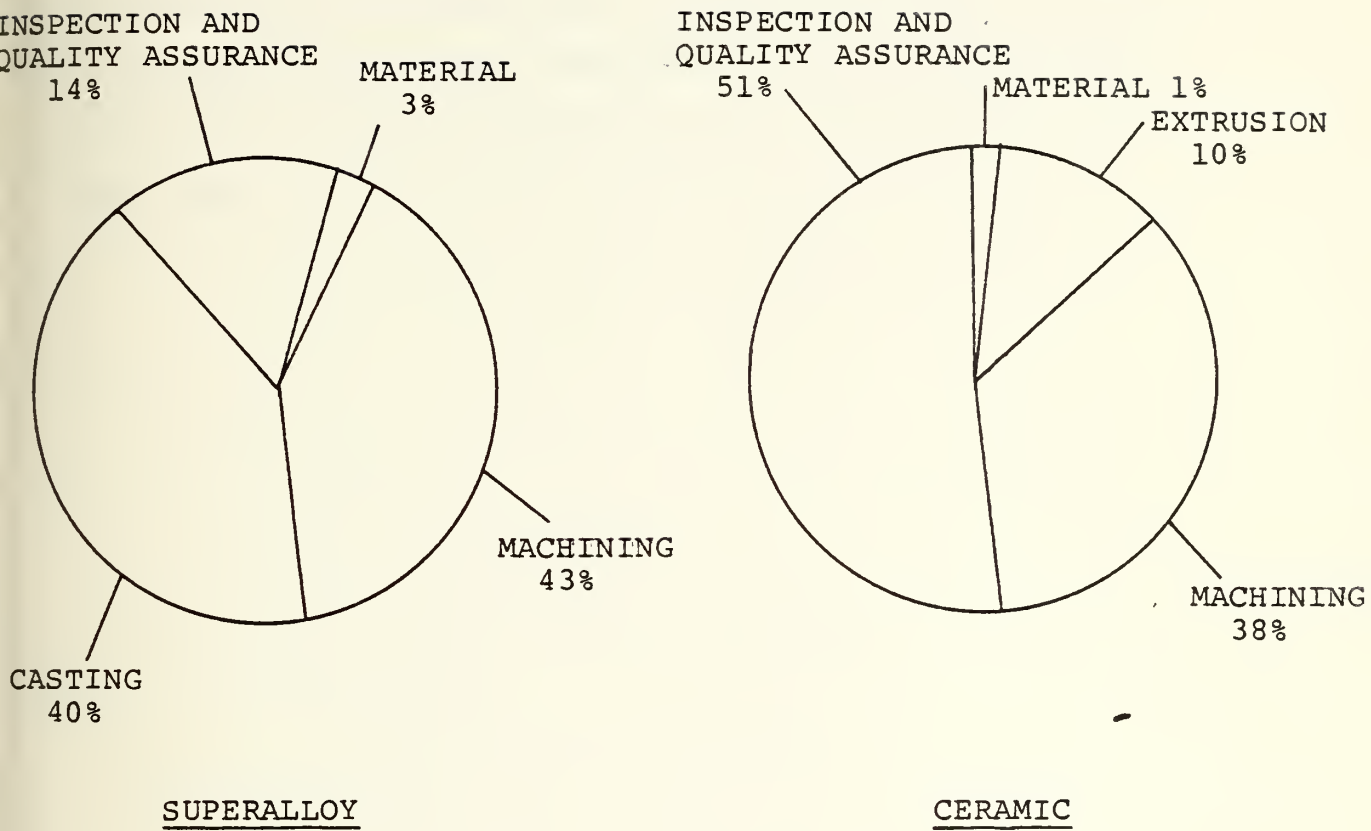


FIGURE 7.1: COST BREAKDOWN FOR SUPERALLOY AND CERAMIC BASED PRODUCTS

material costs are less than α -SiC, but the forming process costs for MAS are more than α -SiC. The most likely conclusion that can be made is that, on the basis of raw material, fabrication, firing and machining costs, it appears that a α -SiC regenerator can be readily mass produced at a cost competitive with a regenerator made from MAS.

CHAPTER 8

SUMMARY8.1 Introduction

The requirements for a ceramic regenerator for use in an engine have been established by numerous investigators. The most desirable parameters of a ceramic regenerator material are:

1. Strength at the working temperatures (both the compressed air temperature and exhaust gas temperature).
2. Good corrosion resistance at the working temperatures.
3. High thermal shock resistance.
4. Low thermal conductivity.
5. Ability to be fabricated into desired shape and design.
6. Economically competitive with existing regenerator materials.

By comparative analysis, among and between ceramics and superalloy metals, the ceramic, magnesium aluminum silicate (MAS), exhibits the best combination of the thermal and mechanical properties desired for operating temperatures up to 1200°C . On the other hand, for operating temperatures above 1200°C and up to 1400°C ,

alpha-silicon carbide (α -SiC) is selected as the ceramic material possessing the optimum balance of the thermal and mechanical properties required of the regenerator envisioned for the new engine cycle.

8.2 MAS

The mechanical and thermal properties of MAS, the ceramic material selected for operation for temperatures up to 1200°C, are included in Table 8.1.

8.3 α -SiC

The mechanical and thermal properties of α -SiC, the ceramic material selected for operation between 1200°C and 1400°C, are included in Table 8.2. The α -SiC powder selected is Carborundum's Hexolog SA silicon carbide, which is recommended by the company officials for smaller, complex shapes which exactly characterizes the ceramic regenerator proposed for the new engine design.

<u>PROPERTY</u>	<u>UNITS</u>	<u>ROOM TEMPERATURE</u>
Density	g/cc	2.51
Young's Modulus	Mpsi (GPa)	1.01 (6.9)
Shear Modulus	ksi (MPa)	7.0 (48.3)
Fracture Strength	ksi (MPa)	1.61 (11.09)
Compressive Strength	Psi (KPa)	97.4 (675)
Poisson's Ratio		0.2
Flexural Strength	Ksi (MPa)	16.0 (110.3)
Thermal Conductivity	cal/cm·sec·°C	.0026 (at 1200°C)
Thermal Expansion Coefficient	$10^{-6}/^{\circ}\text{C}$	1.55 (at 90°-1200°C)
Melting Point	°C	1470

TABLE 8.1: THERMAL AND MECHANICAL PROPERTIES OF MAS

PROPERTY	UNITS	BODY TEMPERATURE			
		1000°C	1200°C	1400°C	
Density	g/cc	3.14-3.18			
Young's Modulus	Mpsi (GPa)	54.9 (378)			
Shear Modulus	Mpsi (GPa)	24.5 (169)			
Poisson's Ratio		0.118			
Flexural Strength (4 pt)	Kpsi (MPa)	66.6 (459)	65.3 (450)	62.7 (432)	
Weibull Modulus (2 parameter)		12.3			
Hardness (KNOOP)	kg/mm ²	2800			
Wet Abrasion (Riley-Stoker)		3.4			
Fracture Toughness (Double Torsion & Senb)	Ksi in ^{1/2} (MPa m ^{1/2})	4.2 (4.6)	5.8 (6.4)		
Thermal Density (Laser Flash)	cm ² /sec	0.413	0.185	0.140	
Specific Heat (Drop Calorimeter)	cal/gm°C	0.160	0.220	0.268	
Thermal Conductivity	cal/cm sec°C	0.208	0.147	0.118	
Thermal Expansion Coefficient	10 ⁻⁶ /°C	4.02 RT-700°C 5.32 700°-2000°C			
Melting Point	°C	2700			

TABLE 8.2: THERMAL AND MECHANICAL PROPERTIES OF α-SiC

REFERENCES

1. W.T. Bakker and D. Kotchick, "Material Requirements for High Pressure Ceramic Heat Exchangers", Ceramic Proceedings, Sept.-Oct. 1982, pp. 379-809.
2. R.A. Penty and J.W. Bjerklie, "Silicon Carbide for High-Temperature Heat Exchangers", Ceramic Proceedings, Jan-Feb 1982, pp 120-125.
3. D.W. Richerson, "Modern Ceramic Engineering Properties, Processing and Use in Design", Marcel Dekker, Inc., 1982.
4. C.A. Fucinari, "Regenerator Matrix Physical Property Data", NASA CR-159854, NASA Contract DEN 3-8, May 1980.
5. R.A. Alliegro, "Processing and Fabrication of Non-Hot-Pressed Silicon Carbide", presented at Second Army Materials Technology Conference, Hyannis, MA, 1973, pp 253-263.
6. A.F. McLean, "Ceramics in Small Vehicular Gas Turbines", presented at Second Army Materials Technology Conference, Hyannis, MA, 1971, pp. 9-36.
7. I.M. Lachman, R.D. Bagley, and R.M. Lewis, "Thermal Expansion of Extruded Cordierite Ceramics", Ceramic Bulletin, Vol. 60, No. 2, 1981, pp. 202-205.
8. J.A. Cook, C.A. Fucinari, J.N. Lingscheit, and C.J. Rahnke, "Evaluation of Advanced Regenerator Systems", NASA CR-159422, NASA Contract DEN 3-8, August 1978.
9. D.W. Richerson, "Modern Ceramic Engineering Properties, Processing and Use in Design", Marcel Dekker, Inc. 1982.
10. H.E. Helms and J.A. Byrd, "Ceramic Components for Automotive and Heavy Duty Turbine Engines - CATE and AGT 100", ASME Publication, 82-GT-253.
11. S.T. Bulgain and R.N. Kleiner, "Development of a Low Thermal Expansion Magnesium-Aluminum-Silicate Ceramic for Gas Turbine Heat Exchanger Applications", ASME Publication, 75-GT-66.

12. J.P. Day, "A Study of Chemical Reactivity in Ceramic Heat Exchangers", ASME Publication 78-GT-118.
13. J.G. Lanning and D.J.S. Wardale, "The Development of a Glass-Ceramic Axial Flow Rotary Regenerator", ASME Publication, 66-GT-107.
14. J.J. Cleveland, C.W. Fritsch, and R.N. Kleiner, "Fracture Strength and Thermal Shock Resistance of Thick- and Thin-Wall Magnesium-Aluminum-Silicate Ceramic Heat Exchangers", ASME Publication, 77-GT-98.
15. C.A. Fucinari, C.J. Rahnke, V.D.N. Rao, and J.K. Vallance, "Ceramic Regenerator Systems Development Program - Final Report", October 1980.
16. W.D. Kingery, "Introduction to Ceramics", Second Edition, John Wiley and Sons, Inc., New York. 1976.
17. J.E. Hope and W.C. Riley, "Modern Ceramics: Some Principles and Concepts", John Wiley and Sons, Inc., New York, 1965.
18. R.P. Tye, "Thermal Conductivity", Volume 2, Academic Press, New York. 1969.
19. D.F. Miner and J.B. Seastone, "Handbook of Engineering Materials", First Edition, Wiley Engineering Handbook Series, John Wiley and Sons, Inc., New York. 1955.
20. J.F. Lynch, C.G. Ruderer, and W.H. Duckworth, "Engineering Properties of Selected Ceramic Materials", Battelle Memorial Institute, Columbus Laboratories, Columbus, OH. 1966.
21. C.A. Fucinari and V.D.N. Rao, "Feasibility Study of Silicon Nitride Regenerators", Ford Motor Co., October 1979.
22. J.A. Mangels and G.J. Tennenhouse, "Densification of Reaction-Bonded Silicon Nitride", Ceramic Bulletin, Vol. 59, No. 12, 1980, pp. 1216-1222.
23. T. Hirai, S. Hayashi, and K. Niihara, "Thermal Diffusivity, Specific Heat and Thermal Conductivity of Chemically Vapor-Deposited Si_3N_4 ", Ceramic Bulletin, Vol. 57, No. 12, 1978, pp. 1126-1129.

24. S. Dutta, "Microstructure and Property Characterization of Sintered Si_3N_4 , SiC , and SiALON ", Comm. of Am. Ceram. Soc., Vol. 65, No. 1, January 1982, pp. C2 to C3.
25. J.A. Mangels and G.J. Tennenhouse, "Sintering Behavior and Microstructure Development of Yttrium-Doped Reaction-Bonded Silicon Nitride", Am. Ceram. Soc. Bull., Vol. 60, No. 12, 1981, pp 1306-1310.
26. R.E. Loehman and D.J. Rowcliffe, "Sintering of $\text{Si}_3\text{N}_4\text{-Y}_2\text{O}_3\text{-Al}_2\text{O}_3$ ", J. Am. Ceram. Soc., Vol. 63, Nos. 3-4, April 1980, pp. 144-148.
27. D.R. Clarke and F.F. Lange, "Strengthening of a Sintered Silicon Nitride by a Post-Fabrication Heating Treatment", Comm. Am. Ceram. Soc., Vol. 65, No. 4, April 1982, pp. C-51 to C-52.
28. D.W. McKee and D. Chatterji, "Corrosion of Silicon Carbide in Gases and Alkaline Melts", J. Am. Ceram. Soc., Vol. 59, No. 9-10, September-October 1976, pp. 441-444.
29. A. Giachello, P.C. Marginengo, G. Ommasini and P. Popper, "Sintering and Properties of Silicon Nitride Containing Y_2O_3 and MgO ", Ceram. Bull., Vol. 59, No. 12, 1980, pp. 1212-1215.
30. D.E. Schwab and D.W. Kotchick, "High Temperature Strength of Sintered $\alpha\text{-SiC}$ in Salt and Oxidizing Environments", Ceram Bull., Vol. 59, No. 8, 1980, pp. 805-813.
31. L.L. Hench, P.N. Viadyanathan, and S. Dutta, "Effect of Y_2O_3 and Al_2O_3 on the Oxidation Resistance of Si_3N_4 ", Ceram. Proc., September-October 1982, pp. 587-595.
32. F.W. Galasso and R.D. Veltri, "Sintering of $\text{Si}_3\text{N}_4\text{-Y}_2\text{O}_3$ Under Nitrogen Pressure", Comm. Am. Ceram. Soc., Vol. 64, No. 1, January 1981, pp. C-15 to C-16.
33. J.A. Costello and R.E. Tressler, "Oxidation Kinetics of Hot-Pressed and Sintered $\alpha\text{-SiC}$ ", J. Am. Ceram. Soc., Vol. 64, No. 6, June 1981, pp. 327-331.
34. C.L. Quackenbush, J.T. Neil, and J.T. Smith, "Sintering Microstructure and Properties of Si_3N_4 and SiC Based Structural Ceramics", ASME Publication, 81-GT-220.

35. R.N. Katz and E.M. Lonoe, "Ceramics for Small Airborne Engine Applications", Advisory Group for Aerospace Research and Development, March 1980.
36. W. Bocker and H. Hausner, "The Influence of Boron and Carbon Additions on the Microstructure of Sintered Alpha Silicon Carbide", Powder Metallurgy Internl, Vol. 10, No. 2, 1978, pp. 87-89.
37. S.C. Singhal, "Corrosion-Resistance Structural Ceramic Materials For Gas Turbines", Proceedings of 1974 Gas Turbine Materials in the Marine Environment, Marine Maritime Academy, Castine, Maine, 24-26 July 1974.
38. M.B. Trigg and E.R. McCartney, "The Reactions of Silicon Nitride with Vanadium Oxides", Ceramurgia Internl., Vol. 6, No. 1, 1950, pp. 147-148.
39. S.C. Singhal, "Oxidation and Corrosion-Erosion Behavior of Si_3N_4 and SiC ", Army Materials Technology Conf. 2nd, Hyannis, MA. 1973.
40. J.A. Copolla, M. Srinivasan, K.T. Faber, and R.H. Smoak, "High Temperature Strength of Sintered Alpha Silicon Carbide", Internl. Sym. on Factors in Densification and Sintering of Oxide and Non-Oxide Ceramics, October 1978, Hakone, Japan.
41. R.C.A. Harris, "Oxidation of 6H- α Silicon Carbide Platelets", J. Am. Ceram. Soc., Vol. 58, No. 1-2, Jan-Feb 1975, pp. 7-9.
42. I.A. Yrorskii, V.J. Elchin, and G.G. Genesin, "Test Methods and Properties of Materials", Soviet Powder Metallurgy and Metal Ceram., Vol. 17, No. 27, December 1978. pp. 542-545.
43. Y. Murata and R.H. Smoak, "Densification of Silicon Carbide by the Addition of BN, BP and B_4C , and Correlation to Their solid Solubilities", Internl. Sym. on Factors in Densification and Sintering of Oxide and Non-Oxide Ceramics, October, 1978, Hakone, Japan.
44. J.S. Haggerty, "Growth of Precisely Controlled Powders From Laser Heated Gases", Proc. Internal Conf. Ultrastructure Processing of Ceramics, Glasses, and Composites, Feb. 13-17, 1983, Gainesville, FL.

45. R.A. Massa and J.S. Haggery, "Synthesis and Characterisitcs of Ceramic Powders* made from Laser-Heat Gases", Ceram. Eng.Sci. Proc., Vol. 3, No. 1-2, 1982, pp. 3-19.
46. E.A. Fisher, "Technical Ceramic Fabrication Processs", ASME Publication, 75-GT-110.
47. F.H. Norton, "Warping and its Control", Ceramic Fabrication Processes. Edited by W. D. Kingery, 1963.
48. S. Prochazka, "Sintering of Silicon Carbine", Army Materials Technology Conf. 2nd, Hyannis, MA. 1973.
49. S. Prochazka, "Sintering of Silicon Carbide", Mass. Transport Phenomena in Ceramics. Edited by A.R. Cooper and A.H. Heuer, 1974.
50. J.A. Costello, R.E. Tressler, and I.S.T. Tsong, "Boron Redistribution in Sintered α -SiC During Thermal Oxidation", Fall Meeting Am. Ceram. Soc., New Orleans, LA. October 15, 1979.
51. A.L. London and R.K. Sha, "Class-Ceramic Hexagonal and Circular Passage Surfaces - Heat Transfer and Flow Friction Design Characteristics", Transactions SAE, 1973, pp. 425-434.
52. A.L. London, M.B.O. Young, and J.H. Tang, "Glass-Ceramic Surfaces, Straight Triangular Passages - Heat Transfer and Flow Friction Characteristics", Trans. ASME, Vol. 92, Series A, Oct. 1970, pp. 381-389.
53. R.L. Cable, "Effect of Microstrucure on the Mechanical Properties of Ceramic Material", Ceramic Fabrication Processes. Edited by W. D. Kingery, 1963.
54. S. Srinivasagopalan, M. Srinivasan, and G.W. Weber, "Proof Test Studies in Sintered Alpha Silicon Carbide", Presented at 4th Annual Conf. Composites and Adv. Mat., Am. Ceram. Soc., Jan 21-23, 1980.
55. M. Srinivasan and S.G. Seshardi, "Probabilistic Design and Reliability of Silicon Carbide Ceramics", ASME 1981 Failure Prevention and Reliability Conf., Hartford, CT, Sept. 10-23, 1981.

56. E. J. Stefanides, "Alpha SiC Ceramic Solves Heat, Wear Problems", Design News, May 1980, p. 115.
57. A. Brooks and A.I. Bellin, "Benefits of Ceramics to Gas Turbines", "Advisory Group For Aerospace Research and Development, March 1980.
58. B.K. Miller, Jr., "Ceramics in Diesels", Report For Course 13.15J at MIT, May 13, 1983.

THE DEVELOPMENT OF QUALITY STANDARDS
AND IMPACT MODEL FOR USE IN HIGHWAY
MAINTENANCE

Richard Thomas Geikie

Thesis

K3985 Kikuta

Selecting the proper
ceramic material for a
regenerator experien-
cing large temperature
gradients.

207073

Thesis

K3985 Kikuta

Selecting the proper
ceramic material for a
regenerator experien-
cing large temperature
gradients.

207073

thesK3985

Selecting the proper ceramic material fo



3 2768 002 11920 8

DUDLEY KNOX LIBRARY